Review

Experimental aspects of geoneutrino detection: Status and perspectives

O. Smirnov

JINR, Joint Institute for Nuclear Research, Dubna, Russian Federation

A R T I C L E   I N F O

A B S T R A C T

Neutrino geophysics, the study of the Earth's interior by measuring the fluxes of geologically produced neutrino at its surface, is a new interdisciplinary field of science, rapidly developing as a synergy between geology, geophysics and particle physics. Geoneutrinos, antineutrinos from long-lived natural isotopes responsible for the radiogenic heat flux, provide valuable information for the chemical composition models of the Earth. The calculations of the expected geoneutrino signal are discussed, together with experimental aspects of geoneutrino detection, including the description of possible backgrounds and methods for their suppression. At present, only two detectors, Borexino and KamLAND, have reached sensitivity to the geoneutrino. The experiments accumulated a set of $\sim$190 geoneutrino events and continue the data acquisition. The detailed description of the experiments, their results on geoneutrino detection, and impact on geophysics are presented. The start of operation of other detectors sensitive to geoneutrinos is planned for the near future: the SNO+ detector is being filled with liquid scintillator, and the biggest ever 20 kt JUNO detector is under construction. A review of the physics potential of these experiments with respect to the geoneutrino studies, along with other proposals, is presented. New ideas and methods for geoneutrino detection are reviewed.

© 2019 Elsevier B.V. All rights reserved.

Contents

E-mail address: osmirnov@jinr.ru.

1. Introduction

The Earth's surface heat flow is, in part, fed by the energy released in the radioactive decay of long-lived isotopes naturally present in its crust and mantle. Geoneutrinos, antineutrinos emitted in these decays, would provide useful geological information if detected. But the neutrino detection is not a simple task as they almost do not interact with matter. Interest in the geoneutrinos significantly rose due to the development of large volume detectors, able to detect their exiguous interaction rates. These measurements are expected to shed light on abundances and distributions of radioactive elements inside the Earth beyond the reach of direct measurements by sampling. The natural radioactivity of the Earth is a powerful source of heat influencing the thermal history of the planet. The knowledge of the radioactive content in the Earth's depths is essential for many problems in geoscience.

The importance of radioactivity in the Earth's heat balance was understood quite early after its discovery. In 1905, Irish physicist J. Joly was the first who commanded attention to rock radioactivity as a source of the Earth's thermal energy. His early calculations showed that the distribution of radioactive elements is not uniform throughout the Earth's volume, as the concentration of radioactive elements in the crust extrapolated to the entire volume would result in significantly higher heat production than the known total heat flux from the Earth. In other words, these calculations indicated that the concentration of radioactive elements in the mantle and the core are lower than in the crust [1]. In the 1970s, uranium and thorium concentrations were measured in mantle rock samples extracted from the ocean floor, and they indeed turned out to be low. Hence, natural radioactive isotopes are concentrated mainly in the continental crust. The energy from the decay of radioactive isotopes is an important source of heat in the Earth, which is estimated to account for roughly half of the Earth's total heat release. The Earth emitted more radiogenic heat at the initial stage of its existence than it emits now, primarily because rocks at that time had more radioactive elements. Decays of the ^{26}Al isotope with a half-life of 0.717 Myr were the primary heat source in the early Earth.

There are different types of radioactive decays among the radioactive isotopes heating the Earth. The energy of α-decays is totally converted into heat, while the energy released in β-decays is partially taken away by antineutrinos. Historically, the study of β-decay provided the first physical evidence for the neutrino existence. The continuous spectrum of the β-decay was a mystery, as there was no apparent third particle to provide the energy and angular momentum balance. In a famous letter written in 1930, Pauli suggested the existence of a light neutral particle, which he called the neutron. This "neutron" emitted during β-decay would account for the missing energy and angular momentum. In 1931 Enrico Fermi renamed the particle the neutrino, which literally means "little neutral one". The neutrino's interaction with matter is extremely weak, and its detection was an experimental challenge for a quarter of a century, accomplished only in

1956 through an experiment by Reines and Cowan [2]. Because each β-decay is accompanied by antineutrino emission, detecting these antineutrinos would mean registering the corresponding β-decays in the Earth's depths.

The first mention of geologically produced neutrinos in modern physics can be found in the Gamow letter to Reines (see e.g. [3]). Gamow suggested that unidentified background observed in the nuclear reactor experiment by Reines and Cowan (devoted to the reactor antineutrino search) could be due to antineutrinos from β-decaying members of the U and Th families. In his teletype answer Reines reported the first estimate of the 1 MeV antineutrino flux of 10^8 cm^{-2} s^{-1} at the Earth's surface based on the heat loss at the surface of 50 erg cm^{-2} s^{-1}, which was not enough to explain the excess despite the fact that the antineutrino flux was significantly overestimated in this calculation.

In 1960 Marx and Menyhárd [4] were the first to obtain a realistic estimate of the geoneutrino flux at the Earth surface of 6.7×10^6 s^{-1} cm^{-2}. Geoneutrinos were discussed by Markov in his monograph on neutrinos [5], later Eder [6] was the first who pointed out the importance of geoneutrino[1] studies in the context of the problem of heat release in the Earth, and Marx's discussion of the geophysics by neutrinos in [7] closed the decade.

The modern theoretical study of this problem is attributed to the work of Krauss, Glashow, and Schramm [8]. The first paper in a geophysical journal appeared only in the 1990s [9]. The potential of the Borexino and KamLAND detectors for geoneutrino detection was first pointed out by Raghavan et al. [10][2] and Rothschild et al. [12], respectively. The interest in geoneutrinos in the geoscience community exploded after the first experimental indication of their presence by the KamLAND [13] and Borexino collaborations [14]. At present one can state that we are witnessing the formation of a new field of geophysics: neutrino geoscience, merging the fine art of neutrino detection with geophysics.

Geoneutrino flux measurements will give answers to the still debatable questions about the natural radioactivity of our planet: what is the radiogenic contribution to the total heat generated by the Earth? how much uranium, thorium and potassium are distributed in the Earth's crust and mantle? what are the planetary Th/U and K/U mass ratios? how uranium and thorium are distributed in the Earth's crust and mantle? is the mantle chemically uniform, layered, or more complicated? are there mantle reservoirs enriched in U and Th? is there any georeactor or hidden excessive ^{40}K in the Earth's core, as suggested by some theoreticians? are the geochemical Bulk Silicate Earth (BSE) models consistent with geoneutrino data? and which of the proposed Earth models will fit the observed geoneutrino flux?

An important note: in this review we are concentrated on the geologically produced neutrinos. The use of other natural or artificial neutrino sources for the purpose of geological research have been actively studied in parallel with the development of particle acceleration techniques and neutrino detectors. There were proposals to use neutrino beams to search for deposits of oil and gas or high-Z ores at large distances from the accelerator. Other projects were aiming the exploration of the vertical density profile of the Earth and especially its core. All of these interesting projects are beyond the scope of this review.

2. Geoneutrinos and the Earth's heat

The natural radioactivity of the present Earth is associated with long-lived radioactive isotopes (radionuclides) with half-lives of the order of billions of years, comparable with the Earth's and Solar system's age. The complete list of these isotopes (including both α and β radioactive nuclides) contains 28 nuclides, and another six nuclides have half-lives longer than 80 million years, long enough for some of them to survive in noticeable quantities up to the present day. These 34 naturally occurring radioactive nuclides comprise the primordial nuclides with different abundances and life-times, but the major contribution to the Earth's radioactivity comes from very few of them, namely from decays of radioactive elements in chains of decays started with ^{238}U and ^{232}Th, and from decays of ^{40}K, with some contribution from the ^{235}U chain and from decays of ^{87}Rb and ^{147}Sm.

Electron antineutrinos ($\overline{\nu_e}$) are produced in radioactive β-decays

$$^A_Z X \rightarrow ^A_{Z+1} Y + e^- + \overline{\nu_e}, \tag{1}$$

where A and Z are the mass and atomic number of the parent nucleus X. The daughter nucleus Y has the same A and Z increased by 1. The energy released in the reaction corresponds to mass difference Q_0 between the parent and the daughter nuclei. The energy release Q_0 is distributed between the electron and the antineutrino. Because of the tiny cross section of interaction with matter the antineutrino carries away a fraction of the total energy release. The energy of electrons emitted in β-decays, as well as the energy of the accompanying γ-radiation and energy produced in α-decays, is converted into the heat, called radiogenic. Another source of heat is primordial heat accumulated during the formation of the Earth. In accordance with modern understanding, radioactive decays are responsible for roughly a half of the total heat flow of the Earth, with the other half coming from the secular cooling of the Earth. The energy budget of the Earth is schematically shown in Fig. 3.

---

[1] Eder used the term "terrestrial neutrinos".

[2] A revolutionary 50 kt Borex detector was also proposed by Raghavan [11]; the idea was materialized as a smaller version, a 0.3 kt detector called Borexino.

2.1. Long-lived radiogenic elements

We start with reviewing the radiogenic elements. The most important decays, from the geophysical point of view, are those in the U and Th decay chains, and the ^{40}K decay.

The uranium chain (historically called the "radium series") begins with naturally occurring ^{238}U. It includes isotopes of astatine, bismuth, lead, polonium, protactinium, radium, radon, thallium, and thorium, providing that all are present in any uranium-containing sample. The total energy released per decay of ^{238}U into the stable ^{206}Pb is 51.773±0.017 MeV on the assumption of secular equilibrium.[3] Natural uranium, along with ^{238}U and ^{235}U, contains the decay product ^{234}U, which is in secular equilibrium with its parent ^{238}U, and its long lifetime provides $5.5 \cdot 10^{-5}$ isotopic abundance in natural uranium. Uranium-234 and its daughter decays are included in the calculations as a part of the parent ^{238}U chain. In the course of transformation of ^{238}U into ^{206}Pb 8 α- and 6 β-decays occur, the latter are accompanied by 6 antineutrinos

$$_{92}^{238}\text{U} \rightarrow_{82}^{206}\text{Pb} + 8\alpha + 6e^- + 6\overline{\nu_e} + 51.77 \text{ MeV.} \tag{2}$$

Another chain starts with the less abundant uranium isotope, ^{235}U ("actinium series"). This decay series includes isotopes of actinium, astatine, bismuth, francium, lead, polonium, protactinium, radium, radon, thallium, and thorium. The total energy released per decay of the parent ^{235}U into the stable ^{207}Pb is 46.398±0.010 MeV on the assumption of secular equilibrium. The transformation of ^{235}U into ^{207}Pb occurs through 7 α- and 4 β-decays accompanied by 4 antineutrinos

$$_{92}^{235}\text{U} \rightarrow_{82}^{207}\text{Pb} + 7\alpha + 4e + 4\overline{\nu_e} + 46.40 \text{ MeV.} \tag{3}$$

The last chain is the "thorium series" beginning with naturally occurring ^{232}Th. This series includes isotopes of actinium, bismuth, lead, polonium, radium, and radon. The total energy released per decay of the parent ^{232}Th into the stable ^{208}Pb is 42.6575 ± 0.0053 MeV. The transformation of ^{232}Th into ^{208}Pb occurs through 6 α- and 4 β-decays accompanied by 4 antineutrinos

$$_{90}^{232}\text{Th} \rightarrow_{82}^{208}\text{Pb} + 6\alpha + 4e^- + 4\overline{\nu_e} + 42.66 \text{ MeV.} \tag{4}$$

The main route of the ^{238}U and ^{232}Th decay chains are presented schematically in Figs. 1 and 2. The less important branches are excluded in these charts for the sake of simplicity.

Potassium-40 (^{40}K) is a radioactive isotope of natural potassium with a half-life long enough to survive in noticeable amount until the present day, the modern isotopic abundance of ^{40}K is $\sim$117 ppm. ^{40}K decays through two channels, β-decay

$$_{19}^{40}\text{K} \rightarrow_{20}^{40}\text{Ca} + e^- + \overline{\nu_e} + 1.311 \text{ MeV}, \quad (89.3\%), \tag{5}$$

and electron capture

$$_{19}^{40}\text{K} + e^- \rightarrow_{18}^{40}\text{Ar} + \nu_e + 1.505 \text{ MeV}, \quad (10.72\%). \tag{6}$$

A fraction of the EC decays occurs into the excited state of ^{40}Ar (1460 MeV). In accordance with available data [15] the intensity of the 1460.82 MeV γ-line is $(10.66 \pm 0.17)\%$, and the total EC branch has $(10.72 \pm 0.13)\%$ branching ratio, leaving for EC into the ground state $(0.06 \pm 0.04)\%$. This decay is anticorrelated with 10.66% decay into the excited state. The EC into the ground state slightly reduces the heating energy. The ^{40}K β^- decay is unique third forbidden, our estimate of the effective energy release (average energy of the β- spectrum) $E_{eff} = 583.6$ keV for ^{40}K is in a good agreement with both the experimentally obtained value $\langle E \rangle = 583.98$ keV [16] and the recent calculations $\langle E \rangle = 583.27$ keV [17].

The last two decays of minor importance are those of ^{87}Rb and ^{147}Sm. Rubidium is the 23rd most abundant element in the Earth. So, despite its relatively low specific heat yield, it could be important for precision calculations

$$_{37}^{87}\text{Rb} \rightarrow_{38}^{87}\text{Sr} + e^- + \overline{\nu_e} + 0.2833 \text{ MeV.} \tag{7}$$

According to McDonough and Sun [18], natural Rb is $\sim$400 times less abundant than K with specific heat yield 2.4 times greater than that of natural K, thus adding to the total heat about 0.6% of the potassium contribution.

Samarium is just the 40th among the most abundant elements. The isotopic abundance of natural Sm is lower than that of ^{87}Rb, $\sim$600 times less abundant compared to K [18], but its α-decay is more energetic, $E_0 = 2.3$ MeV, providing specific heat yield 14 times greater than that of natural K. As a result, ^{147}Sm contributes to the total radiogenic heat even more than ^{87}Rb, adding $\sim$2.3% of the potassium contribution. The total heat from Rb and Sm is about 0.1 TW, well below the uncertainty of the total heat flow measurement.

Heat production of other elements from the list of long-lived isotopes is calculated in [19], and all the contributions are at least an order of magnitude lower than the aforementioned ones.

The properties of the main contributors to the radiogenic heat production are presented in Table 1. Q_{tot} is the total energy released in the corresponding decay or chain of decays including the energy taken away by antineutrinos. Heating

---

[3] The life-time of the ^{238}U and ^{232}Th is much longer than life-time of any daughter isotope in the corresponding chain, therefore on the long time-scale the decay rates of daughter radioactive isotopes coincide with the decay rate of the parent isotope. In nuclear physics this situation is called secular equilibrium.

Table 1
Characteristics of the main contributors to the radiogenic heat production. Following the ENSDF database notations, the numeric uncertainty, shown in parentheses, denotes an uncertainty in the last significant figure(s).

|	^{238}U	^{235}U	^{232}Th	^{40}K	^{87}Rb	^{147}Sm
Decay(s) type	$\beta + \alpha$	$\beta + \alpha$	$\beta + \alpha$	β & EC (ν)	β	α
Natural isotopic abundance	0.992742	0.007204	1.0000	$1.1668(8) \cdot 10^{-4}$	0.2783(2)	0.1499(18)
Life-time, $T_{1/2}$ (Gy)	4.468(6)	0.7038(5)	14.0(1)	1.248(3)	49.7(3)	106.0(11)
Isotope atomic mass (g/mol)	238.051	235.044	232.038	39.9640	86.909	146.915
Total decay energy, Q_{tot} (MeV)	51.773(17)	46.398(10)	42.6575(53)	1.3116(11)	0.283	2.311(1)
Heating energy, Q_H (MeV)	47.678(10)	44.383(5)	40.438(5)	0.6767(17)	0.0567(2)	2.311(1)
Specific heat yield (μW kg^{-1})	94.32(13)	4.097(3)	26.4(2)	$3.356(8) \cdot 10^{-3}$	$7.74(14) \cdot 10^{-3}$	$4.72(6) \cdot 10^{-2}$
Specific $\bar{\nu}_e$ luminosity (kg^{-1} s^{-1})	$7.41(1) \cdot 10^7$	$2.305(2) \cdot 10^6$	$1.63(1) \cdot 10^7$	$2.763(7) \cdot 10^4$	$8.5(2) \cdot 10^5$	–
Specific ν_e luminosity (kg^{-1} s^{-1})	–	–	–	$0.332(1) \cdot 10^4$	–	–
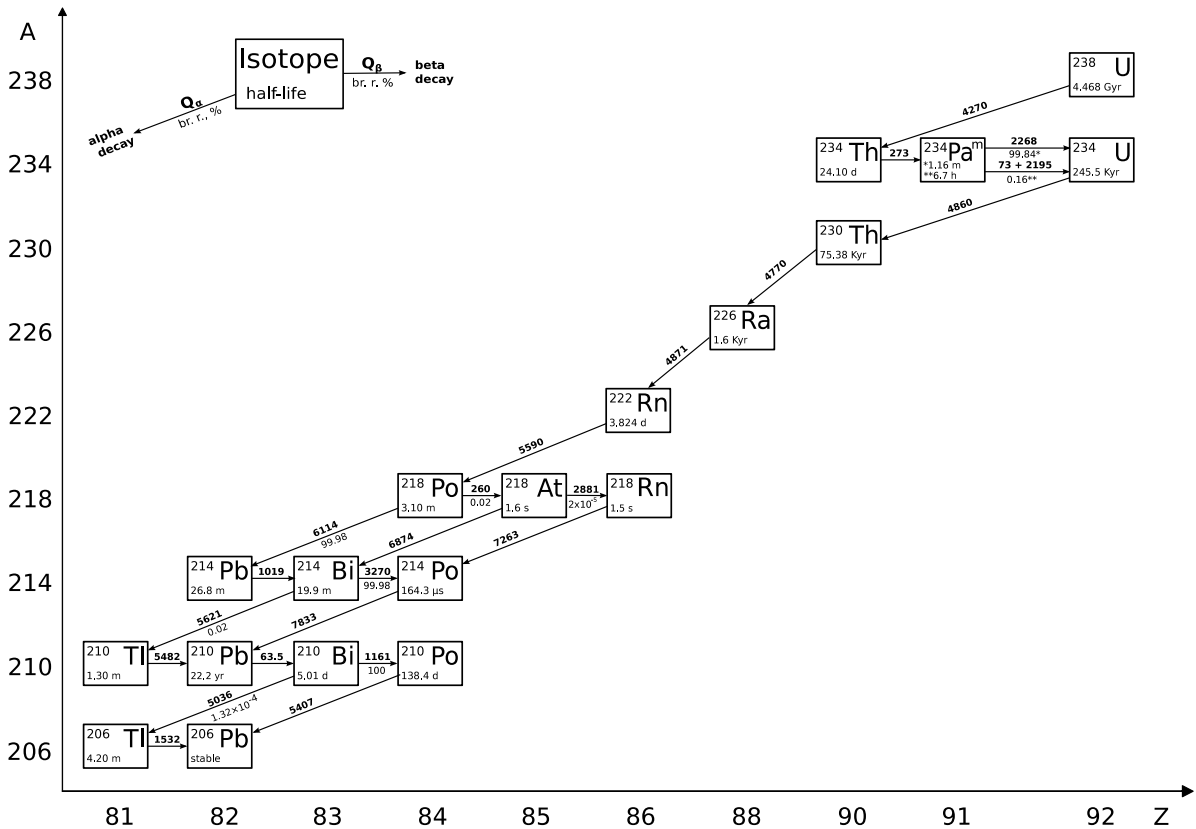
Fig. 1. ^{238}U decay chain. The scheme reproduces the original one from Fiorentini et al. [3] using the updated nuclear data.

energy Q_H is the "visible" (dissipated for heating) energy release, namely the total released energy, excluding the energy fraction taken away by antineutrinos. Specific heat yield ϵ_H and specific antineutrino (or neutrino in the case of electron capture on ^{40}K) luminosities ϵ_ν per 1 kg of naturally occurring element are provided in the last two rows with account taken of the natural abundance of the corresponding radioactive isotope fraction. In the case of uranium, the corresponding values for two isotopes should be summed to obtain the total heat and antineutrino flux per 1 kg of natural U.

The data for the evaluation of the energy release and its uncertainty were taken from the last available version of the ENSDF database [15].[4] It should be noted that while measured values of Q_{tot} have typical errors below 0.1%, the precision of evaluation of Q_H is generally less certain as it depends on the shapes of β-decay spectra and precision of the measurement of the branching ratios for complex decays with β-decay into excited levels of daughter nuclei.

---

[4] Evaluated Nuclear Structure Data File (ENSDF). The ENSDF database contains evaluated nuclear structure and decay information for over 3000 nuclides, continuously updated with new evaluations published in the Nuclear Data Sheets. We used the database version of December 2018 in the calculations. The ENSDF is compiled by the International Network of Nuclear Structure and Data Decay Evaluators (http://www-nds.iaea.org/nsdd/).
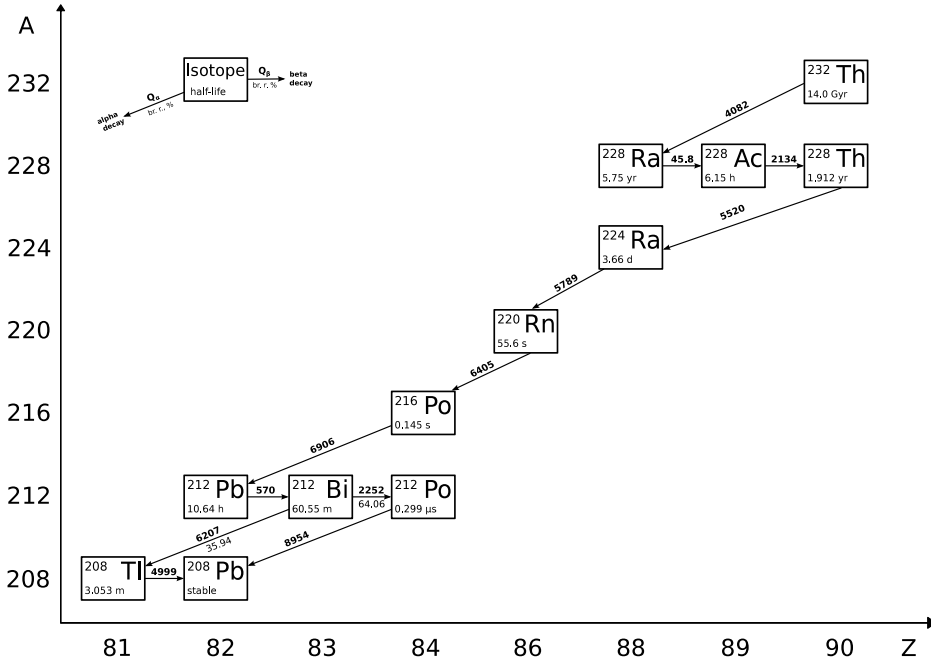
Fig. 2. ^{232}Th decay chain. The scheme reproduces the original one from Fiorentini et al. [3] using the updated nuclear data.

The details of the β-spectra shape calculations are presented below in Section 4.4. The universal β-decay shape is used in calculations with the exception of ^{210}Bi in the ^{238}U chain, of ^{40}K β-decay (3rd unique forbidden), and of ^{87}Rb (3rd forbidden non-unique). Note that the transition ^{212}Bi$\rightarrow$^{212}Po in Table 5, and all the transitions in Table 6, are forbidden non-unique ones. As an illustration of possible bias due to the spectral shape, two values could be compared: the value $Q_H = 0.122$ MeV obtained with assumption of the allowed shape and used in earlier review [3] for ^{87}Rb evaluation is twice as large as the value in Table 1 calculated using the corrected shape. The total error on energy release is not significantly influenced by the corrections to the energy shapes, since only a small fraction of the total energy is released in β-decays, typically below 5% of the total: 2.0 out of 47.7 MeV in the ^{238}U chain, 1.5 out of 44.4 MeV in the ^{235}U chain, and 1.5 out of 40.4 MeV in the ^{232}Th chain. Moreover, as will be discussed below, experimental spectra for forbidden decays of high-Z nuclei are very similar to the allowed shapes, and only minor contributions to the uncertainty of the total energy release in the U and Th chains are expected.

We can conclude that geoneutrinos are predominantly born as electron antineutrinos in β-decays with an admixture of electron neutrinos from electron captures. Neutrinos are produced only in the electron capture of ^{40}K. In contrast to the Sun powered by nuclear fusion and emitting neutrinos at the rate of $L_\nu^\odot \simeq 1.8 \times 10^{38}$ ν/s, the Earth "shines" essentially in antineutrinos produced in radioactive β^--decays, emitting $L_{\bar\nu}^\oplus \simeq 3 \times 10^{25}$ $\bar\nu$/s, many orders of magnitude below the rate of neutrino production in the Sun. For comparison, a typical nuclear reactor produces $L_\nu^R \sim \times 10^{20}$ $\bar\nu$/s. Because of the Sun-to-Earth distance the flux of the solar neutrinos at the Earth is strongly reduced and the difference in solar and geoneutrino fluxes is less pronounced, though still significant, $\Phi_\nu^\odot \sim 6 \times 10^{10}$ cm^{-2} s^{-1} neutrinos from the Sun versus $\Phi_{\bar\nu}^\oplus \sim 3 \times 10^7$ cm^{-2} s^{-1} of all antineutrinos from the Earth.

The estimates above consider total flux of neutrinos of all flavours. In the process of propagation the original electronic neutrino flavour for both the solar neutrino and earth antineutrino is not conserved because of the neutrino oscillation mechanism, and other neutrino flavours can be detected or missed depending on the detection method used.

2.2. Radiogenic heat and geoneutrino luminosity of the Earth

For a given amount of radioactive isotopes, the energy released in radioactive decays is strictly connected to the amount of antineutrinos produced in these decays. The total antineutrino production rate (or luminosity) L$_\nu$ can be related to the mass of elements contained in the Earth using the data from Table 1

$$L_\nu = [(7.64 \pm 0.1) \cdot M(\text{U}) + (1.63 \pm 0.1) \cdot M(\text{Th}) + (2.765 \pm 0.007) \cdot 10^{-3} \cdot M(\text{K}) + \cdots] \cdot 10^{24} \quad \text{s}^{-1}. \tag{8}$$

A similar relation between radiogenic heat production H$_R$ and the mass of the corresponding elements can be expressed as

$$H_R = [(9.849 \pm 0.013) \cdot M(\text{U}) + (2.64 \pm 0.02) \cdot M(\text{Th}) + (3.356 \pm 0.008) \cdot 10^{-4} \cdot M(\text{K}) + \cdots] \quad \text{TW}, \tag{9}$$
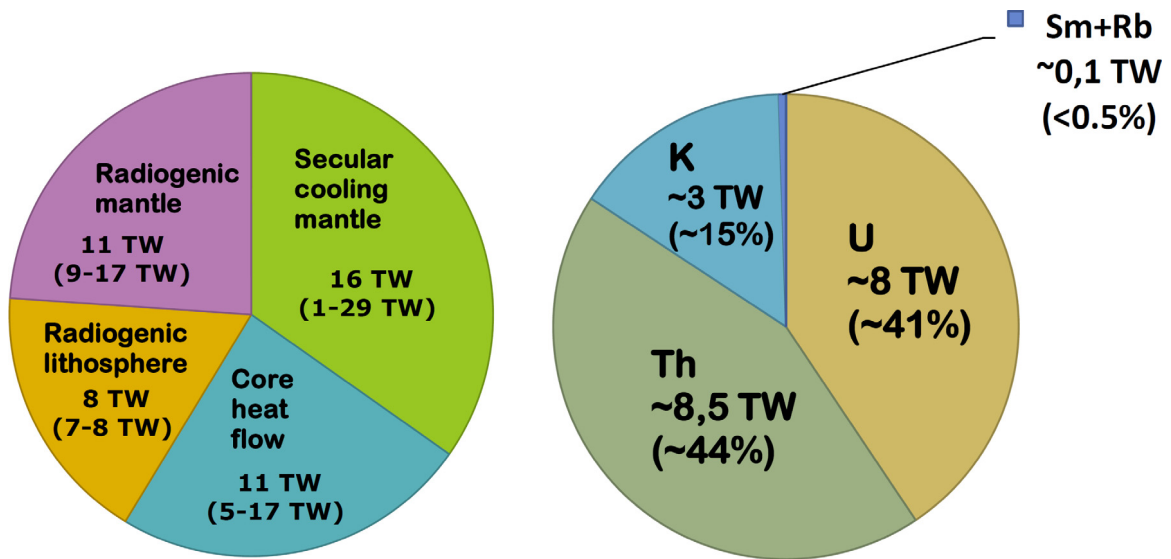
Fig. 3. Left: The energy budget of the Earth according to [20], the radiogenic heat production splits between the crust (lithosphere) and the mantle, the rest of the heat is provided by secular cooling of the mantle and core heat flow. **Right:** Heat producing elements providing major contributions to the radiogenic heat production. The heat is calculated assuming abundances of the corresponding elements from McDonough and Sun's model [18]. Other models can result in different absolute values of heat production, though the relative contributions are less sensitive to the model (see, e.g., Table 3).

where masses of the corresponding elements present in the Earth are expressed in units of 10^{17} kg, and 1 TW is 10^{12} W.[5] The estimates for the global mass of U varies from 0.5 to 1.2×10^{17} kg (see Table 3 and related discussion of the corresponding models in Section 3.3), the Th and K mass are related to the U mass, and the ratio M(Th)/M(U) and M(K)/M(U) can differ in various models. The chondritic value of M(Th)/M(U) = 3.9 and the ratio M(K)/M(U)$\sim 10^4$ are commonly used, following McDonough and Sun's estimates [18].

The Earth's interior is hotter than its surface, this difference of temperatures feeds the heat flux through the Earth's surface. The present day total energy loss of the Earth is well established by the heat flow measurements in the continents and well-tested physical models for cooling of the sea floor. The most recent estimates are those by Jaupart et al. providing the 46 ± 3 TW heat flow [20]. The authors revised the analysis of $\sim$25000 heat flow measurements around the globe used in previous estimates, reassessing the required corrections and errors. Another estimate, based on the data from $> 38,000$ heat flow measurements, gives the 47 ± 2 TW heat flow [21]. These estimates of the heat are in good agreement and are less than 0.1% of the incoming solar energy,

Radiogenic heat and decrease in the primordial heat content (secular cooling) constitutes the two primarily contributions to the total energy loss of the Earth. An insignificant amount of heat is produced due to tidal effects, chemical differentiation, crystallization in the D'' layer, etc. These minor sources produce no more than one percent of the total heat. The ratio of the radiogenic heat production to the surface heat flux is called the Urey ratio and is an important quantity characterizing heat production in the Earth.[6] The energy budget of the Earth is schematically presented in Fig. 3: the radiogenic heat production splits between the crust and the mantle, and the rest of the heat is provided by secular cooling that can be determined directly from ancient lava samples. The radiogenic heat production in the continental crust responsible for up to 50% of the Earth's total radiogenic heat can be determined within 10% precision. At the same time, radiogenic heat generation in the Earth's mantle remains uncertain, but its knowledge is important for geophysics in order to understand the Earth's convective engine, plates tectonics, and growth of continents. The latter process, in turn, tends to deplete radioactive elements in the Earth's mantle. The measurement of the geoneutrino fluxes that are directly bound to the amount of the heat producing elements (HPEs) can provide better constrains to the Earth's energy

---

[5] The errors in Eqs. (8) and (9) can be partially or fully correlated, especially for the U and Th contributions. The equations adapted from [3].

[6] The Urey ratio is named after Harold Urey, the 1934 Nobel Prize laureate in Chemistry for the discovery of deuterium, as recognition of his contribution to cosmochemistry. As noted by Korenaga [22], this key parameter for a planetary thermal budget could be a source of confusion because geophysicists and geochemists have defined the ratio in different ways. Two different Urey ratios are being used: the bulk Earth Urey ratio and the convective Urey ratio. The bulk Earth Urey ratio in the geochemical literature usually denotes the contribution of internal heat generation in the entire Earth to the total surface heat flux. In contrast, the convective Urey ratio is the ratio of internal heat generation in the mantle over the mantle heat flux. The latter definition is the original one introduced by Christensen [23] for his parameterized convection models, and is commonly used by geophysicists while discussing the thermal history of the Earth. The contribution of continental crust does not directly participate in convective heat transfer and is excluded from both the internal heating budget and the surface heat flux.
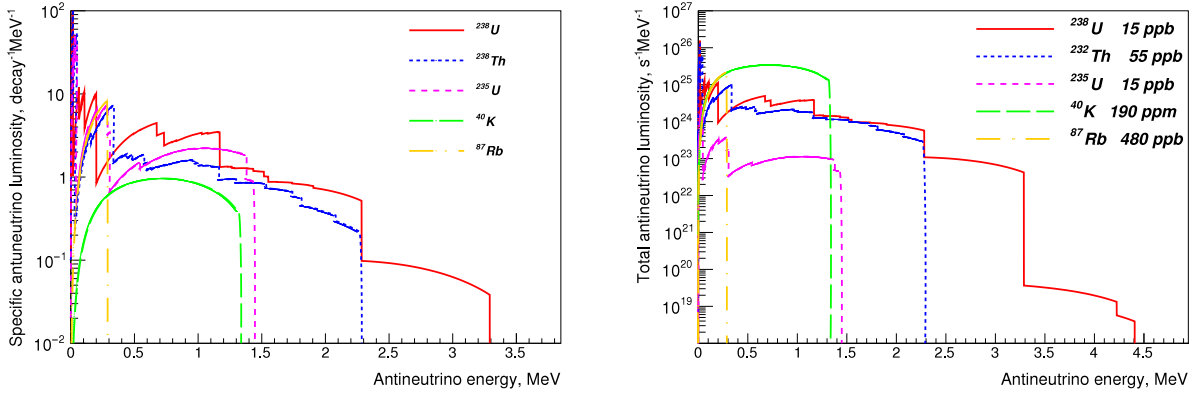
Fig. 4. The antineutrino energy spectra normalized to one decay of the parent nucleus (left plot), and total antineutrino differential luminosities (right plot). The abundances, used in calculation, are shown after each isotope notation [18].
Source: Figure adapted from [3].

budgets. Because of the variations of the crust thickness, the geoneutrino flux measurements in different geographical locations will help separating a much less position-dependent mantle contribution.

The total luminosity L_ν and hence the related heat production H_R can be estimated using the geoneutrino flux measured by the antineutrino detector. The geoneutrino flux measured at a certain position depends on the distribution of radioactive isotopes in the Earth bulk and varies within an order of magnitude for different locations on the Earth's surface [24]. One should also take into account neutrino oscillations when comparing the expected antineutrino flux with the measured one.

In stable continental regions, the main component of the heat flux is the crustal radioactivity. In oceanic areas the higher surface heat flux is due to the cooling of oceanic crust and bears no relation to radioactivity. In thermal equilibrium, the geoneutrino flux is expected to decrease over low heat flux regions and to increase over high heat flux regions [25].

3. Geoneutrino flux calculation

The antineutrino energy spectra normalized to one decay of the parent nucleus are shown in left plot of Fig. 4. The differential total antineutrino luminosities of the Earth ($\frac{dL_\nu(E)}{dE}$) calculated using abundances of natural isotopes in the Earth from [18] are shown in the right plot of Fig. 4.

Geoneutrino flux at the detector's location can be calculated by integrating the antineutrino fluxes from all possible points of origin in the Earth and summing over all contributing β-decays. We assume that non-electronic antineutrino species are lost for the detection and take into account the electron antineutrino survival probability P_{ee}

$$\phi_I(E_\nu) = n_I(E_\nu) \cdot \int_{V_{Earth}} \frac{\rho(\overrightarrow{r})}{4\pi |\overrightarrow{R_D} - \overrightarrow{r}|^2} \cdot A_I(\overrightarrow{r}) \cdot P_{ee}(E_\nu, |\overrightarrow{R_D} - \overrightarrow{r}|) d\overrightarrow{r}, \tag{10}$$

where the index $I = \{U, Th\}$ denotes the U or Th chain (the summation should be extended to include ^{40}K and/or other species if needed), $\rho(\overrightarrow{r})$ is the Earth's density at position $\overrightarrow{r}$, $n_I(E_\nu)$ is the antineutrino energy spectrum in the corresponding chain normalized to the number of antineutrinos emitted in the chain ($\int n_{Th}(E)dE = 4$, $\int n_U(E)dE = 6$), $\overrightarrow{R_D}$ is the position of the detector, integration is performed over the Earth's volume V_{Earth}, and $P_{ee}(E, L)$ is the electron antineutrino survival probability for the antineutrino energy E at distance $L = |\overrightarrow{R_D} - \overrightarrow{r}|$ from the antineutrino source. $A_I(\overrightarrow{r})$ is the specific activity of the chain I at the position with coordinates $\overrightarrow{r}$

$$A_I(\overrightarrow{r}) = \frac{a_I(\overrightarrow{r}) \cdot C_I}{\tau_I m_I}, \tag{11}$$

where $a_I(\overrightarrow{r})$ is the mass abundance of the corresponding parent element, and C_I, τ_I, and m_I are the isotopic abundance, life-time, and atomic mass of the isotope, respectively.

3.1. Neutrino oscillations

The electron neutrino survival probability appears in Eq. (10) because the cross section of the neutrino interaction with the active media of the detector depends on the neutrino flavour. All existing neutrino oscillation data (with a few exceptions indicating the presence of the fourth hypothetical sterile neutrino, a case that goes beyond the scope of the review) can be described assuming a 3-flavour neutrino mixing in vacuum. Mass eigenstates correspond to mass states

of neutrinos, called ν_1, ν_2 and ν_3. It follows from experimental data that neutrinos must be light with m_1, m_2, and m_3 below 1 eV, and all the three ones must have different masses to allow for oscillations, while the lightest neutrino still can be massless. The "usual" flavour states produced in nuclear reactions are the mixture of the mass eigenstates, the composition of which can change as a neutrino propagates. We can state that at present all properties of the mixing matrix describing neutrino mixing are well established experimentally with respect to the precision needed for the geoneutrino flux estimations. The electron antineutrino, being born in β-decay as a mass state mixture corresponding to the electron flavour, after travelling a distance $L = |\vec{R_D} - \vec{r}|$ could be detected as another flavour with a certain probability. The distant observer will still detect these neutrinos in electron flavour with a (survival) probability P_{ee}, while the complementary probability 1-P_{ee} remains for observing other neutrino flavours. If a detector is unable to register non-electron neutrino flavours, the factor P_{ee} should be applied to obtain the electron flavour component. In the general case (e.g. in the case of a hypothetical detector sensitive to the neutrino elastic scattering) one should also take into account the presence of other flavour components.

The three-flavour electron neutrino survival probability is (see e.g. [26]):

$$P_{ee}^{3\nu}(E_\nu, L) = 1 - \left(\cos^4\theta_{13}\sin^2 2\theta_{12} \cdot \Delta_{21} + \sin^2 2\theta_{13}\left[\cos^2\theta_{12} \cdot \Delta_{31} + \sin^2\theta_{12} \cdot \Delta_{32}\right]\right), \tag{12}$$

where θ_{12} and θ_{23} are the mixing angles, and Δ_{ij} is defined as

$$\Delta_{ij} = \sin^2\left(1.27|\Delta m_{ij}^2|[\text{eV}^2]\frac{L[\text{m}]}{E_\nu[\text{MeV}]}\right), \tag{13}$$

with $\Delta m_{ij}^2 = m_i^2 - m_j^2$, the neutrino mass squared difference. Note that by definition we have only two independent mass squared differences because of $\Delta m_{31}^2 = \Delta m_{32}^2 + \Delta m_{21}^2$. The values of Δm_{21}^2 and Δm_{31}^2 are measured in oscillation experiments, and one of the two independent mass squared differences, say Δm_{21}^2, turns out to be much smaller in absolute value than the second one $|\Delta m_{21}^2| \ll |\Delta m_{32}^2|$, providing that $\Delta m_{31}^2 \approx \Delta m_{32}^2$. Neutrino experiments data imply $\Delta m_{21}^2 = (7.37 \pm 0.17) \cdot 10^{-5}$ eV^2 and $\Delta m_{31}^2 \simeq (2.525 \pm 0.030) \cdot 10^{-3}$ eV^2 [27]. Formula (12) can be used directly in precise calculations.

It is convenient to introduce the length of oscillations L_{osc}. The phase in Eq. (13) that is responsible for oscillations can be written as $\pi\frac{L}{L_{osc}}$ the length of oscillation L_{osc} is then defined as

$$L_{osc} = \frac{\pi}{1.27}\frac{E_\nu[\text{MeV}]}{|\Delta m^2|[\text{eV}^2]}[\text{m}]. \tag{14}$$

There are two distinct length scales for oscillation, defined by two very different Δm^2, as noted above. For a given Δm^2, the length of oscillation depends only on energy.

The survival probability can be approximated by averaging over fast-oscillating terms for energies in the range of interest (below the maximum energy of 3.27 MeV in the geoneutrino spectra). Indeed, the length of oscillations for Δm_{12}^2 is of the order of 100 km, and for $\Delta m_{32}^2(\Delta m_{31}^2)$ it is even less. Both lengths are small compared to the Earth radius of 6400 km, and the average survival probability is:

$$\langle P_{ee}^{3\nu}(E_\nu, L)\rangle \simeq 1 - 0.5\left(\cos^4\theta_{13}\sin^2 2\theta_{12} + \sin^2 2\theta_{13}\right). \tag{15}$$

Using $\sin^2\theta_{13} = 0.0215 \pm 0.007$ and $\sin^2\theta_{12} = 0.297 \pm 0.017$ [27], we obtain the electron antineutrino survival probability

$$\langle P_{ee}\rangle = 0.558 \pm 0.015, \tag{16}$$

which can be used in estimations instead of (12). The uncertainty quoted for $\langle P_{ee}\rangle$ is evaluated using the uncertainties of the parameters involved in the calculations, and the error on substitution of P_{ee} by its average value is omitted here, since it depends on the method of detection and the detector's geographical position. The substitution of $P_{ee}(E_\nu, L)$ by its average value can also lead to distortion of the geoneutrino spectrum, which can in principle induce additional systematic errors in far future high statistics geoneutrino spectral fits, possibly larger than the error on the absolute value of $\langle P_{ee}\rangle$. For example, more detailed evaluations performed for the Jinping site [28] give P_{ee} values growing linearly from 0.55 for $E \sim 0$ to 0.56 at $E = 3$ MeV, with the average over the geoneutrino spectrum $\langle P_{ee}\rangle = 0.553$ and the effective average $\langle P_{ee}\rangle = 0.562$, calculated by weighting over the cross section of the detection reaction, which is inverse β-decay of the proton in this case.[7] Similar estimates are provided by Dye in [30], where he reports an upward shift and distortion of the energy spectrum introduced by using the average oscillation probability. Uranium and thorium within one oscillation length to the detector cause an increase of the survival probability, making the effect more pronounced on continental crust than on oceanic crust. The $P_{ee}/\langle P_{ee}\rangle$ ratio for the continental crust is growing almost linearly from 1.015 at 1.8 MeV to 1.04 at 3.5 MeV. The estimated deviations are in average within the precision of (16), well beyond the sensitivity of modern and near future geoneutrino detection facilities.

---

[7] These calculations are based on the earlier compilation of the oscillation parameters from [29].
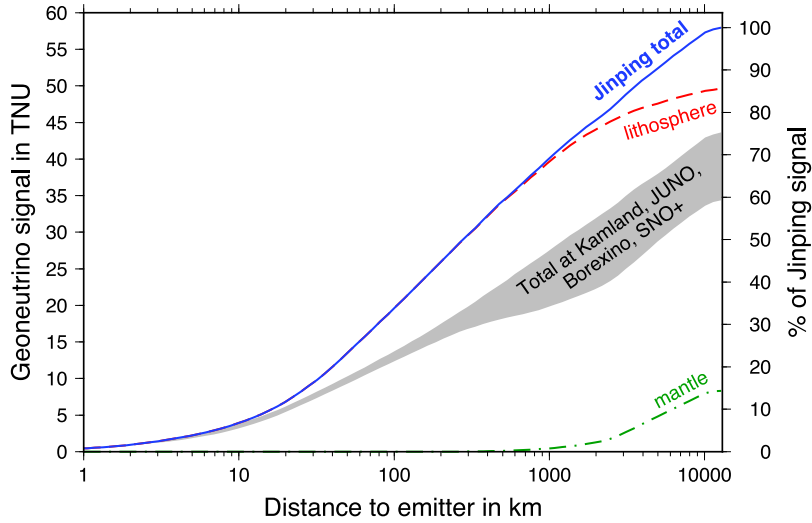
Fig. 5. Cumulative geoneutrino signal versus distance to the fixed detector location. Geoneutrino signal is expressed in absolute units (left vertical axis, see Section 4 for TNU definition) and as a percentage of the total signal expected at the Jinping location (right vertical axis). Contributions from lithosphere and mantle to the total Jinping signal are shown separately (denoted as "lithosphere" and "mantle" in the plot). Grey shaded area envelops signals at other detectors. (Figure from Šrámek et al. [33], reproduced under Creative Commons Attribution 4.0 International License [34]).

With the average electron neutrino survival probability, the formula for the antineutrino spectrum reduces to

$$\phi_I(E_\nu) = n_I(E_\nu) \cdot \langle P_{ee} \rangle \cdot \int\limits_{V_{Earth}} \frac{\rho(\overrightarrow{r})}{4\pi |\overrightarrow{R_D} - \overrightarrow{r}|^2} \cdot A_I(\overrightarrow{r}) \cdot d\overrightarrow{r}, \tag{17}$$

where the term defined by the integral is the full flux of the antineutrino Φ_I from the isotope I expressed in usual flux units of cm^{-2} s^{-1}, and the antineutrino spectrum at the detector from the isotope I is

$$\phi_I(E_\nu) = n_I(E_\nu) \cdot \langle P_{ee} \rangle \cdot \Phi_I, \tag{18}$$

All calculations above are performed for the case of vacuum oscillations neglecting the matter effect. While neutrinos travel through dense matter (in our case through the Earth) their mixing angles acquire a density-dependent matter term. In fact, the electron neutrino interacts through charged and neutral currents with electrons in the medium, while those of other flavours interact through neutral currents only. As a result, a difference in the potential of interaction for electronic and other flavours appears, $-\sqrt{2}G_F n_e$, where n_e is the electron density and G_F is the Fermi constant. In the case of constant density, the matter effect changes the mixing angles and masses, and the basic oscillation formula can be used with the corresponding substitutions. In the case of varying matter density, the calculations are more complex. The electron density in the Earth indeed varies with depth. The changes in density are especially noticeable at the boundaries of different layers of Earth. The steep changes of electron density complicate the prediction of survival probability, because changes in the wave function depend on the state of the wave function and the speed of the variation. The survival probabilities were calculated by solving numerically equations of motion in [31,32]. It was concluded that the matter effect increases the survival probability by ~2%, and the spectral distortions (deviations from the average for different point of production) are below 1%. The corresponding systematics should be taken into account when using the formula for the vacuum oscillations.

3.2. Modelling the distribution of heat producing elements

The geoneutrino flux at a certain position depends on the distribution of radioactive isotopes in the Earth bulk; in basic formula (10) it is the $\rho(\overrightarrow{r})A_I(\overrightarrow{r})$ term. Calculations show that the geoneutrino flux varies within an order of magnitude for different locations over the Earth's surface because of the non-uniformities in isotope distribution. Half of the total antineutrino flux arrives from distances of no more than 500 km, and the closest 50 km contribute a quarter of the total. Thus, the local area around the laboratory is the most important contributor to the total signal, see Fig. 5. The mantle contribution at these distances is still negligible as the typical HPEs abundances are three orders of magnitudes lower compared to the crustal abundances.

The information on density $\rho(\overrightarrow{r})$ comes from seismic studies. The simplified structure of the Earth is well described by the Preliminary Reference Earth Model (PREM) [35], a one-dimensional model representing the average Earth properties as a function of the planetary radius. It provides, in particular, a table of the Earth density as a function of the radius that can be used in calculation. The Earth interior is structured in the following way: from surface to centre, a thin crust

(thicker continental, ∼35 km in average, and thinner oceanic, ∼8 km) and a mantle (∼2900 km), both of which are made up of silicates, and a Fe–Ni alloy core (∼3500 km). The PREM tables can be used for the mantle densities. The mantle volume is generally further subdivided in two parts: the main spherical shell extending from the core–mantle boundary (CMB) to about 80 km beneath the surface and a smaller mantle volume in between the main shell and beneath the oceanic crust.[8] The latter breaks the spherical symmetry of the geophysical response at the observation sites.

The contribution from the mantle is model dependent. The so-called Bulk Silicate Earth models (BSE, for their review see [36]) predict abundances of the heat producing elements (HPEs) in the primordial mantle and assume that the total mass of the corresponding element is at present distributed between the crust and the mantle. Hence, the mass of HPEs in the mantle can be estimated withing the BSE model by subtracting the mass of the HPEs in the crust from the total one. Then the geoneutrino signal from the mantle can be calculated considering different possible distributions of the remaining mass of the HPEs across the mantle.

A map of the density of the Earth's crust is provided by more detailed three-dimensional models. The most recent are CRUST 1.0 [37] and LITHO 1.0 [38]. CRUST 1.0 provides 8 structural layers defined in $1° \times 1°$ cells: water, ice, upper, middle, and lower sediments, and upper, middle, and lower crystalline crust. LITHO 1.0 is a $1°$ tessellated model of the crust and the uppermost mantle of the Earth extending into the upper mantle to include the lithospheric lid and the underlying asthenosphere. The model is parameterized laterally by tessellated nodes and vertically as a series of geophysically identified layers, similar to CRUST 1.0 with the additional lithospheric lid and the asthenosphere.[9] Details can be found in [38].

The values of the HPEs concentration $A_l(\overrightarrow{r})$ are assigned to various crustal layers of the model. Earlier calculations were based on CRUST 5.1 (a global crustal model with $5° \times 5°$ cells) [39] and its update to $2° \times 2°$ cells (CRUST 2.0) [40]. In particular, the reference model by Fiorentini et al. [41], further developed by Huang et al. [24], is based on the global CRUST 2.0 model. CRUST 2.0 provides a detailed crustal column for $2° \times 2°$ cells, which is not constrained by geophysical measurements but only inferred from the geological type. A "characteristic" crustal column consists of 7 layers with different composition and physical properties for each geological type (based on age and tectonic setting) and is assigned to each cell depending on its geology. In accordance with Mareschal et al. [42], it is an oversimplification, because it does not account for the heterogeneity of the continental crust. These reference models provide a useful starting point for interpreting geoneutrino observations. However, its practical use is questioned by Mareschal et al. [42], who note that though CRUST 2.0 (and similarly its refined $1° \times 1°$ version) uses a compilation of seismic data, it is still a model. Neither CRUST 1.0 nor LITHO 1.0 provides uncertainties on the thickness of crustal layers or rock density. Šrámek et al. in [33] expect them to be of the order of 5–10%, but arguments for this estimate are not provided. Huang et al. [24] note that uncertainties in Moho depths[10] are a major source of uncertainty in the global crustal model. The previous 3SMAC topographic model [43] included the analysis of crust–mantle boundary developed by Čadek and Martinec [44], in which the average uncertainties of continental and oceanic crustal thickness are 5 km and 3 km (1σ) respectively in agreement with the expectations of [33]. Mareschal et al. in [42] report that crustal thickness of CRUST 1.0 differs by up to 30% from the real data of the seismic studies in Ontario and Quebec. Dye [45] notes that a potentially significant source of systematic uncertainty is lateral heterogeneity of the terrestrial U and Th distributions. Whereas oceanic crust is quite uniform in composition, lateral heterogeneity certainly exists in the continental crust, as evidenced by uranium mining at specific locations.

Šrámek et al. in [33] tested predictions of CRUST 1.0 against LITHO 1.0 for Jinping location. The results differ by ∼5%. The LITHO 1.0-based model prediction is higher, consistent with the LITHO 1.0 Continental Crust (CC) around Jinping being thicker compared to the CC of CRUST 1.0; globally the CC in LITHO 1.0 is 13% more massive than in CRUST 1.0.

Local area contribution

The use of a simplified global model could lead to a significant systematic error in antineutrino flux evaluation. The most sensitive parts are the regions closest to the detector. The systematics induced by the crustal model can be reduced by supplementing models with detailed topographic information. In fact, ∼25% of all geoneutrinos arrive from distances below 50 km, which is within a $1° \times 1°$ cell, and ∼50% of all antineutrinos arrive from a distance below 500 km; thus, the detailed description of the local area reduces the error of the most sensitive part. For example, after the evaluation of the local contribution to the geoneutrino signal at the Gran Sasso National Laboratory (LNGS) on the basis of a detailed geological, geochemical, and geophysical study of the region, the total predicted flux was reduced by 10% [46], compared to the previous calculation based on general worldwide average assumptions. The reason is the presence of a relatively thick

---

[8] This is a geophysical mantle subdivision; the geochemical separation into Enriched Mantle and Depleted Mantle has different discontinuities and volumes, see also next comment.

[9] Lithosphere is the rigid outer conductive part of the Earth, consisting of the crust and the mechanically coupled upper layer of the mantle beneath it; asthenosphere is the upper layer of the Earth's mantle below the lithosphere, in which convection is thought to occur. The both terms belong to the mechanical (or rheological) Earth layer subdivision, which includes the lithosphere, asthenosphere, mesospheric mantle, outer core, and inner core. More popular is chemical subdivision of the Earth regions into the crust, the mantle (further subdivided into the upper and lower mantle), and the core, which can also be subdivided into the outer core and inner core.

[10] Mohorovičić discontinuity (Moho) corresponds to the boundary between the Earth's crust and its mantle. The Moho lies at a depth of about 35 km below the continents and about 7 km beneath the oceanic crust and is contained almost entirely within the lithosphere.

layer of sediments significantly depleted in U and Th, which was not considered in more general studies. Thus, the need for detailed integrated geological study is underlined by this work. The rest of the crust does not need precise mapping of the geological regions and depends mainly on the total quantity of HPEs. The estimates of the local contributions to the geoneutrino signal are available for the laboratories hosting or planning to host the geoneutrino experiments. These estimates will be discussed in detail in the sections devoted to the related experiments.

Large mantle structures

A homogeneous composition of seismically differentiated regions in the mantle is usually assumed in models. However, there is experimental evidence of inhomogeneities in the deep mantle. The global seismic tomography reveals two large low shear velocity provinces (LLSVP) at the base of the mantle off the west coast of Africa and near Tahiti in the South Pacific [47] with indication of a composition different from the surrounding mantle [36]. Šrámek et al. [36] examined the influence of the chemical composition changes on the mantle signal. The studies demonstrate that the mantle geoneutrino flux at the Earth's surface will have two distinct maxima at about $+20\%$ of the average mantle flux above the LLSVPs, assuming the mantle is depleted in U and Th with respect to the LLSVPs.

Roskovec et al. [48] considered the search for the so-called "second continents", hypothesized gravitationally stabilized regions enriched with upper crustal concentration levels of radiogenic elements at a depth of 600 to 700 km. The geoneutrino flux in these second continents can be detected with land- and/or ocean-based detectors.

3.3. Models of the Earth

The models discussed above provide the density at the given position of the mantle (PREM) and constrain the crust properties assigning the concentrations of HPEs to each of the crustal/lithospheric types. To complete the model and obtain the global distribution of HPEs, one needs a set of abundances of these elements in the mantle. The common major assumptions are:

- the core of the Earth does not contain HPEs, since U, Th, and K are lithophile elements having affinity to the silicate minerals and melts, and should not be present in the Earth's core;
- the BSE concept is used to calculate partitioning of the elements. The BSE model provides chemical composition considers of the primordial mantle, namely the mantle at the moment just after the core separation but prior to the start of the crust formation[11];
- during the formation of the Earth's crust, the mantle was depleted in U and Th, while the continental crust was highly enriched in these HPEs. The crustal abundances can be derived from the direct measurements, and the mantle abundances can be calculated using the BSE constraint;
- the homogeneous composition of seismically differentiated mantle regions is usually assumed in the model.

The BSE model is in good agreement with the majority of experimental observations concerning the core and the upper mantle. The composition of the primitive mantle is derived from the composition of the chondritic meteorites, representing the majority of stone meteorites, with some corrections for the observed abundances in the Earth. The composition of chondrite meteorites is practically identical to the chemical composition of the Sun, excluding the lightest elements, such as hydrogen and helium. It is assumed that chondrites originate from protoplanet matter surrounding the Sun by condensation and accretion of the dust with intermediate heating. Chondrites do not show traces of melting and correspond to non-differentiated planets (planets without crust), i.e., to the composition of the primitive mantle. Compositional models of the Earth can be grouped into three major classes in accordance with the total predicted radiogenic heat of the Earth [49,50]: low-Q models (10–15 TW), medium-Q models (17–22 TW), and high-Q models (> 25 TW):

- **Low-Q models** (**cosmochemical**): these models state either that the Earth accreted with low quantities of Th and U (Enstatite Earth model, [51–54]) or that in the early stages of accretion the planet lost up to half of its crust enriched in Th and U in collisions with massive external bodies (the Collisional Erosion model [55–58]). The latter is one of the variations of the Non-Chondritic model [59]). It is based on the composition of enstatite chondrites having the closest isotopic similarity to the mantle samples and possessing high enough iron content to explain the metallic core. The studies supporting the enstatite chondrite-derived composition are provided by Warren [57] and Zhang et al. [60]. Models predict U concentration of 12 ± 2 ppb.[12]
- **Medium-Q models (geochemical):** these models use samples of the Earth's mantle, constraining the abundance ratios to those of the carbonaceous chondrites[13] similar to the solar photosphere in content of refractory lithophile

---

[11] According to McDonough and Sun [18] the Silicate Earth and Primitive Mantle are synonymous.

[12] ppb, parts per billion, is used to describe low concentration of substances, 1 ppb corresponds to 10^{-9} g/g and equals 1 ng of substance per g of solid (ng/g).

[13] The class of carbonaceous chondrites meteorites is usually denoted CI, here "C" is for carbon and "I" is the first letter of the Ivuna location, where this class of meteorites was first found.

Table 2

Estimates of HPEs abundances and corresponding radiogenic power for BSE in cosmochemical, geochemical, and geodynamical models, compiled by Šrámek et al. [36]. The BSE mass is $\sim 4 \times 10^{24}$ kg, and the corresponding total mass of HPE can be obtained multiplying its abundance by the BSE mass.

Parameter	Cosmochemical (Low-Q)	Geochemical (Medium-Q)	Geodynamical (High-Q)
a_U (ppb)	12 ± 2	20 ± 4	35 ± 4
a_{Th} (ppb)	43 ± 4	80 ± 13	140 ± 14
a_K (ppm)	146 ± 29	280 ± 60	350 ± 35
Th/U	3.5	4.0	4.0
K/U	12,000	14,000	10,000
Q_H (TW)	11 ± 2	20 ± 4	33 ± 3

Table 3

Global masses of U, M(Th)/M(U) ratio, and the corresponding radiogenic heat production H(U+Th) in the Earth according to different BSE models (compiled by Huang et al. [73]).

Reference	M(U) (10^{17} kg)	M(Th)/M(U)	H (TW)
Javoy et al. [52]	0.5	3.5	9.2
Lyubetskaya and Korenaga [67]	0.7	3.7	13.4
McDonough and Sun [18]	0.8	3.9	16.2
Allegre et al. [65]	0.8	3.9	16.2
Palme and O'Neil [66]	0.9	3.8	17.6
Anderson [74]	1.1	4.0	23.0
Turcotte and Schubert [71]	1.2	4.0	25.4

elements (having affinity to silicate minerals and melts), siderophile elements (affinity to iron), and volatile elements [18,61–67]. A typical chondritic ratio of Th/U masses is 3.9[14] and K/U masses $\sim$14000. Typical U concentration in these models is 20 ± 4 ppb. The underlying strong assumption is that by sampling the top of the Earth one can restore the bulk composition of the mantle, i.e., the mantle is roughly homogeneous in composition.

- **High-Q models (geodynamical):** these models are based on a physical approach with a boundary condition given by the surface heat flux, and on the simple relationship between the heat output from the convecting mantle and the vigor of convection described as a balance between thermal buoyancy driving the dynamics and thermal and momentum diffusion hindering the flow [69–72]. Trade-offs between buoyancy and viscosity versus thermal and momentum diffusion rates allow for a range of solutions that can include Low- to High-Q models. Typical U concentration in these models is 35 ± 4 ppb.

The compositional predictions of these three models for the BSE are shown in Table 2. The more detailed compilation of estimates for the abundances of HPEs for different Earth reservoirs: bulk continental crust, bulk oceanic crust, bulk mantle, and depleted mantle, can be found in Šrámek et al. [36] together with estimates of power in TW and the mantle Urey ratio.

Global masses of U, Th/U mass ratio, and radiogenic heat production H(U+Th) in the Earth according to different classes of BSE models are shown in Table 3.

The Earth's crust is highly enriched in U and Th, while its mass is much less than that of the mantle. Therefore, the crustal geoneutrino contribution dominates in continental observatories. The prediction for the crust contribution is bounded more strongly than the mantle contribution, the latter can be obtained extracting the crust contribution from the total. The difference in heat output of the models is in fact defined by the mantle contribution and the variability of predictions of the mantle heat is more pronounced as compared to the total heat, namely : (3 ± 2) TW for cosmochemical, (12 ± 4) TW for geochemical and (25 ± 3) TW for geodynamical models. Therefore, the measurement of the geoneutrino signal from the mantle is a clue to distinguishing between the existing models. Moreover, geoneutrinos are a tool for studying the identified large-scale mantle structures, as discussed in the previous section.

4. Detection of antineutrinos

Antineutrino spectra expected from the ^{238}U and ^{232}Th chains, as well as from the ^{40}K decay, are presented in Fig. 4. A fraction of antineutrino spectra from the ^{238}U and ^{232}Th chains exceeds the threshold of the inverse beta-decay (IBD) of the free proton.[15] This makes possible registration of antineutrino by liquid scintillation detectors in the IBD of the

---

[14] Wipperfurth et al. recently reported the results of their high precision study of the mass ratio in [68], which they found to be M(Th)/M(U) = $3.776^{+0.122}_{-0.075}$. We use a commonly accepted value of 3.9 throughout the text, as it has been used in all experimental publications until now, and it is still compatible with the value of Wipperfurth et al. within the 1σ uncertainty.

[15] Inverse beta-decay of the free proton is commonly abbreviated as IBD without mentioning the free proton. We will follow this convention if not stated otherwise explicitly.

Table 4

Locations and rock overburden in metres of water equivalent (m.w.e.) of existing labs hosting or having plans to build a geoneutrino detector, existing or approved facilities are highlighted by bold. The last 4 rows present correspondingly: the total expected reactor antineutrino signal (FER stays for full energy range), the expected reactor antineutrino signal in the geoneutrino energy window (GEW, $E_{\overline{\nu_e}} < 3.27$ MeV), the predicted geoneutrino signal and the reactor/geoneutrino ratio for the relevant energy range. The calculations for KamLAND are performed for the actual situation with Japanese reactors off. The data on the predicted reactor signals are compiled using the estimates from [75–77]. The geoneutrino signals were calculated by Huang et al. in [24] using their Reference EARTH Model.

Laboratory	LNGS	Kamioka	Sudbury	Jinping	Jiangmen	Baksan	Pyhäsalmi	Hawaii
longitude	42.55°N	36.42°N	46.475 °N	28.15°N	22.12°N	43.24°N	63.66°N	19.72°N
latitude	13.57°W	137.31°W	81.20°W	101.71°E	112.51°E	42.70°E	26.04°E	156.32°W
depth, m.w.e.	3000	2700	6000	6720	2100	4900	4000	4−5000
Detector/proposal	Borexino	KamLAND	SNO+	Jinping	JUNO	Baksan	LENA	Hanohano
S(R)$_{FER}$ (TNU)	$85.2^{+2.0}_{-1.8}$	$27.4^{+0.6}_{-0.6}$	$193.9^{+4.7}_{-4.5}$	27.8	1569 ± 88	$37.4^{+0.9}_{-0.8}$	$69.5^{+1.7}_{-1.6}$	$3.4^{+0.08}_{-0.07}$
S(R)$_{GEW}$ (TNU)	$22.9^{+0.6}_{-0.5}$	$7.4^{+0.2}_{-0.2}$	$48.8^{+1.7}_{-1.5}$	6.8	351 ± 27	$9.96^{+0.28}_{-0.27}$	$18.0^{+0.5}_{-0.5}$	$0.9^{+0.02}_{-0.02}$
S(U+Th) (TNU)	$40.3^{+7.3}_{-5.8}$	$31.5^{+4.9}_{-4.1}$	$45.4^{+7.5}_{-6.3}$	59.4 ± 6.8	$39.7^{+6.5}_{-5.2}$	$47.2^{+7.7}_{-6.4}$	$45.5^{+6.9}_{-5.9}$	$12.0^{+0.7}_{-0.6}$
S(R$_{GEW}$)/S(U+Th)	0.6	0.2	1.1	0.1	8.8	0.2	0.4	0.1

proton $\overline{\nu}_e + p \longrightarrow e^+ + n$ with a threshold of $E_\nu \simeq 1.8$ MeV. Today, all the available data on geoneutrinos are obtained with this detection technique, and the near future detectors will also use the IBD for the geoneutrino detection. It should be noted that at the moment there are no dedicated projects aimed at the geoneutrino studies. The projects have different primary goals, such as solar neutrino studies in Borexino or reactor antineutrino studies in KamLAND, and the geoneutrino studies are merely an extension of the mainstream programme. The need for the detectors with lower threshold for ^{40}K detection and potential advantages of geoneutrino directional studies can trigger development of specialized detectors based on other principles. These possibilities will be discussed later.

A convenient unit to describe the rate of interactions in the IBD detectors is a Terrestrial Neutrino Unit (TNU) first introduced by Mantovani et al. in [41]. One TNU corresponds to 1 interaction for 10^{32} target protons in one year; 10^{32} target protons are contained in roughly 1 kt of typical liquid organic scintillator, and few years is a typical expected exposure time for the geoneutrino detection. Thus, the counting rate in TNU roughly corresponds to the expected event rate per year in a 1 kt scale IBD detector. Let us note that the TNU defined in this way is suitable only for the reaction of the IBD of the proton, in the case of other IBD reactions, the definition should be properly changed.

The characteristic features of the typical geoneutrino detector are its size and strong requirements on the backgrounds. Shielding against cosmogenic backgrounds needs a huge quantity of material and is easily achieved by placing the detector deep underground, in a mine or a tunnel under the mountain massif. There are few laboratories in the world suited to host large detectors. A list of the most relevant ones is presented in Table 4, and a more detailed list can be found in [75].

All the data on the geoneutrino obtained until now are provided by two experiments, in LNGS (Borexino) and at Kamioka (KamLAND). The SNO lab is ready to start the SNO+ experiment, and there are plans to use the future data from the JUNO detector for geoneutrino studies. The note on the primary goals also applies to these two upcoming experiments: the main goal of SNO+ will be neutrinoless double beta decay search, and JUNO challenges the problem of the mass hierarchy of neutrinos. The laboratory at Jinping plans to host two detectors able to search for geoneutrinos, but currently the final decision for the detector choice is missing. There are no approved experiments at other sites.

4.1. Antineutrino detection in IBD of the proton

The antineutrino detection reaction is the IBD of the proton:

$$\overline{\nu_e} + p \rightarrow n + e^+. \tag{19}$$

It was first applied in the pioneering research by F. Reines and C.L. Cowan who conducted the first experiment on reactor antineutrino detection. Liquid organic scintillators can be used as a detection medium, as it is rich in free protons and cheap, permitting construction of large detectors. At present, geoneutrino observations using IBD have been reported by two collaborations with the Borexino and KamLAND organic liquid scintillation detectors respectively.

The reaction has a relatively high kinematic threshold due to a difference in mass between the products and the reactants: $E_{th} = \frac{(m_n+m_e)^2 - m_p^2}{2m_p} = 1.806$ MeV, 2 keV higher than in the case where recoil energy is neglected. The kinematic threshold of the reaction makes it impossible to detect lower-energy antineutrinos in IBD detectors.

The energy of the incoming antineutrino E_ν is strongly correlated with the energy of the positron created as a result of the interaction. The positron takes away the energy $E_{kin} = E_\nu - 1.806$ MeV in the form of the kinetic energy with a negligible fraction of this excess energy left for the kinetic energy of the neutron. The kinetic energy of the positron is partially transformed into scintillation light detected by photosensitive elements of the detector - photomultiplier tubes (PMTs). The annihilation of the positron produces two gamma-quanta of 0.511 MeV energy each, also producing light

flashes in the scintillator through Compton scattering on electrons. Thus, the total amount of scintillation light corresponds to the visible energy

$$E_{vis} = E_{kin} + 2m_e = E_\nu - 0.784 \text{ MeV}. \tag{20}$$

Together with the positron, a neutron is released in reaction (19). This gives an opportunity to "tag" the reaction, looking for pairs of events correlated in space and time. Indeed, the neutron is thermalized very effectively in proton-rich media (in 10–20 collisions with protons), and the thermal neutron has a relatively high cross section of interaction with protons. It is captured on the proton with a typical time of 200–250 µs for liquid organic scintillators, releasing an easily-detectable monoenergetic gamma quantum

$$n + p \rightarrow D + \gamma (2.223 \text{ MeV}). \tag{21}$$

In large-volume detectors all 2.2 MeV of gamma energy are lost in Compton scattering on electrons and thus converted into light, and the gamma is effectively detected. Therefore, the "tag" is provided by a 2.2 MeV "delayed" event observed in coincidence with a "prompt" one. In a liquid organic scintillator another neutron capture reaction is possible: $^{12}C(n,\gamma)^{13}C$. In this case, a more energetic gamma quantum with $E_\gamma = 4.945$ MeV is emitted. The relative probability of the neutron capture is only about 1% of that of the capture on the proton due to the large difference in cross sections, and the contribution of this reaction is insignificant.

The time window defining the "true" coincidence can be chosen on the basis of the expected accidental coincidence rate and the life-time of the neutron with respect to the capture on the proton, the 5τ window is typically used in the low background environment. The tagging technique allows the effective reduction of the random coincidence background. Further improvement of the technique can be achieved by using the vertex reconstruction of prompt and delayed events offered by modern large-volume liquid scintillation detectors equipped with many photosensors. The position is reconstructed using arrival times of photons at each photosensor (for more details and examples of the technique see e.g. [31,78,79]). The position reconstruction is also essential for the reduction of the background from the construction materials in the active volume of the scintillator. The liquid scintillator (LS) should be contained in a transparent vessel separating LS from the non-scintillating buffer, both the thin nylon or thicker acryl are used in modern detectors. The material of the vessel is unavoidably less clean with respect to radioactive impurities than the LS. The inner section of the LS volume, called the fiducial volume (FV), provides the best signal-to-background ratio and is selected off-line using the position reconstruction code. In such a way, the remaining outer section serves as active shielding for the FV.

The typical drift distance of a neutron is few centimetres compared to ten centimetres of the typical position reconstruction precision, and two events in reactions (19) and (21) occur practically at the same position. Hence, another condition can be imposed on the pair of events: their positions should be reconstructed as close to each other as possible. The selection criteria should be based on the balance of the efficiency of the spatial cut and on the rate of accidental coincidences satisfying the applied cut. The efficiency of the spatial cut generally depends on the precision of the reconstruction algorithm. The two basic selection criteria, time and distance between events, can be combined with other specific features of two correlated events, e.g., by rejecting pairs containing α-like events.

Compared to low energy neutrino detection, antineutrino detection in few MeV energy range is relatively easier in the LS due to the possibility of using the delayed coincidence tag, and due to the fact that antineutrino detection reaction (19) for these energies has a higher cross section than the reaction of elastic neutrino-electron scattering used in neutrino detectors. The elastic geoneutrino (antineutrino) scattering off electrons will still contribute to the total untagged events counting rate, but it is a small effect compared to the natural background from elastic Solar neutrino scattering off electrons.

4.2. Cross section of IBD of the free proton

The total cross section for reaction (19) can be expressed in terms of the neutron lifetime τ_n and the neutron decay phase-space factor $f = 1.7152$ (includes the Coulomb, weak magnetism, recoil, and outer radiative corrections, but not the inner radiative corrections) neglecting terms of the order of E_ν/m_p as [80]

$$\sigma_n(E_\nu) \simeq \frac{2\pi^2}{m_e^5 \cdot f \cdot \tau_n} E_e p_e, \tag{22}$$

where $E_e = E_\nu - (m_n - m_p) = E_\nu - 1.293$ MeV is the positron energy neglecting the small neutron recoil energy, and p_e is the corresponding momentum, both measured in MeV. The numerical factor before $E_e p_e$ in (23) depends inversely on the neutron decay time; using a recent value $\tau_n = 880.3 \pm 1.1$ s [81], we obtain

$$\sigma_n(E_\nu) \simeq 9.57 \cdot 10^{-44} p_e E_e \text{ cm}^2. \tag{23}$$

The (small) energy-dependent outer radiative corrections to σ_{tot} are given in [82,83]. The corrections to the cross section of the order of E_ν/m_p, not negligible even at low energies, and the angular distribution of the positrons are described by Vogel and Beacom [84]. The relatively small outer radiative corrections of the order of α/π can be accurately evaluated if necessary [85], and the cross section of the inverse β-decay can be evaluated with an accuracy of up to ~0.2%.

The uncertainties of the IBD reaction cross section obtained in reactor experiments are an order of magnitude larger (1.4–3.0% [86–88]), dominated by the uncertainties of the number of target protons estimation, and the reactor-related uncertainties of the reactor power and time-dependent fuel composition, e.g., fission fractions.

A more general calculation of the neutrino-nucleon cross section in the energy range up to several hundred MeV was discussed by Strumia and Vissani in [89]. They provided a simple approximation of the result

$$\sigma_n(E_\nu) \simeq 10^{-43} p_e E_e \cdot E_\nu^{-0.07056 + 0.02018 \ln E_\nu - 0.001953 \ln^3 E_\nu} \text{ cm}^2 \tag{24}$$

that agrees within a few per-mille with the precise calculations for energies up to 300 MeV, and provides the comparably good total accuracy, the authors report 0.4% total precision at low energy.

The differential geoneutrino event rate at the detector is

$$\frac{dN}{dE_\nu} = n_p \sigma_n(E_\nu) \epsilon(E_\nu) \phi(E_\nu), \tag{25}$$

where n_p is the number of target protons within the FV of the detector, $\epsilon(E_\nu)$ is the detector efficiency at energy E_ν, and $\phi(E_\nu)$ is the differential electron antineutrino flux at the detector's location defined by (10).

4.3. Geoneutrino signal in the IBD antineutrino detector

The expected total geoneutrino signal S_I for the isotope I can be obtained by integrating (25) over energy from the reaction threshold to the maximum energy of the corresponding antineutrino flux

$$S_I = \int_E dE_\nu \cdot n_p \cdot \epsilon(E_\nu) \cdot \phi(E_\nu) \cdot \sigma_n(E_\nu) \simeq \langle P_{ee} \rangle \cdot \Phi_I \cdot n_p \cdot \int_E dE_\nu \cdot \epsilon(E_\nu) \cdot \sigma(E_\nu) \cdot n_I(E_\nu). \tag{26}$$

All the notations were introduced above, and the substitution of $P_{ee}(E_\nu, L)$ by its average value is performed in accordance with (18). Assuming the energy-independent detector efficiency, the term defined by the integral can be replaced with an average cross section

$$S_I = \langle P_{ee} \rangle \cdot \Phi_I \cdot n_p \cdot \epsilon \cdot \sigma_I, \tag{27}$$

where the average cross section σ_I is defined over the corresponding neutrino spectrum

$$\langle \sigma_I \rangle = \frac{\int_E dE_\nu \cdot n_I(E_\nu) \cdot \sigma_n(E_\nu)}{\int_E dE_\nu \cdot n_I(E_\nu)}. \tag{28}$$

Performing calculations for ^{238}U and ^{232}Th, one obtains

$$\langle \sigma_{238\text{U}} \rangle = (4.08 \pm 0.04) \times 10^{-45} \text{ cm}^{-2}, \tag{29}$$

$$\langle \sigma_{232\text{Th}} \rangle = (1.25 \pm 0.05) \times 10^{-45} \text{ cm}^{-2}. \tag{30}$$

The main contribution to the uncertainties are induced by the uncertainties of intensities and end-point energies of the corresponding transitions quoted in Tables 5 and 6. Since the IBD cross section increases fast, the small uncertainties of the end-point energy in the ^{238}U chain are inducing errors comparable to the ones due to the relatively larger uncertainties of the intensities of the transitions. Possible errors due to the deviations of β-spectra from the "universal" shape are not considered because of the lack of experimental measurements.

With the average cross sections, the geoneutrino signal for 1 year can be calculated as

$$N(I) = \langle \vec{P}_{ee} \rangle \cdot \epsilon \cdot \langle \sigma_I \rangle \cdot 10^{45} \cdot \frac{\Phi_I}{10^6} \cdot \frac{n_p}{10^{32}} \cdot \frac{3.156 \times 10^7}{10^7}, \tag{31}$$
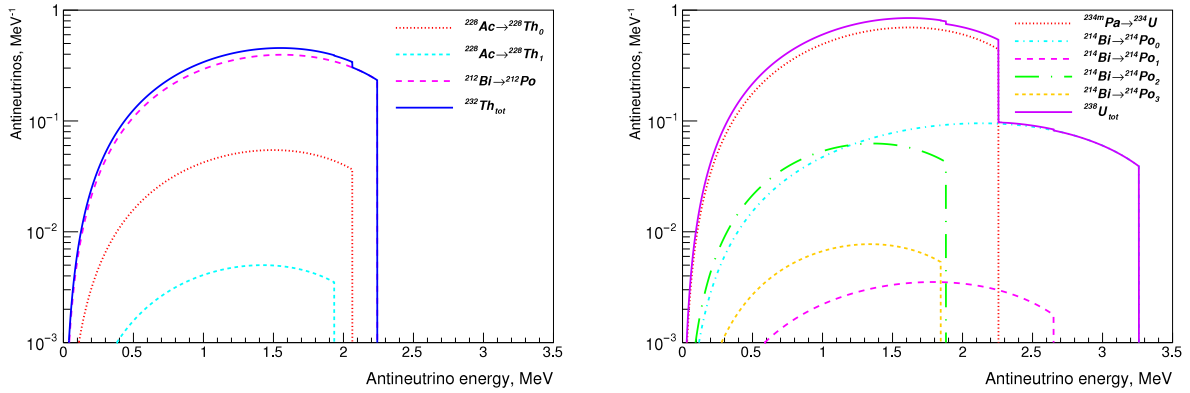
or

$$N(\text{U}) = (12.87 \pm 0.15) \cdot \langle P_{ee} \rangle \cdot \epsilon \cdot \frac{\Phi_\text{U}}{10^6} \cdot \frac{n_p}{10^{32}} \text{ yr}^{-1}, \tag{32}$$

$$N(\text{Th}) = (3.95 \pm 0.14) \cdot \langle P_{ee} \rangle \cdot \epsilon \cdot \frac{\Phi_\text{Th}}{10^6} \cdot \frac{n_p}{10^{32}} \text{ yr}^{-1}. \tag{33}$$

The geoneutrino signal expressed in TNU is usually quoted for 100% detector efficiency and depends on the corresponding geoneutrino flux as

$$S(\text{U}) = (12.87 \pm 0.15) \cdot \langle P_{ee} \rangle \cdot \frac{\Phi_\text{U}}{10^6} \text{ TNU} \simeq (7.2 \pm 0.2) \cdot \frac{\Phi_\text{U}}{10^6} \text{ TNU}, \tag{34}$$

$$S(\text{Th}) = (3.95 \pm 0.14) \cdot \langle P_{ee} \rangle \cdot \frac{\Phi_\text{Th}}{10^6} \text{ TNU} \simeq (2.2 \pm 0.1) \cdot \frac{\Phi_\text{Th}}{10^6} \text{ TNU}. \tag{35}$$

Fig. 6. Antineutrino spectra for β-decaying isotopes in the ^{232}Th (left) and ^{238}U (right) chains with the end-point energy $Q > 1.806$ MeV. The resulting total spectra are normalized to one parent decay. The end-point energies Q used in calculations are reported in Tables 5 and 6.
Source: Figure adapted from [3].

The errors on the average cross section and on the average oscillation probability are propagated quadratically. Only the error on the $\langle P_{ee} \rangle$ from (16) is considered, though further contributions to the total signal uncertainty are possible as discussed in 3.1.

In order to obtain the number of detected events, one should multiply the geoneutrino signal expressed in TNU by the detector efficiency and scale the exposure to 10^{32} protons yr. For the target mass of 10^{32} protons, 1 yr exposure with the detection efficiency $\epsilon = 1$, and $\langle P_{ee} \rangle = 0.558$, the detector would count (7.2 ± 0.2) events from the U chain and (2.2 ± 0.1) events from the Th chain for the incident flux of 10^6 cm^{-2} s^{-1}. Since the Th/U mass ratio of the Earth is M(Th)/M(U)$\simeq$3.9, and thorium activity for the unit mass is 3.1 times lower, one expects S(Th)/S(U)$\simeq$1/4, and though the global thorium mass is four times higher than that of uranium, it contributes only $\sim$1/5 to the total geoneutrino signal.

Because of the reaction threshold, the detection of antineutrinos from decays of ^{40}K and ^{87}Rb is impossible in IBD reaction. The same applies to all β-decays in the ^{235}U chain and most β-decays in the ^{238}U and ^{232}Th chains. Only two isotopes in each chain have energetic enough β-decays to provide a contribution to the IBD signal. In the ^{232}Th decay chain these are two branches of the ^{228}Ac decay (to ground state and to the first excited state), and the decay of the ^{212}Bi to the ground state. In the ^{238}U chain, these are the decays of ^{234} ^{m}Pa and 4 branches of the ^{214}Bi decay.

The properties of β-decaying isotopes in the ^{232}Th and ^{238}U chains contributing to the geoneutrino signal are presented in Tables 5 and 6, respectively. The second column contains activity of the corresponding reaction with respect to the activity of parent ^{232}Th (or ^{238}U). The $I \pm \delta I$ column contains the relative intensity of the corresponding decay (with respect to one parent decay) with the associated experimental error. Q is the β-decay end-point. f_{Th}, f_U and f_{tot} denote the fraction of the signal in the ^{232}Th, ^{238}U) chain and in total geoneutrino signal respectively. The neutrino spectra for U and Th are shown in Fig. 6. The corresponding neutrino signals expected in the IBD detector for the U and Th chains are shown in Fig. 7.

As one can see from Table 5, the contribution from the ^{228}Ac is quite uncertain. It contributes 0.8% to the total antineutrino signal uncertainty because of the poorly measured relative intensity of the decay. Uncertainty of the ^{214}Bi decay intensity to the ground state contributes another 0.4% to the total error of the signal. The uncertainties of the end-point of the more energetic transitions in the U chain give another 0.8% to the uncertainty of the total signal. Summed quadratically, these contributions constitute 1.2%, and other transitions in both decay chains do not contribute significantly to the total signal uncertainty. The uncertainties induced by the approximations used in β-decay shape calculation can, in principle, contribute to the total signal uncertainty, and these errors cannot be, in general, propagated quadratically because of the unknown correlations.

The total neutrino spectrum calculated for the chondritic ratio of Th/U masses M(Th)/M(U) = 3.9 is shown in the left plot of Fig. 8. Theoretical IBD spectra from the U and Th chains on the assumption of the secular equilibrium in the chains and at the chondritic ratio of Th/U masses are shown in the right plot of Fig. 8. The spectra are calculated for an ideal detector with an infinite resolution The visible difference in the spectra makes contributions from the U and Th potentially distinguishable, though the low-energy part of the U spectrum has a noticeable contribution very similar to the Th spectrum, weakening the discrimination power of the U and Th signals. The separation of the U and Th contributions will be discussed in Section 6.3.
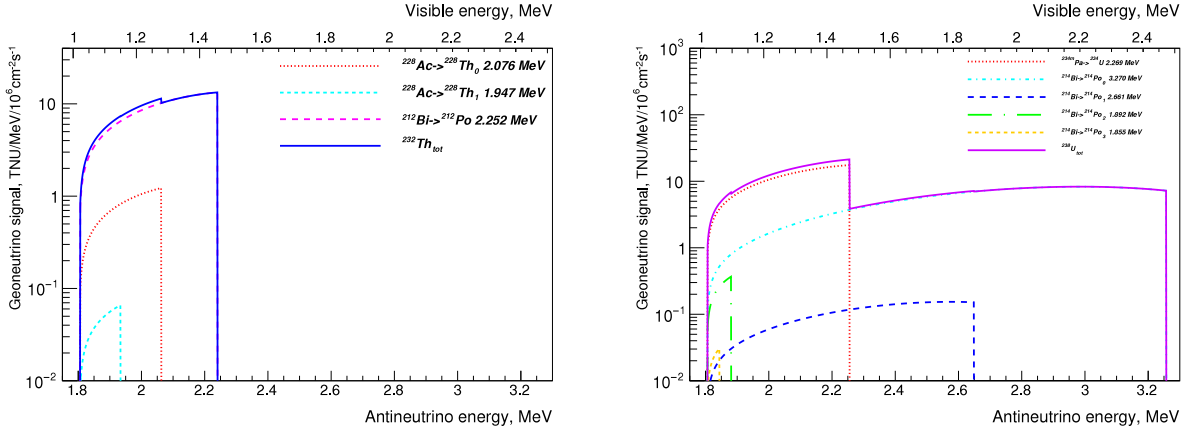
Fig. 7. Expected IBD antineutrino signal from decays in the ^{232}Th (left) and ^{238}U (right) chains. Indices after the decay denote the corresponding energy level of the daughter nucleus. An incident antineutrino flux of 10^6 cm^{-2} s^{-1} is assumed in calculations.
Source: Figure adapted from [3].
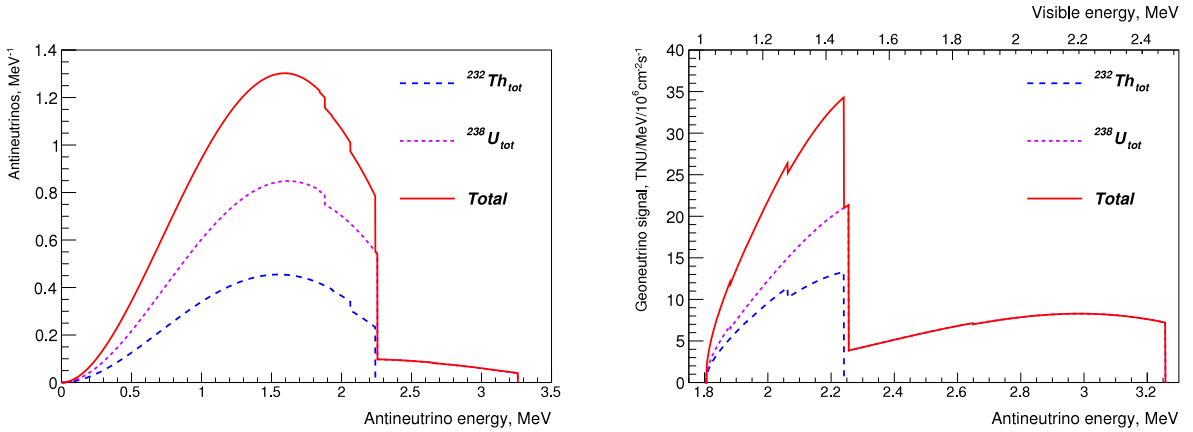
Fig. 8. left: resulting antineutrino spectra for ^{232}Th and ^{238}U chains from isotopes with end-point energy $E_0 > 1.806$ MeV and their sum for chondritic Th/U mass ratio. Total spectrum is normalized to unity. **right:** expected IBD antineutrino signal from decays in ^{232}Th and ^{238}U chains and total signal. Chondritic ratio of Th and U masses and incident antineutrino flux of 10^6 cm^{-2} s^{-1} are assumed in calculations.

4.4. Beta-decay shapes

For the allowed β-decays with massless neutrinos, the energy spectrum of electrons has the following theoretical ("universal") shape [90]

$$dN_\beta(w, w_0) = \frac{1}{N_0} F(w, Z_D) C(w) p w (w_0 - w)^2 dw, \tag{36}$$

where w and p are the full energy of the electron and its momentum ($p = \sqrt{w^2 - 1}$), respectively, w_0 is the β-decay end-point, all measured in units $m = h = c = 1$, and $F(w, Z_D)$ is the Fermi function describing the correction for screening by atomic electrons in a nuclear Coulomb field, where Z_D is the charge of the daughter nucleus, and $C(w)$ describes departures from the allowed shape. With energy-independent contributions omitted the relativistic Fermi function $F(w, Z_D)$ could be expressed as

$$F(w, Z_D) = p^{2(\gamma-1)} e^{\pi y} |\Gamma(\gamma + iy)|^2, \tag{37}$$

where Γ is the complex gamma-function, $\gamma = \sqrt{1 - (\alpha Z_D)^2}$, $y = 2\pi \alpha Z_D \frac{w}{p}$, and α is the fine structure constant.

The normalization factor N_0 provides the normalization to unity

$$\int_1^{w_0} N_\beta(w, w_0) dw = 1. \tag{38}$$

Table 5

Properties of β-decays in the ^{232}Th chain with $Q > 1.806$ MeV contributing to the geoneutrino signal in IBD detectors. The intensity of the corresponding decay with respect to one parent decay of ^{232}Th is presented in the second column. The branching ratio I is shown together with its error δI. The end-point energy Q of the corresponding decay is presented with its uncertainty δQ too. The numeric uncertainties are shown in parentheses, denoting an uncertainty in the last significant figure(s). Next column provides the type of the decay. The last two columns show the contribution f_{Th} of the corresponding branch to the full geoneutrino signal from the ^{232}Th chain, and the contribution f_{tot} to the total signal from the both U and Th chains in assumption of the allowed β-decays shape and chondritic ratio of the parent isotope masses M(Th)/M(U) = 3.9.

Decay	Bq/Bq[Th]	$I(\delta I)$	$Q(\delta Q)$ (MeV)	Type	f_{Th} (%)	f_{tot} (%)
^{228}Ac$\rightarrow$ ^{228}Th	1.000	0.07(5)	2.076(3)	Allowed ($3^+ \rightarrow 2^+$)	5.1	1.1
		0.006(5)	1.947(3)	Allowed ($3^+ \rightarrow 4^+$)	0.1	0.0
^{212}Bi$\rightarrow$^{212}Po	0.6406(6)	0.5537(11)	2.2521(17)	1st forbidden ($1^- \rightarrow 0^+$)	94.7	19.7

Table 6

Properties of β-decays in the ^{238}U chain contributing to the geoneutrino signal in IBD detectors. The notations are the same as in Table 5.

Isotope	Bq/Bq[U]	$I(\delta I)$	$Q(\delta Q)$ (MeV)	Type	f_U (%)	f_{tot} (%)
^{234}Pa$\rightarrow$^{234}U	0.9984(4)	0.9757(4)	2.269(4)	1st forbidden ($0^- \rightarrow 0^+$)	38.6	30.6
^{214}Bi$\rightarrow$^{214}Po	0.99979(10)	0.1910(17)	3.270(11)	1st forbidden ($1^- \rightarrow 0^+$)	60.6	47.9
		0.0058(18)	2.661(11)	1st forbidden ($1^- \rightarrow 2^+$)	0.7	0.5
		0.0735(5)	1.892(11)	1st forbidden ($1^- \rightarrow 2^+$)	0.1	0.1
		0.0089(3)	1.855(11)	1st forbidden ($1^- \rightarrow 0^+$)	0.0	0.0

The correction of the β-decay spectrum due to the electron screening can be easily taken into account by replacing $F(w, Z_D)$ with (Rose correction)

$$F(w - v_0, Z_D)\sqrt{\frac{(w - v_0)^2 - 1}{w^2 - 1}}\frac{w - v_0}{w}, \tag{39}$$

where $v_0 \simeq 1.13\alpha^2 Z^{4/3}$. The correction is important for the low energy part of the β-decay spectrum, i.e., relatively important for the neutrino spectra calculation. Another correction is due to the finite nuclear size, negligible for allowed transitions, and a radiative correction is due to internal bremsstrahlung (negligible for the low w_0 β-decays). Both were neglected in our calculations of the energy release in the β-decays of the isotopes from the U and Th decay chains and ^{40}K.

The β-decays can involve transitions to excited nuclear states "i" with different branching ratios b_i (with $\sum_i b_i = 1$). Transitions to excited states are typically accompanied by energy relaxation involving a single gamma or a gamma cascade and/or less abundant conversion electrons.

The β-decays are classified according to the spin change $\Delta J = |J_i - J_f|$ and the parity change $\Delta\pi = \pi_i\pi_f$, where indices i and f denote the initial and the final spin J and parity π of the nuclear states, respectively. Decays with $\Delta J^{\Delta\pi} = 0^+, 1^+$ are allowed, decays with $\Delta J^{\Delta\pi} = 0^-, 1^-, 2^+, 3^-, 4^+ \ldots$ are forbidden non-unique with the degree of forbiddenness defined by ΔJ, and decays with $\Delta J^{\Delta\pi} = 2^-, 3^+, 4^- \ldots$ are forbidden unique with the degree of forbiddenness defined by $\Delta J - 1$. From the theoretical point of view, the forbidden unique β-decays are simpler, since the rate of the decay and the shape of the spectrum are defined by only one nuclear matrix element (and thus they are "unique"). For allowed and forbidden unique transitions, Behrens and Bühring [91] demonstrated that in a first approximation, but with excellent precision, the nuclear current component can be factored out, and only the dynamical factor from the coupling with the leptons remains. However, all forbidden transitions involved in formation of the geoneutrino signal are nonunique ones. The calculation of the β-spectra for the nonunique transitions is far more complicated because the structures of the initial and final nuclear states have to be taken into account. There are good qualitative reasons to assume the allowed shape for several first forbidden nonunique β-decays if the ξ approximation is fulfilled [92], i.e., when the Coulomb energy of the β-particle emitted at the nuclear surface is much higher than the maximum energy of the transition, $2\xi = \frac{\alpha Z}{R} \gg E_o$. As noted by Mougeot [17], there are no studies evaluating the applicability of the ξ approximation or setting a limit on the ratio $2\xi/E_0$ for which it would definitely provide good results.

Hayen et al. [93] discussed the precision calculation of the allowed β-decay spectra for low to medium Z nuclei considering all the corrections up to $\sim 10^{-4}$ for energies down to 1 keV. They point out the poorly described problem of the β-spectra calculations at low energies. In particular, the screening correction, usually introduced as an energy shift v_0, does not allow calculations for energies lower than v_0, which results in discontinuities for energies typically below 10 keV. Another low-energy effect is the exchange effect corresponding to the case where a beta electron is not directly emitted into the continuum but into a bound orbital of the daughter atom, accompanied by the simultaneous emission of a bound electron. It leads to enhancement of the beta emission intensity, in particular at low energy. First discussed by Bahcall [94], it was quantitatively evaluated for several β-decaying nuclides in [95]. Its implementation for allowed transitions can be found in the BetaShape code [96]. Measurements of the β-spectrum from the forbidden transition of ^{241}Pu shows the evidence of the effect [97]. These low-energy effects tend to increase the β-spectrum, and the mirror

neutrino spectrum will be correspondingly enhanced at its high-energy part. The effect in the observed signal will be amplified because of the fast increase of the IBD cross section with energy, and the enhancement of the β-spectrum by 0.1% of the total one at low energies will result in the 0.6% increase of the U signal and the 0.9% increase of the Th signal.

The shapes of the β-decay spectra have only little been studied experimentally since the late 1970s. These spectra were thought to be known accurately enough. Theoretical studies stopped in the 1980s. However, at present, it became obvious that there are not enough data available, in particular for high forbidding orders and at low energy [98]. Precise knowledge of the shape of energy spectra and their uncertainties, especially in the low-energy region of the β-spectrum, is needed for accurate geoneutrino flux estimations. The same applies to the feeding probabilities in complex decay schemes.

An attempt to measure the shape of the ^{214}Bi $(\beta + \gamma)$ decay was reported in [99]. The experimental spectrum obtained with the CTF detector [100,101] was fitted with a model function. First, the feeding probability p_0 of the ground state was defined from the fit assuming the universal β-decay shape. The feeding probability p_1 of the first excited state in this fit was fixed at the central value from [102]. Other transitions result in β-decays with energies below the geoneutrino detection threshold, and do not contribute to the geoneutrino signal. Their probabilities were fixed at the central values from [102] too. The p_0 was found to be 0.177 ± 0.004, consistent with the indirect estimate of the table of isotopes.[16]

At the next step of the analysis the shape of the β-spectrum with end-point $E_0 = 3.27$ MeV corresponding to the transition to the ground state was allowed to vary applying an adjustable form-factor parameter. The values of p_0 and p_1 in this fit were constrained at the values from [102]. It was found that the effect of uncertainties of the β-decay shape on the geoneutrino signal is mostly negligible. The conclusion reflects the fact that the effect of shape variations and that of the values of p_0 and p_1 on the signal are anticorrelated in the fit of the ^{214}Bi spectrum with free shape parameter and free p_0 and p_1. Therefore, if the spectrum is deformed in a way that there are more (fewer) low-energy electrons, the corresponding best-fit value for p_0 is lower (higher). If p_0 ranges from 0.13 to 0.20, the signal would change only by about $\pm 2\%$, i.e., the resulting signal weakly depends on the spectral shape [99]. Larger statistics and reduction of systematics should allow the testing of possible deviations of the neutrino spectrum from the one predicted using the universal shape [99].

4.5. Uncertainties of the predicted geoneutrino signal

The principal factors responsible for uncertainty of the expected geoneutrino signal are related to masses and spatial distribution of radioactive isotopes in the Earth, in contrast to the radiogenic heat that is related only to the total masses of the HPEs. As noted above, the measurement of the geoneutrino signal from the mantle is a clue to distinguishing between the existing models. The mantle contribution can be obtained by subtracting the crust contribution from the total measured signal, and, thus, the minimal possible mantle signal uncertainty is defined by absolute uncertainty of the crust contribution. Since, the accurate prediction of the crustal signal is of primary importance for extraction of the mantle signal. The total uncertainty of the predicted geoneutrino signal from the crust includes geological, geophysical and geochemical uncertainties, and, to the less extent the uncertainties related to the antineutrino physics. The chemical properties of the Earth are less understood compared to its physical structure. The typical uncertainties of the U and Th content in the BSE model are 15%–20% or worse [18]. The uncertainties of the distribution of HPEs, or geophysical uncertainties, contributes 5–10% to the total uncertainty of the crustal signal prediction [33]. Other uncertainties of the expected geoneutrino signal are less important (including uncertainty in the oscillation parameters, uncertainties of the β-decay shapes, uncertainties in the branching ratios, etc.). These antineutrino physics uncertainties constitute $\sim 3\%$, still beyond the sensitivity of the experiments.

It should be noted that since the U, Th, and K, the main contributors to the geoneutrino signal, are all lithophile elements with similar geochemical properties, their content in different Earth reservoirs is positively correlated. In contrast, the total mass constraint of the Bulk Silicate Earth model anti-correlates these element abundances in complementary reservoirs. The problem of the uncertainties and correlations in geoneutrino flux calculation was investigated in [103]. The authors constructed a "geoneutrino source model" (GNSM) for the U, Th, and K abundances in the main Earth reservoirs and then used it to predict geoneutrino signal. They showed the possibility for the future data to constrain the error matrix of the model itself. It should be noted, however, that present experimental uncertainties (connected mainly with low statistics) appear to be significantly larger than those in the GNSM.

The bias in the estimation of the geoneutrino signal related to the specific properties of the probability distributions used for the description of the element abundances are discussed by Takeuchi et al. [104]. The log-normal distribution is widely used for rock composition models [24,33,105], as was suggested by Ahrens [106], based on the observation that igneous rocks commonly show skewed compositional distributions. The use of log-normal probability density functions (PDFs) can lead to bias in mean values, if the maximum likelihood method is used to fit the sample distributions. The geometric mean is unbiased in log-normal models, but it is generally different from the arithmetic mean. The gamma distribution was found to be a better choice than the normal or log-normal distributions for the purpose of unbiased flux calculation [104].

---

[16] The consistency of the experimental result in [99] was checked against the value $p_0 = 0.182 \pm 0.006$ from [102]. The updated value of p_0 is 0.1910 ± 0.0017 [15], which differs by 3.2σ from the measured in CTF. Therefore, the result of [99] could indicate the presence of deviations from the allowed universal shape, and more data are needed to draw the statistically significant conclusions.

Another source of bias could arise from the use of median values for description of rock compositions. For skewed distributions, the median differs from the mean, and the result will have an unpredictable mean or median if median values are used in estimations or in mass-balance calculations. Also, after rejecting "non-typical" samples in distribution tails, the mean of the filtered samples depends on the filter cut-off and hence the resulting mean becomes arbitrary. All these systematic uncertainties can be avoided by using the proper distribution shape.

Based on the discussed points, a method of 3D crustal modelling was developed by Takeuchi et al. [104] with uncertainty estimation that is truly probabilistic and reproducible, as opposed to "uncertainties by comparison" or "subjective/arbitrary estimation".

5. Sources of background in IBD experiments

Experimental errors in geoneutrino experiments are associated mainly with low statistics and with the presence of backgrounds, as it is very difficult to ensure a background-free environment for counting such rare events. Principal contributions to the background come either from antineutrino sources other than geoneutrinos (reactor antineutrinos) or from events mimicking antineutrino interactions. The latter can be produced by cosmic muons (cosmogenic background) or by intrinsic residual radioactive contamination of LS (internal background). Other natural antineutrino sources such as a diffuse flux of neutrinos from past supernovae (supernova relic neutrinos with, the flux is ~ 10 cm^{-2} s^{-1} [107]) and atmospheric neutrinos (~ 1 cm^{-2} s^{-1} [108]) are negligible compared to the geoneutrino flux ($\sim 10^6$ cm^{-2} s^{-1}) and do not contribute to the background.

5.1. Antineutrino candidates selection

Selection criteria for the pairs of correlated events (antineutrino candidate events) are built using the reconstructed distance ΔR between two events, the time difference between the events ΔT, the cut on events energy, and the cuts on the interaction types in the case where the detector provides a possibility of distinguishing events caused by β's or γ's from those caused by heavier particles, alphas and/or protons. The set of events selected using the cuts can still have an admixture of "false" events due to the random coincidence of single background events passing all the selection criteria, and/or due to the (β, n) decays of the spallation products, events caused by fast neutrons, etc. These backgrounds will be considered in more detail in this section.

The antineutrino candidate selections in general include:

1. A cut on the prompt event energy, which should accept events with energies from the kinematic threshold of the IBD to the highest energy expected for the considered process. Energy resolution of the detector should be taken into account.
2. A cut on the delayed event energy should be tuned to accept the peak of 2.2 MeV γ from the neutron capture. The cut should take into account the energy resolution of the detector and the possible partial escape of γ's to the outer part of the detector.
3. A cut on the time difference between the prompt and the delayed events, ΔT, usually ranges from the minimum possible time defined by the detector and its electronics properties to the upper limit defined by optimizing the ratio of efficiencies for accepting true events and the leakage of the random background.
4. A cut on the relative distance between the prompt and the delayed events, ΔR. The upper limit for ΔR is to be chosen by optimizing the signal-to-background ratio.

The efficiency of the basic cuts depends on the detector's characteristics (energy resolution, vertex reconstruction precision) and internal background in the chosen FV and can depend on the energy of the prompt event. The efficiency is lower at the sensitive volume borders due to the possible escape of the delayed γ from the detector. In practice, it reaches 70%–85% in large volume liquid scintillation detectors.

The set of the basic cuts for selecting the correlated events can be complemented with α/β selection cuts, since both prompt and delayed events are caused by light ionizing particles (electron-like events). A cut on the FV was applied in both the Borexino and KamLAND analyses to remove excessive external background. The false events caused by passing muons are removed by excluding the time range after the identified muon; the duration of the excluded time is defined by the type of expected background. For neutron-related backgrounds it is enough to exclude ~ 2 ms, and exclusion of long-lived (β+n) isotopes needs veto times of ~ 2 s.

The physical background from nuclear reactors is irreducible and can be separated from geoneutrinos by applying a spectral cut. The spectral cut should also allow for the shape of the residual backgrounds, given that they are still present after all the cuts applied.

5.2. Reactor antineutrinos

Until now the geoneutrino flux measurement was a side-product of projects having other main goals, namely solar neutrino fluxes measurement in the case of Borexino, or oscillations of reactor antineutrinos in the case of KamLAND. The reduction of background from reactors was not an option in the projects. The search for the neutrino mass hierarchy with

the next generation of antineutrino detectors, e.g., 20 kt LS JUNO experiment [109], requires a location even closer to the reactors, which would provide the maximal manifestation of the effect searched for, but at the same time making more difficult the extraction of the geoneutrino signal because of the stronger reactor antineutrino background. On the other hand, these detectors will provide higher statistics of events, in principle allowing for the use of statistical separation of geoneutrinos and reactor antineutrinos on the basis of directionality. The reactor antineutrino flux depends on the power of the nuclear reactors and on the distance between the reactors and the detector. Keeping track of power history of near reactors helps in statistical extraction of the expected signal.

Nuclear reactors generate heat by controlled fission of uranium and plutonium isotopes. The main components of the nuclear fuel are ^{235}U, ^{238}U, ^{239}Pu, and ^{241}Pu providing more than 99.9% of the total power, and thus only these actinides are considered. Their relative contributions to the total thermal power of the plant depend on the reactor type and on the burn-up stage of the individual core. Antineutrinos are emitted in β^- decays of fission products. The energy spectrum of reactor antineutrinos extends up to ∼10 MeV, covering the full range of the geoneutrino spectrum. The total antineutrino spectrum from the reactor for a single fission event can be expressed as a sum of individual contributions

$$\Phi_R(E) = \sum_{I=1}^{4} f_I \phi_I(E), \tag{40}$$

where the fission fraction f_I is the contribution of the isotope I, $\sum f_I = 1$, and $\phi_I(E)$ is its antineutrino energy spectrum. The thermal power of the reactor W_{th} is expressed through the number of fission rates R and the thermal energy release Q_I per one fission of the isotope I or through the thermal power $P_I = R \cdot f_I \cdot Q_I$ generated by the isotope I

$$W_{th} = R \sum_{I=1}^{4} f_I Q_I = \sum_{I=1}^{4} P_I. \tag{41}$$

The corresponding effective energies Q_I are determined from the energy released in fission with account taken of the energy loss due to the antineutrino emission and extra energy produced by neutron captures on the reactor materials. The values of Q_I were calculated by Kopeikin et al. [110].

Similarly to the fission fractions, the power fractions p_i can be defined as

$$p_I = \frac{P_I}{W_{th}} = \frac{f_I Q_I}{\sum_{I=1}^{4} f_I Q_I}. \tag{42}$$

The power fraction p_I is the fraction of the total thermal power produced by the fission of the isotope I. If the power fractions p_I are known, Eqs. (40) and (41) can be used to obtain the antineutrino spectra from the reactor's thermal power using isotopic antineutrino spectra $\phi_I(E)$

$$S(E_\nu) = W_{th} \cdot \sum_{I=1}^{4} \frac{p_I}{Q_I} \phi_I(E_\nu), \tag{43}$$

The antineutrino spectrum $\phi_I(E)$ of the isotope I is a weighted sum of antineutrino spectra from all fission fragments for the corresponding isotope. Typically, the number of involved isotopes is over 800. In practice, the antineutrino spectrum of a given fission fragment is not measured, but obtained from the corresponding β-spectrum. The latter in many cases is not known with sufficient precision, or its computation is complicated by many possible branches. Consequently, a summation of the antineutrino spectra will result in a limited accuracy of the final antineutrino spectrum [111,112], but in many cases it is the only available option.

Another method is based on the reconstruction of the reactor antineutrino spectrum from the measured integral *beta*-spectrum of all fission fragments [113–117]. In order to convert a measured electron spectrum into the antineutrino one, the total spectrum is fitted with a set of allowed β-spectra over the preliminary defined set of virtual end-point energies that can also be the fit parameters. The antineutrino spectrum is then obtained by replacing the electron energy E_e in each branch by its "mirror" reflection $E_0 - E_{\bar{\nu}}$. The procedure guarantees good reproduction of the experimental electron spectrum, but the converted spectrum depends on the uncertainties related to effects of nuclear structure [117]. In particular, Hayes et al. [118] pointed out that uncertainties could arise due to the forbidden decays and could make up to 30% of all the spectra. Correspondingly, a highly debated "reactor anomaly", consisting in a 6% deficit of antineutrinos detected in short-baseline reactor antineutrino experiments compared to the prediction based on the converted aggregate β-spectrum and presumably constituting the 3σ effect [119], can be a result of underestimation of the theoretical errors.

In the last several years, a significant deviation from the prediction in the 4–6 MeV energy range is observed by a number of reactor antineutrino experiments, see [120–124] and review [125]. More specifically, an excess of events observed in the measured spectrum at these energies has 4.4σ local significance [121]. With respect to the geoneutrino energies, the feature appears at higher energies and should not significantly influence the geoneutrino analysis. At present, the physical reasons for the neutrino spectral bump are unclear, but the spectral distortion can be accounted for in the analysis by using the experimental measurements.

In geoneutrino studies the antineutrino spectra are predicted using available information on the reactors' thermal power, their geographical position, mode of operation, types, etc. The non-oscillating antineutrino spectra are taken
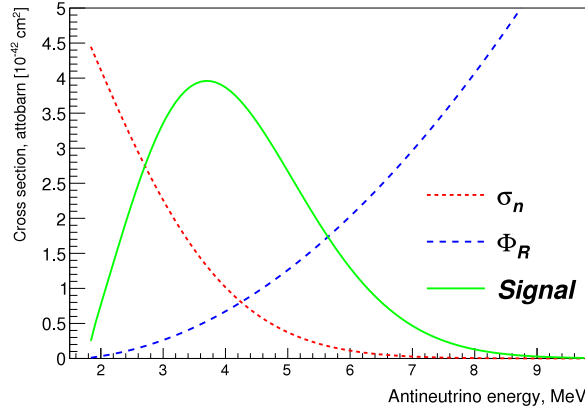
Fig. 9. IBD cross section (increasing function, blue), the non-oscillating reactor antineutrino flux (decreasing distribution, red), and the resulting reactor signal (bell-like shape, green). The vertical scale shows the IBD cross section absolute values measured in attobarn (10^{-42} cm^2), while other two shapes are arbitrary normalized.

from parameterizations, with the most recent one provided in [112]. The spectral shapes are very similar to the older parameterization given in [126] with a 3.5% higher total flux. Phenomenological parameterization of fission antineutrino spectra for a given isotope has a polynomial form

$$\phi_I(E_\nu) = \exp(\sum_{p=1}^{6} \alpha_{p,I} E_\nu^{p-1}). \tag{44}$$

The coefficients α_p for each of the involved isotopes I are provided in [112]. The product of the fast-decreasing reactor spectrum and the steeply increasing IBD cross section gives a bell-like shaped spectrum of the detected signal with a maximum around 4 MeV, schematically shown in Fig. 9.

A reactor operation schedule is required for estimating its contribution to the detected antineutrino spectrum in a given time interval. The load factor (LF) is used as a measure of the reactor time profile. It is defined as the ratio between the net electrical energy produced during the reference period and the net electrical energy that would be produced if the reactor operated in the steady mode. The load factor data are published by the International Atomic Energy Agency (IAEA) [127], providing the data on a monthly timescale and as an annual average. It is assumed in the calculation that the published values of electrical LFs are equal to the corresponding thermal LFs.

Summarizing, the signal from the reactor antineutrino can be evaluated as [128]

$$\frac{dn_R(E_\nu)}{dE_\nu} = \epsilon(E_\nu) \cdot N_p \cdot T \cdot \sum_{R=1}^{N_{Reactors}} \frac{W_{th}^R}{4\pi L_R^2} LF_R \cdot \sum_{I=1}^{4} \frac{p_I}{Q_I} \phi_I(E_\nu) P_{ee}(E_\nu, L_R) \sigma_n(E_\nu), \tag{45}$$

where the index R runs over all world reactors $N_{reactors}$ and I runs over 4 isotopes, E_ν is the antineutrino energy, $\epsilon(E_\nu)$ is the detector efficiency, N_p is the number of target protons, T is the data taking time, W_{th}^R is the thermal power of the Rth reactor, LF_R is the load factor of the Rth reactor, $\phi_I(E_\nu)$ is the antineutrino spectrum of the isotope I, $P_{ee}(E_\nu, L_R)$ is the electron antineutrino survival probability at the distance L_R to the reactor. In general the signal also depends on the neutrino oscillations parameters, and in the 3-flavour scenario of oscillations the dependence is expressed by formula (12) if matter effects are neglected. The effective energies Q_I and the thermal power fractions p_I are defined above, and $\sigma_n(E_\nu)$ is the IBD reaction cross section.

The information on LFs and thermal powers is provided on the monthly basis, and, hence, for the practical usage the further month-by-month summation of the spectra provided by formula (45) is needed, with the values of T, W_{th}^R and LF_R evaluated for each month.

There are about 450 nuclear power plants over the world, concentrated mainly in Europe, North America, Japan, and Korea. The oscillation length for antineutrinos with energies of a few MeV is at a level of 100 km, and the expected signal spectra demonstrate a characteristic oscillation pattern. The geographic location of the reactors is important for the calculations. An example of the expected reactor spectrum compared to the geoneutrino signal for two extreme cases for Reactor/Geo antineutrino signals ratio is shown in Fig. 10 for the Borexino (with a moderate Reactor/Geo signals ratio) and JUNO (with the highest value of the Reactor/Geo signals ratio) detectors; another example is presented in Fig. 24, where the reactor spectrum for the closest reactor in the Sudbury laboratory shows pronounced oscillation features.

The total expected reactor antineutrino signal, the expected reactor antineutrino signal in the geoneutrino energy window ($E_{\overline{\nu_e}} < 3.27$ MeV), the predicted geoneutrino signal, and the reactor-to-geoneutrino ratio for the relevant energy range are presented in Table 4. The data on the predicted reactor signals are compiled using the estimates from [76] for
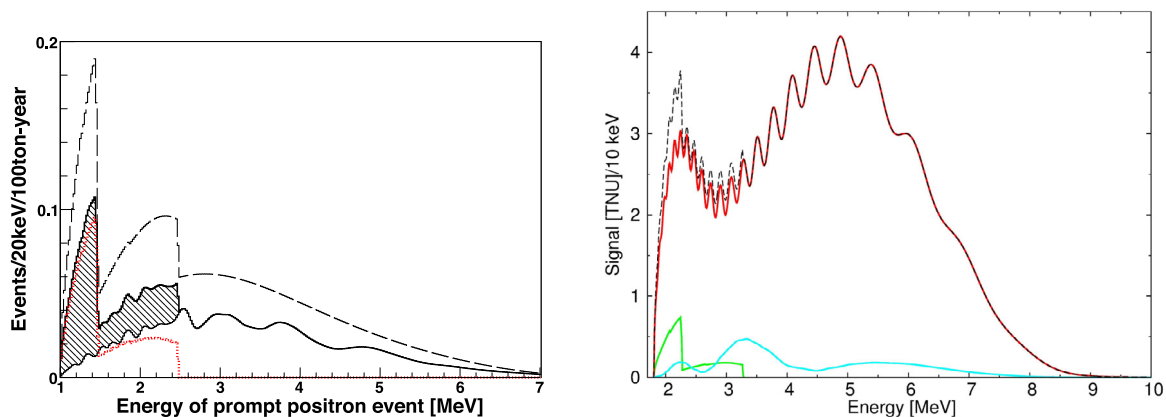
Fig. 10. left: total antineutrino spectra expected at Borexino's location, no energy resolution is applied. Non-oscillating (or total antineutrino flux) and oscillating (electron antineutrino) spectra are shown with dashed and solid lines, respectively. The geoneutrino contribution is shown by the red line. Its contribution to the oscillated spectrum corresponds to the shaded area (Fig. from [129]). **right:** antineutrino energy spectra expected at JUNO's location. The geoneutrino energy spectrum is visible at the beginning of the energy scale (green). The reactor antineutrino spectrum is shown before (the lower curve expanding over all energy scale, cyan) and after adding the contribution of the Yangjiang and Taishan nuclear power plants (the upper solid line, red), reactor ON scenario. The reactor antineutrino spectra are computed assuming normal neutrino mass hierarchy and taking into account neutrino oscillation. The total spectrum (black dashed lines) is obtained assuming the reactors ON scenario (Figure from [130]).

JUNO, that include 2 future reactors, contributing more than 90% to the total, from [77] for Jinping site, and from [75] for the rest of the locations. The geoneutrino signals were calculated by Huang et al. in [24] using their Reference EARTH Model. The ratio between the predicted reactor signal in the Low Energy Region (LER) and the expected geoneutrino signal can be considered as a factor characterizing the sensitivity of the detector placed at the corresponding location with respect to the geoneutrino fluxes.

In addition to short-lived fission products discussed above, the exhausted fuel contains isotopes with decay time of the order of 1 yr that can contribute to the reactor antineutrino signal. The pressurized light water power reactor (PWR) operates for 11 months, followed by shutdown of 1 month to replace 1/3 of the spent nuclear fuel (SNF), which is generally kept for several years in a water spent fuel pool not far from the reactor, forming an additional small but potentially non-negligible source of antineutrinos. The KamLAND collaboration estimated an additional contribution of 2.4% to the reactor antineutrino signal from the spent fuel [13]. For the Chooz experiment, an increase of 1.0–1.5% in the LER of the reactor antineutrino spectrum was predicted by Kopeikin et al. [131]. Similarly, it was found that the spent nuclear fuel spectrum influenced the softer part of the Daya Bay experiment antineutrino spectrum, with the maximum contribution from the SNF of about 3.0% [132].

Since the background from reactors is caused by antineutrinos indistinguishable from the geoneutrinos, it can be separated from the geoneutrino spectrum only by applying a spectral fit. The model spectra should account for the shape distortions due to antineutrino oscillations. In practice, both the reactor antineutrino spectrum and the number of events are calculated, but the normalization is left as a free parameter in the fit over the entire energy scale.

The antineutrino flux from the reactors is affected by planned upgrades in which different reactor cores are turned off, which results in expected variations in the total flux. The known time evolution of the reactors power provides additional information for separating this background. This possibility was exploited by the KamLAND collaboration before the almost total shutdown of the Japanese reactors in 2011.

5.3. Cosmogenic backgrounds

Muons produced in primary cosmic ray interactions in the atmosphere penetrate deep underground. Though the cosmic muon flux is reduced in the underground labs by orders of magnitude, it is still high enough to induce significant background. The site depth is the main factor influencing the cosmic muon flux, which decreases exponentially with depth. Among existing underground sites the best shielded against cosmic muons is SNO laboratory (Canada) placed in a 2 km deep mine and providing shielding equivalent to 6010 m of water. The Baksan laboratory in the Caucasus mountains (Russia) provides 4800 m.w.e. shielding. The LNGS laboratory in Italy, where the Borexino detector is placed, provides 3400 m.w.e. shielding; the KamLAND site is less protected (2700 m.w.e.), and the future JUNO site will be even less protected (2000 m.w.e.) against cosmic muons. See Table 4 for more details.

Hagner et al. [133] studied production of radioactive isotopes by the muon spallation reaction in an organic LS using the Super Proton Synchrotron muon beam at CERN. The production yields were studied with 100 and 190 GeV incident muons and extrapolated at other energies assuming a power-law dependence on the incident muon energy. Direct measurements of the production yield of cosmogenic isotopes were performed with large underground detectors: the

Mont Blanc liquid scintillation detector (LSD) [134], the large-volume detector (LVD) [135], the Borexino [79] in LNGS, and the KamLAND [136]. The direct measurements were compared with calculations on the base of MUSIC [137], FLUKA [138], and GEANT4 [139] programs. Some of these isotopes are long-lived and a false candidate event could be produced by a random coincidence of two decay, following the muon. But the most dangerous cosmogenic background from the point of view of its similarity to the IBD events is associated with neutron-rich isotopes produced by spallation with a β-decay branch followed by the emission of a neutron and thus perfectly matching the antineutrino-induced signal. These are long-lived ^{8}He ($T_{1/2} = 119.1$ ms, with $\beta + n$ branching ratio of 16% and Q = 10.65 MeV [15]) and ^{9}Li ($T_{1/2} = 178.3$ ms, with $\beta + n$ branching ratio of 50.8% and Q = 13.6 MeV [15]). The end-points of both β-spectra in $\beta + n$ branches are big enough to cover completely both the geoneutrino and the reactor spectra. Because $\beta + n$ decays are indistinguishable from antineutrino events, the best way to suppress the corresponding background is complete or partial exclusion of events occurring after an identified muon passing through the detector. In the first case all events in the detector volume are excluded from the analysis in the fixed time window after the passing muon. The veto time should be optimized to provide the best balance between the cosmogenic background reduction efficiency and the loss of the live time. The typical veto time is 2 s. In the case of a partial veto, only the cylindrical volume around the muon track, where spallation is possible, is excluded from the analysis for the fixed time. This helps to gain the live time, but the method is more complicated as it requires reconstruction of the muon track and introduces additional uncertainties to the exposure calculations.

Thus, the IBD detector must be equipped with an efficient muon detector and/or muon tracker. The criteria for the choice of the muon veto depend on the site depth.

Another background related to cosmic muons is caused by fast neutrons (single or multiple) produced outside the detector, i.e., by muons not identified by the muon detector. Fast neutrons have a long free path, and hence can reach the active volume of the detector entering from outside. The fast neutron elastically scattered off the proton can produce a high energy prompt event, and then thermalize and be captured onto a proton, producing an antineutrino-like false event. The amount of these events depends on the site depth and detector geometry, and is typically comparable to the residual background from the isotopes with the $\beta + n$-decay mode. The prompt signal due to the proton scattered off the neutron should, in principle, be distinguishable from the signal induced by a positron in LS due to different time profiles of the scintillation flash. A heavy particle produces flashes with a more pronounced "slow" component, i.e., its time distribution has longer tails compared to ones in time distribution of scintillations caused by electrons and gammas, allowing partial discrimination of this type of background.

5.4. Intrinsic backgrounds and external γ background

Because of the presence of residual radioactivity in the LS some false events can be selected after applying the cuts, forming the so-called random coincidences background. The possible low-level contamination of the LS with radioactive impurities can be due to the cosmogenic ^{14}C, naturally present in the organic LS, or due to the radioactive noble gases transferred to the LS when in the contact with air (normally containing cosmogenic ^{39}Ar, technogenic ^{85}Kr from nuclear power plants exhaust, and ^{222}Rn produced in the ^{238}U decay chain), or it could be residual intrinsic contamination with ^{40}K or isotopes from the decay chains of ^{232}Th and ^{238}U. Some of the daughter isotopes can be present not in secular equilibrium with progenitors due to different efficiencies of purification and other processes. In order to provide an acceptably low level of random coincidences count, the LS of the detectors should be purified and kept in conditions that prevents its contamination. The choice of the proper LS purification strategies can reduce these contaminations to very low levels, as was demonstrated by the Borexino collaboration.

The random coincidence spectrum and its counting rate can be easily reproduced on the basis of single (uncorrelated) event spectra by picking pairs of events in an off-time coincidence window (one random event and another one from the time window far away from the one used to search for the candidates) and applying the same selection criteria as used to select candidate events. The overall rate of random coincidences depends quadratically on the single events count, i.e., on the residual radioactivity. The prompt signal energy spectrum coincides with a single events spectrum if the events are uniformly distributed over the detector volume, otherwise the non-uniform distribution of sources can result in the deformation of the spectrum shape.

Another source of background tightly linked with internal LS contamination is the (α, n) reaction on ^{13}C, which is naturally present in organic scintillators with isotopic abundance of 1.3%. Monoenergetic α-particles with the 5.3 MeV kinetic energy are produced in decays of ^{210}Po from the ^{238}U decay chain [140]. The ^{210}Po have 138.4 days life-time. In both the Borexino and the KamLAND detectors the activity of ^{210}Po was found to be higher than those expected in the case of secular equilibrium with ^{238}U or its most probable source of ^{210}Pb deposited from the decays of ^{222}Rn. More details can be found in sections dedicated to the Borexino and KamLAND experiments.

An antineutrino candidate event can be mimicked by the ^{214}Bi decay from the ^{222}Rn decay chain followed by a rare branch in the ^{214}Po α-decay. The life-time of the ^{214}Po isotope is close to the neutron capture time in the LS. If the energy conditions for the prompt and delayed signals are satisfied, then this delayed coincidence would pass the simple selections cuts. The energy of α is 7.69 MeV in 99.99% of decays, and in the remaining 10^{-4} cases the energy is released through 6.9 MeV α accompanied by a 0.8 MeV γ. The visible energy in the latter case is much higher, since light yield of α-particles is highly suppressed compared to the light yield of light ionizing particles and can fall into the energy range chosen for the delayed event selection. The α/β discrimination technique can be applied to distinguish pure 2.2 MeV γ from the $\alpha + \gamma$ decay in the considered case.

The LS is contained in a transparent vessel. Despite very thin walls of the vessel, it is still a relatively strong source of γ's because of many orders of magnitude higher content of radioactive impurities compared to the intrinsic contamination of the LS. Also, the energetic γ's from the decay of radioactive isotopes in other construction materials can penetrate the passive shielding (buffer). To reduce these backgrounds, the inner part of the whole volume, or the FV, can be used in the analysis, and the outer part of the LS volume will serve as an active veto against the external backgrounds. The software-defined dimensions of the FV depend on the trade-off between the acceptable count of random coincidences and the mass of the antineutrino target.

Background from the radioactive contamination of LS can be further reduced by applying the e^+/e^- discrimination method [141], successfully used by the Borexino collaboration to reduce background from β^+-decay of cosmogenic ^{11}C [142]. The idea of the method is based on the difference in the photon emission time distribution. In 50% of the cases the decay of the positron occurs through a bound orthopositronium state, which delays the positron decay in the LS by few nanoseconds. This turns out to be enough to be used in statistical positron tagging. In a simple case of other backgrounds being pure electronic (β-decays) the amount of background events should correspond to the difference between the amount of electron-like and positron-like events, giving additional information for background suppression.

6. Current experiments and their results

The first indication of a non-zero geoneutrino signal was reported by KamLAND in 2005 [13], and the 90% confidence interval for the total number of detected geoneutrinos of 4.5 to 54.2 was found with the Th/U mass ratio fixed in the fit at the chondritic value of 3.9. In April 2010, the first high significance confirmation of the geoneutrino signal detection came from the Borexino [14]. The collaboration reported the presence of a non-zero geoneutrino signal in the acquired antineutrino data set at a 99.997% confidence level. Both experiments provided several updates of their results with the most recent ones released in 2015 by Borexino [143] and in 2016 by KamLAND [144], the latter still has a preliminary status.

Both experiments exploit large volume liquid scintillation detectors with 300 and 1000 tonnes of the target mass respectively, placed deep underground to protect the setup against cosmic muons. The antineutrino detection in both detectors is performed via the IBD of the proton.

6.1. Borexino experiment

Borexino is a large volume, unsegmented organic liquid scintillation detector located underground at the Laboratori Nazionali del Gran Sasso, Italy. The complete up-to-date technical description of the Borexino detector is reported in [145,146]. Primarily designed for high precision real-time measurement of the flux of monoenergetic (862 keV) ^{7}Be solar neutrino via $\nu - e$ elastic scattering interactions in the scintillator, Borexino is also an extremely sensitive antineutrino detector with practically zero non-reactor backgrounds. Because both β and γ interactions are essentially indistinguishable from the sought-after solar neutrino induced events, the measurement was made possible by the deep purification of the LS from radioactive contaminants, well below the 10^{-16} g of U and Th per g of the LS [147]. The feasibility of reaching the level of radiopurity required by Borexino was first proven in the tests performed in 1996 with Borexino's counting test facility (CTF), a first detector sensitive to radioactive contaminations at subtrace levels below 10^{-16} g/g in U and Th, out of the reach of other techniques [100,101].

The Borexino detector is schematically depicted in Fig. 11. The central spherical core of 278 t design value contains organic LS solution, composed of pseudocumene (1,2,4-trimethylbenzene $C_6H_3(CH_3)_3$) doped with 1.5 g/l (0.17% by weight) PPO fluor (2,5-diphenyloxazole, $C_{15}H_{11}NO$). The LS is contained within an 8.5-m-diameter Inner Vessel (IV), made of a thin (125 μm) transparent nylon carefully selected and handled in order to achieve maximum radiopurity [148]. The Borexino is equipped with 2212 large area photocathode PMTs. The inward looking 8″ PMTs are uniformly distributed over the inner surface of 13.7-m-diameter stainless steel sphere (SSS). All but 384 PMTs are equipped with light concentrators that are designed to reject photons not coming from the active scintillator volume, thus reducing the background caused by the radioactive decays in the buffer liquid or by penetrating γ's from the PMTs. The 384 PMTs without concentrators are used to study this background and help identify muons that cross the buffer but not the IV.

The space between the IV and the SSS is filled with 1000 t of quenched pseudocumene (PC) buffer fluid, composed of PC with an addition of 5 g/l of dimethylphthalate (DMP, $C_6H_4(COOCH_3)_2$). A small amount of DMP quenches the undesired scintillation yield of the buffer fluid by a factor of 20. The amount of light produced by external γ-rays originating from the PMTs and surrounding materials is quenched below the trigger level, hence avoiding the processing of these events and preventing the trigger electronics overloading.

The buffer is further subdivided into two regions by a second transparent nylon vessel 11.5 m in diameter, or outer vessel (OV), made of the same material as IV, and preventing ^{222}Rn emanated by the external materials (steel, glass, PMT materials) from being transported close to the IV with convective fluxes. Since the PC/PPO solution is slightly lighter (about 0.4%) than the PC/DMP solution, the IV is anchored to the bottom ("south pole" of the SSS) with a set of nylon strings. The buffer between the IV and the SSS provides shielding against external backgrounds. The choice of PC as a buffer material is based on the fact that it matches both the density and the refractive index of the scintillator, thus reducing the buoyancy force for the nylon vessel and avoiding optical mismatch that otherwise would complicate the vertex reconstruction of events.
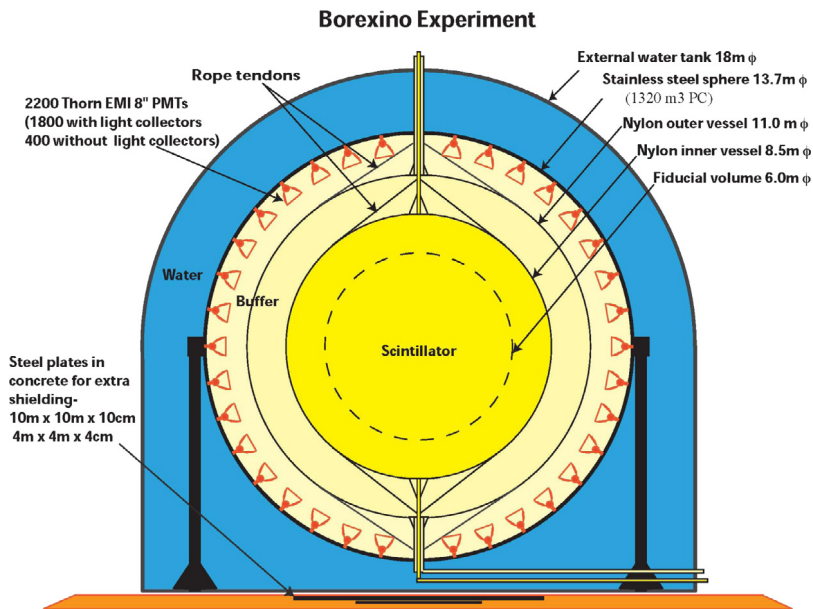
Borexino Experiment

Fig. 11. Sketch of the Borexino detector (courtesy of Borexino collaboration).

The SSS is placed inside a large dome-like water tank (WT) filled with ultra-pure water that provides shielding from high energy γ rays and neutrons emerging from the surrounding rock. The tank has a cylindrical base with a diameter of 18 m and a hemispherical top with a maximum height of 16.9 m. Since the densities of the buffer and LS are ~12% below the water density, the SSS is anchored to the ground by 20 steel legs to compensate for the mechanical stress caused by ~150 t of buoyancy force. The muon flux, although reduced by a factor of 10^6 by the 3800 m.w.e. depth of the Gran Sasso Laboratory, is of the order of 1 m^{-2} h^{-1}, corresponding to about 4300 muons per day crossing the detector. This flux causes the background well above the Borexino requirements, and muons identification system is needed with efficiency providing a strong reduction factor of about 10^4. Therefore, the WT is designed as a Čerenkov muon detector and muon tracker (outer detector, OD) with additional 208 PMTs, The OD is particularly important for detecting muons skimming the central detector and inducing signals in the energy region of interest for neutrino physics. In order to maximize the light collection efficiency, the SSS and the interior of the WT surface are covered with a layer of Tyvek, a white paper-like material made of polyethylene fibres.

Pure PC is a scintillator itself, but an addition of a small quantity of PPO greatly improves the time response and shifts the emission wavelength spectrum to higher values, thus better matching the PMT photocathode quantum efficiency maximum. The PC/PPO solution adopted as a liquid scintillator satisfies specific requirements: high scintillation yield (~ 10^4 photons/MeV), high light transparency (the mean free path is typically 8 m) and fast decay time (~3 ns), all essential for good energy resolution, precise spatial reconstruction, and good discrimination between β-like events and events due to α-particles. Furthermore, several conventional petrochemical techniques are available to purify hundreds of tonne of fluids needed by Borexino.

The LS based on PC provides an opportunity for distinguishing heavy ionizing particles from the light ones. The method is based on the difference in the time profiles of the corresponding signals. Lighter ionizing particles produce faster signals, distinct from the ones produced by the heavier particles with longer tails in the time distribution of the light emission. Several techniques were studied in Borexino for the α/β discrimination, including the optimal Gatti filter [149,150]. The Gatti filter weights bin per bin the time profile of a signal using two reference distributions. Constructed in this way Gatti parameter $g_{\alpha\beta}$ gives a numeric estimate of the similarity of the time profile of the signal to one of the two reference profiles. The α/β discrimination is used for the antineutrino candidate selection to distinguish the false signal due to the ^{214}Po($\alpha + \gamma$) decay with positive $g_{\alpha\beta}$ values from the true one induced by 2.2 MeV γ from the neutron capture on the proton (negative $g_{\alpha\beta}$).

The position of each scintillation event in Borexino is reconstructed off-line with a spatial reconstruction algorithm using the timing pattern of hit PMTs. The code is tuned using the data from several calibration campaigns with radioactive sources inserted in different positions inside the detector [151]. A maximum deviation of 5 cm between the reference and reconstructed source positions is observed at a radius of ~ 4 m, close to the bottom of the IV.

Technical characteristics of the Borexino and its achieved performances are summarized in Table 7. The lower threshold on electrons energy used in the analyses is quoted, the 50% efficiency of the trigger corresponds to significantly lower energy, ~50 keV. The number of PMTs corresponds to the nominal amount of the installed PMTs. The detector was never

Table 7
Principal technical characteristics of the Borexino and KamLAND detectors. The light yield is characterized by the amount of the detected photoelectrons (PEs)

Characteristic	Borexino	KamLAND
LS	PC+PPO(1.5 g/l)	PC(20%) in $C_{12}H_{26}$+PPO(1.36 g/l)
LS density (g/cm^3)	0,880 (at 15 C)	0.780 (at 11.5 C)
Geometrical coverage (% of 4π)	31	34
Number of PMTs	2212(8″)	1325 (17″)+554(20″)
Attenuation length	>10 m at 430 nm	10 m at 400 nm
Light yield (PEs/1 MeV)	~500 for 2000 PMTs	~500
	(~11,500 photons)	(~8300 photons)
Energy resolution (1σ) (%)	~$5 \cdot \sqrt{E(\text{MeV})}$	~$6.4 \cdot \sqrt{E(\text{MeV})}$
IV size (radius) (m)	4.25	6.5
Full mass (t)	278	1000
Energy threshold for e$^-$ (keV)	180	~800
Muon detection efficiency	10^{-4} inefficiency	
Trigger rate (cps)	11	
Spatial resolution (cm)	~14 @ 1 MeV	~$12 \cdot \sqrt{E(\text{MeV})}$

operating the full set of the PMTs since significant amount of the PMTs (~10%) failed after the filling of the detector with water.

Borexino has an energy resolution of ~5% at 1 MeV, very good one for a liquid scintillation detector of its size. This is the result of the high light yield and high transparency of the LS. The latter ensures the excellent uniformity of the detector's response throughout the volume, and, hence, low non-statistical contribution to the energy resolution. The number of working PMTs slowly decreases with time with a loss of about 50 per year [152]. In the last period used in solar neutrino analysis [153], the number of working channels was 1769 at the beginning of the data taking period (December 2011) and only 1383 at its end (May 2016). The energy resolution correspondingly decreased from the initial 5% at 1 MeV observed at the start of the data taking with ~1900 operating channels to ~6% at 1 MeV in 2016.

6.1.1. Radiopurity

The LS radiopurity was essential for the Borexino solar neutrino programme. The components of the 278 t of the LS and 889 t of the buffer liquid were purified in a devoted purification system that combined distillation, water extraction, gas stripping, and filtration. The PPO was purified in a concentrated PPO solution in PC (master solution) by filtration and water extraction and distillation. All the storage and transportation tanks and in general all the surfaces in contact with LS were thoroughly cleaned and kept sealed after being filled with ultrapure nitrogen. The PC was prepared from crude oil extracted from very old Libyan layers, which guaranteed the low level of the contamination in ^{14}C that could not be removed by cleaning. The principles of operation, design, and construction of the purification system and the review of the requirements and methods to achieve system cleanliness and leak-tightness can be found in [154].

The levels of radiopurity achieved in Borexino and presented in Table 8, provide an important reference point for future experiments. The rate of ^{210}Po events is given in counts per day (cpd) for 1 t of the LS. For other isotopes the counting rates are much lower, and either the corresponding units per 100 t of the LS are used, or the contamination is expressed in grams of the contaminant contained in 1 g of the LS. The ^{14}C abundance is calculated from the evaluated counting rate of 40 ± 1 Bq/100 t [155]. The contents of ^{238}U and ^{232}Th are obtained from the detected counting rates of ^{222}Rn (by counting ^{214}Bi-Po coincidence events) and that of ^{220}Rn (by ^{212}Bi-Po coincidence events), assuming secular equilibrium in the corresponding decay chain. The ^{210}Po decay is not in equilibrium with the parent nuclei, as could be concluded from the observed decrease in the ^{210}Po counting rate with the characteristic time constant [150] corresponding to the ^{210}Po life-time T$_{1/2}$ = 138.4 d. The observed long-term time variations of the ^{210}Po counting rate were more complex compared to a simple exponential decay. Significant instantaneous increases of the counting rate were associated with operations and changes in the environment, see [150] for details. The ^{210}Po rate was as low as ~2.6 cpd/t in 2017 [153]. Since the only possible source of technogenic ^{85}Kr, contained in the gaseous exhaust of the nuclear power plants, is the atmospheric air, it is expected that the count of ^{39}Ar will be proportional to the ratio of ^{85}Kr/^{39}Ar in the air.

It should be noted that for some contaminants the achieved levels exceed the demands of the solar neutrino programme. As a result, a very low random coincidence count caused by intrinsic contamination is expected in Borexino. Nevertheless, external sources can produce γ's energetic enough to penetrate into the sensitive volume. All construction materials were carefully selected in order to reduce their amount. The closest to the sensitive volume material is nylon of the containment vessel and its supporting strings, and their contamination would be most critical for the Borexino programme. Nylon was carefully selected to guarantee low contamination with ^{238}U (1.7 ppt measured) and the absence of potassium in view of the fact that the nylon ropes are frequently treated with potassium salts to improve their mechanical properties [148]. However, the residual contamination of the IV restricts the use of the whole IV volume, and the FV cut is used in the analysis, to exclude the most external layer of the LS.

Table 8

Radiopurity levels achieved in two phases of Borexino compared to the typical abundances and the Borexino solar programme requirements.

Background	Typical abundance (source)	Borexino goals	Borexino-I [150]	Borexino-II [153]
^{14}C/^{12}C (g/g)	$\sim 10^{-12}$ (cosmogenic)	$\sim 10^{-18}$	$(2.7 \pm 0.1) \cdot 10^{-18}$	$2.7 \cdot 10^{-18}$
^{11}C (cpd/100 t)	(cosmogenic)	Not specified	27.4 ± 0.3	26.8 ± 0.2
^{238}U (g/g)	$10^{-6} - 10^{-5}$ (dust)	$\sim 10^{-16}$ (1 μBq/t)	$(1.6 \pm 0.1) \cdot 10^{-17}$	$< 9.4 \cdot 10^{-20}$(95% C.L.)
^{232}Th (g/g)	$10^{-6} - 10^{-5}$ (dust)	$\sim 10^{-16}$	$(6.8 \pm 1.5) \cdot 10^{-18}$	$< 5.7 \cdot 10^{-19}$(95% C.L.)
^{222}Rn (cpd/100 t)	100 cm^{-3} (air)	10	~ 1	0.1
^{40}K (g[K$_{nat}$]/g)	$2 \cdot 10^{-6}$ (dust)	$\sim 10^{-15}$	$< 1.7 \cdot 10^{-15}$95% C.L.	n.a.
^{210}Po (cpd/t)	Surfaces (^{222}Rn,^{210}Pb)	$\sim 10^{-2}$	80 (max. initial)	2 (initial)
^{210}Bi (cpd/100 t)	High (^{222}Rn,^{210}Pb)	Not specified	20–70	~ 20
^{85}Kr (cpd/100 t)	1 Bq/m^3 (air, [156])	~ 1	30.4 ± 5.5	6.8 ± 1.8
^{39}Ar	13 mBq/m^3 (air, [156])	~ 1	~ 0.4	$\sim 1.3 \times 10^{-2} \cdot$ R(^{85}Kr)

6.1.2. Selection of antineutrino candidates

The antineutrino candidate selection criteria in Borexino are presented in Table 9.

The cosmogenic backgrounds are removed by using the muon veto tag. If a muon passing through the OD without entering the ID is identified, a 2 ms time window is excluded from the analysis in order to avoid false antineutrino candidate events caused by neutrons. Additionally, a 2 s veto is applied after each muon passing through the scintillator volume in order to suppress the ^{9}Li– ^{8}He background. The total loss of the live-time due to these vetoes is about 11%. The low energy cut on the prompt event is set slightly below the kinematic threshold of the IBD allowing to take into account the energy resolution broadening. The low energy threshold of the neutron energy window was increased in the latest analysis, since in this analysis the data set with increased ^{222}Rn was included. This contamination was observed after the LS purification tests. No high energy cut was applied on the prompt event. The cut on the delayed event energy was tuned to accept the peak of the 2.2 MeV γ from the neutron capture in the whole FV used in the geoneutrino analysis. The α/β selection cut based on a Gatti filter [150] is applied on the delayed signal to prevent false coincidence due to the ^{214}Po($\alpha + \gamma$) events leakage; the cut was absent in the first analysis of 2010. No pulse shape cut is applied on the prompt candidate. A cut on the time difference between the prompt and the delayed events is applied, requiring $20 < \Delta T < 1280$ μs. The upper limit corresponds to 5 lifetimes of the neutron in the LS of 259.7 ± 2.4 μs [157]. The lower bound of the time cut is related to the specific features of the Borexino electronics, where the hardware trigger opens a window 13.5 μs long, and thus two correlated events with $\Delta T < 13.5$ μs will belong to one trigger, and a special algorithm would be needed to extract the antineutrino candidate. To avoid this unnecessary complication, $\Delta T > 20$ μs was chosen slightly exceeding the length of a single event window. A cut on the relative distance between the prompt and the delayed events is applied, demanding $\Delta R < 1$ m. In the latest analysis two cuts were added: the "multiplicity" cut and the fast ADC (FADC) one. The multiplicity cut rejects events either preceded or followed by neutron-like events within a 2 ms window, as these are most likely the events caused by two fast neutrons. The FADC cut consists in the complementary check of candidate events using an independent 400 MHz digitizer acquisition system installed with the aim of increasing the dynamic range of the Borexino electronics for better supernova event processing.

The total detection efficiency of these basic candidate selection criteria within the FV (all but the muon veto cut) was determined through Monte Carlo (MC) simulations to be $\epsilon = (84.2 \pm 1.5)$%, not depending on energy. External background from (α, n) reactions in the buffer was removed by excluding the events occurring in the vicinity of the IV wall, namely $\Delta d < 30$ cm (or $\Delta d < 25$ cm in earlier analyses). The Borexino spatial selection does not assume spherical symmetry of the IV. The position of the IV walls is reconstructed on a weekly basis using events originating from the radioactive contaminants of its material. The overall uncertainty of the total exposure includes systematic errors of the reconstruction of the vessel shape (1.6%) and that of the position of the prompt event (3.8%), other selection criteria contribute no more than 1%.

The time and radial distributions of the candidate events were checked against the expected ones. The distribution of the time difference between the delayed and the prompt events should be compatible with that of the neutron capture time. All prompt events should have a negative Gatti parameter, confirming that they are not caused by α's or protons.

6.1.3. Geoneutrino analysis

Borexino reported the first geoneutrino observation at more than 4σ C.L. in 2010, providing updates of the analysis in 2013 and 2015. The progress of the analysis is presented in Table 10.

The antineutrino spectra expected in Borexino are shown in Fig. 10. The geoneutrino contribution was calculated assuming a chondritic Th/U mass ratio. To make the effect of neutrino oscillations evident, the spectra are shown with and without neutrino oscillations. For the geoneutrinos, the oscillations result roughly in the scaling of the absolute normalization of the spectrum. In contrast, the spectral shape of reactor antineutrinos demonstrates visible oscillation patterns in the absence of the smearing by the detector's energy resolution. The geoneutrino and antineutrino spectra as well as those for other backgrounds, are simulated using a Geant-4-based MC model of the detector [159]. The code

Table 9

Antineutrino candidate selection in the KamLAND and Borexino analyses. Indices "p" and "d" stand for the prompt and delayed events. Borexino performs selections in the "light yield scale" (measured in photoelectrons); ΔR is the reconstructed distance between the prompt and delayed events; ΔT is the time difference between the prompt and delayed events; $R_{IV}(\theta, \phi)$, in Borexino's case, is the radial position of the IV wall in the direction (θ, ϕ); T_μ is the time passed after the preceding muon. The radius of the KamLAND inner vessel is $R_{det} = 6.5$ m, and thus the external 50 cm are cut out. The selection criteria for both KamLAND and Borexino have been changed since the first analysis. We show here the ones from the latest published papers.

| Cut	KamLAND-2013	Borexino-2015
Prompt event energy	$0.9 < E_p < 8.5$ MeV	$Q_p > 408$ PEs
Delayed event energy	$1.8 < E_d < 2.6$ MeV	$860 < Q_d < 1300$ PEs
	or $4.4 < E_d < 5.6$ MeV	
ΔR	$\Delta R < 2$ m	$\Delta R < 1$ m
ΔT	$0.5 < \Delta T < 1000$ μs	$20 < \Delta T < 1280$ μs
Spatial	$R_p < 6$ m and $R_d < 6$ m	$R_{IV}(\Theta, \phi) - R_p(\Theta, \phi) > 0.30$ m
	$R_d > 2.5$ m, $\rho_d > 2.5$ m and $Z_d > 2.5$ m	
T_μ	$T_\mu > 2$ s (showering muons)	$T_\mu > 2$ s (every muon in ID)
	$+ \; T_\mu > 2$ ms (all muons)	$+ \; T_\mu > 2$ ms (all muons)
Likelihood	$L > L_{cut}(E_p)$	None
Pulse shape	None	$g^d_{\alpha\beta} < 0.015$
Multiplicity	None	Multiplicity = 1
FADC	None	FADC

Table 10

Borexino results on the geoneutrino flux measurements. The results are presented for the electron antineutrino flux since only antineutrinos of this flavour are detected. The total flux of all antineutrino flavours is approximately $1/\langle P_{ee} \rangle \simeq 1.8$, times higher. Exposure of 1 t yr in KamLAND corresponds to 8.48×10^{28} protons yr, and 1 TNU corresponds to the 1.1×10^5 cm^{-2} s^{-1} electron antineutrino flux. The last column presents the probability of the absence of the geoneutrino signal in the corresponding data set (null-hypothesis).

Year	Live-time (days)	Exposure (protons yr $\times 10^{31}$)	Number of IBD candidates	Number of geo $\overline{\nu_e}$s	Geo $\overline{\nu_e}$ signal (TNU)	Geo $\overline{\nu_e}$ flux $\times 10^6$ cm^{-2} s^{-1}	P(H$_0$)
2010 [14]	537.2	1.52	21	$9.9^{+4.1}_{-3.4}$	65^{+27}_{-22}	$7.4^{+3.1}_{-2.5}$	$3 \cdot 10^{-5}$ (4.2σ)
2013 [158]	1363	3.69 ± 0.16	46	14.3 ± 4.4	38.8 ± 12.0	4.4 ± 1.4	$6 \cdot 10^{-6}$ (4.9σ)
2015 [143]	2056	5.46 ± 0.27	77	$23.7^{+6.5}_{-5.7}$	$43.5^{+12.1}_{-10.7}$	$5.0^{+1.4}_{-1.2}$	$3.6 \cdot 10^{-9}$ (5.9σ)

produces input spectra by converting the initial energy randomly picked from the corresponding spectrum to the chosen detector's observable. The non-uniformity of the detector response function and non-linearities of the energy scale are automatically accounted with this approach. The MC code was tuned using the data of the extensive calibration campaign with a set of gamma sources. The energy of the gamma rays ranged between a few hundred keV and 9 MeV [151]. These calibration data were used to reduce the systematic error associated with all Borexino results and to optimize the MC simulation of the detector response.

The spectra obtained in this way are used to fit the experimental data. In the geoneutrino analysis, the most suitable observable (energy estimator) is the total collected charge from PMTs expressed in the amount of detected photoelectrons (PEs). It offers the best energy resolution above 1 MeV, in particular due to the fact that its spatial variation across the FV is the smallest among the energy estimators used in the Borexino analyses [150]. The number of PMTs in operation is defined on-line and stored for each event. Using this information, the energy estimator of the event is scaled (normalized) to 2000 working PMTs in order to exclude the non-statistical contribution to the energy resolution, that otherwise will appear because of the variations of the number of PMTs in operation. Another correction is applied to take into account the non-uniformity of the light collection for events of the same energy at different positions. The energy of each event is reconstructed using the total amount of light registered by all PMTs of the detector (measured in PEs) and corrected with a position-dependent light collection function $f(x, y, z)$, which relates the light yield at a point (x, y, z) to that of the event with the same energy deposited at the centre of the detector, $Q(x, y, z) = f(x, y, z) \, Q_0$. For events at the centre of the detector with energies above 1 MeV the total amount of collected light is linear with respect to energy, as shown by calibrations [160].

The expected event rate and the spectral shape of the reactor antineutrinos were calculated by considering all reactors around the world. The variation of the thermal power of individual cores was accounted for by using the monthly mean load factor provided by the IAEA [127]. The power fractions (PFs) ^{235}U : ^{238}U : ^{239}Pu : ^{241}Pu of a typical reactor used in the calculations were 0.56:0.08:0.30:0.06 with a systematic error of 3.2% due to possible differences among the fuels of different cores and the unknown stage of burn-up in each reactor [14]. For 35 European reactors using the Mixed Oxide (MOX) technology 30% of thermal power was considered to have 0.000 : 0.080 : 0.708 : 0.212 PFs [14]. In the latest analysis the more precise PFs of 0.542 : 0.411 : 0.022 : 0.0243 were used for the 46 cores using heavy water moderator [143,158]; the associated correction is very small, $\sim 0.1\%$, as only two reactors of this type are located in Europe. The matter effect on the neutrino propagation increases the observed signal by 0.6%, and 1% increase is due to the contribution of the long-lived fission products in the spent fuel. The predicted signal from the nuclear reactors corresponds to (87 ± 4) TNU.
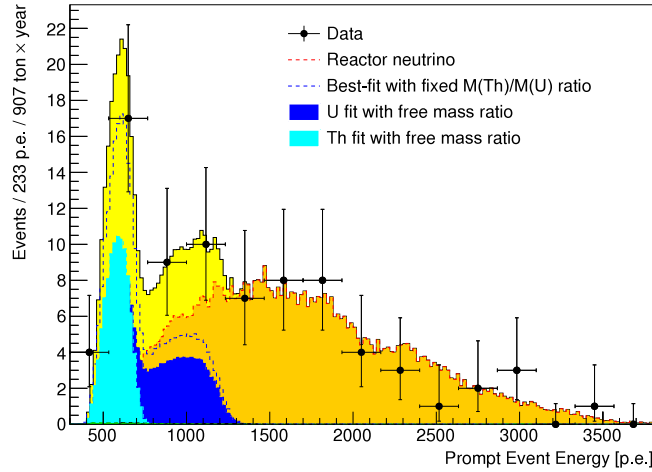
Fig. 12. The light yield spectrum of prompt events of antineutrino candidates in Borexino, the energy scale is in units of PEs. The best-fit in assumption of the chondritic Th/U mass ratio corresponds to the upper curve fitting the data (yellow coloured area). The best-fit reactor antineutrino spectrum coincides with the best fit curve above the end-point of the geoneutrino spectrum (orange coloured area), while the best-fit spectrum of geoneutrino is shown with a dashed line (characteristic curve at low energies, blue). The contributions of U and Th corresponding to the best-fit with free Th/U mass ratio are shown too. The Th contribution has bell-like shape visible at the beginning of the scale (light-blue coloured area), the U contribution expands to ∼1300 PEs (blue coloured area).
Source: Fig. from [143].

The non-reactor background sources in Borexino are at negligible levels. In the most recent analysis the set of 77 candidate events contained $0.78^{+0.13}_{-0.10}$ event from the major part of the non-reactor backgrounds, and less than 0.65 event at 90% C.L. can be associated with the remaining possible sources of background, namely from (α, n) reactions in the buffer and from the fast neutrons generated by muons crossing the rocks [143]. The upper limits in the latter case are set in a conservative approach, since the absence of precise information does not allow more accurate calculations.

The rate and shape of the accidental coincidences spectrum was obtained by shifting the delayed time window to 2–20 s, while keeping all other cuts unchanged. The energy spectrum of these events is below 3 MeV, overlapping the geoneutrino spectrum. Time correlated events have been searched for in the (2 ms, 2 s) time window. A negligible amount of correlated events with a ∼1 s time constant were identified, and their contribution in the antineutrino time window was determined. The average rate of ^{210}Po decays in the data set is determined to be 14.1 ± 0.2 cpd/t, this value is used to constrain the (α, n) reaction contribution.

An unbinned likelihood fit of the energy spectrum of 77 selected prompt $\overline{\nu}_e$ candidate events shown in Fig. 12 was performed with the reactor and geoneutrino spectra obtained by MC simulation. The Th/U mass ratio was fixed to a chondritic value of 3.9 in the geoneutrino spectrum. Either the measured background energy spectrum (accidental coincidences) or the ones obtained through the MC simulations (^{9}Li, ^{8}He, (α, n) backgrounds) were used in the fit. The other components were not included in the fit because of the uncertainty in their energy spectrum and negligible (∼1%) contribution. The normalizations of the geoneutrino spectrum and the reactor antineutrino spectrum were both left free fit parameters without implying any constraints. In contrast, the normalizations of the background components were constrained as pull parameters around the expected values.

The fit returns

$$N_{geo} = 23.7^{+6.5}_{-5.7}(\text{stat})^{+0.9}_{-0.6}(\text{syst}) \tag{46}$$

geoneutrino events and

$$N_{react} = 52.7^{+8.5}_{-7.7}(\text{stat})^{+0.7}_{-0.9}(\text{syst}) \tag{47}$$

events caused by the reactor antineutrinos, or, expressed in TNU units

$$S_{geo} = 43.5^{+11.8}_{-10.4}(\text{stat})^{+2.7}_{-2.4}(\text{syst}) \quad \text{TNU} \tag{48}$$

and

$$S_{react} = 96.6^{+15.6}_{-14.2}(\text{stat})^{+4.9}_{-5.2}(\text{syst}) \quad \text{TNU}. \tag{49}$$

The results include systematic uncertainties from both the exposure uncertainty of 4.8% and the uncertainty of 1% arising due to the energy calibration. The observed geoneutrino signal corresponds to $\overline{\nu}_e$ fluxes at the detector of $\phi(\text{U}) = (2.7 \pm 0.7) \times 10^6$ cm^{-2} s^{-1} for the U chain and $\phi(\text{Th}) = (2.3 \pm 0.6) \times 10^6$ cm^{-2} s^{-1} for the Th chain, respectively. Here statistical and systematic uncertainties are summed in quadrature. Borexino observes a non-zero geoneutrino contribution
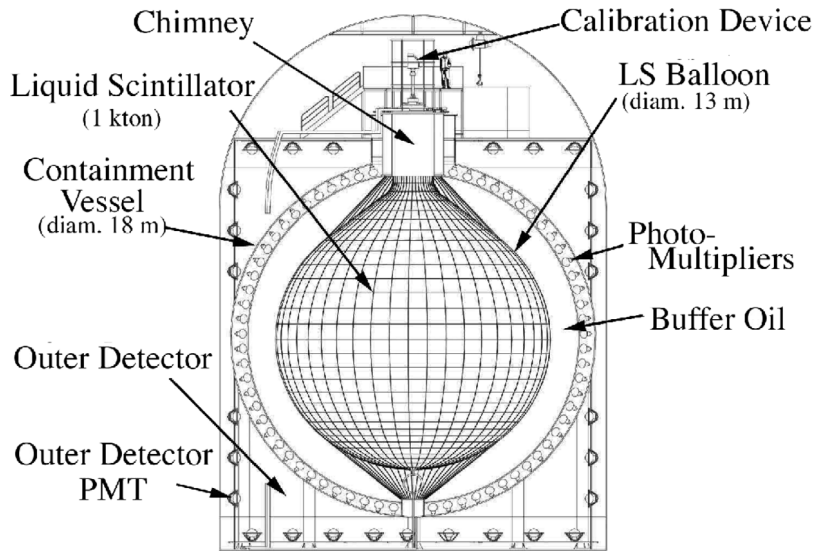
Fig. 13. Schematic view of the KamLAND detector (courtesy of KamLAND collaboration).

in the experimental data with the 5.9σ significance. The null hypothesis for geoneutrino observation has a probability of 3.6×10^{-9}.

6.1.4. Future

The Borexino detector will continue to accumulate data for at least another year, until the end of 2020. By the end of 2018 available statistics was increased by $\sim$40%, compared to the 2015 analysis. The collaboration plans to improve the performance of the muon-veto cut following KamLAND's approach. This should save about 9% of livetime, and 13% of exposure can be recovered by increasing the FV (by reducing the excluded outer shell to 10 cm) and decreasing the lower energy cut for the delayed event. About 4% of exposure can be recovered by including pairs of events occurring below the lower time cut of 20 μs excluded in previous analyses. Increasing the statistics and using the optimized selection cuts will make it possible to reduce the uncertainty of the total geoneutrino flux measurement from the actual 26% down to $\sim$20% [161].

6.2. KamLAND experiment

KamLAND is a reactor antineutrino experiment with a 180 km baseline, perfectly suited to the search for neutrino oscillations in the so-called large mixing angle (LMA) parameter region; at these parameters the expected oscillation length roughly corresponds to 100 km.

The KamLAND detector is located in the Kamioka mine in Japan. Its design is similar to that of the Borexino detector (see Fig. 13). A dome-like stainless steel structure with a cylinder base 18 m in diameter is filled with 3.2 kt of ultrapure water. A 9-m-radius stainless steel sphere placed inside the cylinder divides the detector into two volumes: external, serving as a water Čerenkov detector of cosmic muons, and internal, containing the neutrino target within a transparent vessel with 135-μm-thick walls with the total volume of 1171 ± 25 m^3. The Inner Vessel (IV) supported by a network of Kevlar ropes contains 1000 tonnes of 20% solution of pseudocumene in dodecane ($C_{12}H_{26}$), with addition of 1.36 ± 0.03 g/l of PPO fluor, the latter serves to improve the scintillating properties. The mixture density is 0.780 g cm^{-3} at 11.5 °C. The PC increases light emission but decreases transparency. The composition of the scintillator was adjusted to obtain the maximum light yield for the events at the centre, suffering more from the LS transparency compared to the non-central ones. Scintillation flashes within the inner detector (ID) are observed by 1879 PMTs of two types: 1325 specially developed 20-in. PMTs masked to 17-in. diameter in order to improve timing characteristics and 554 older type 20-in. ones, reused from the Kamiokande experiment. The PMTs provide a total geometric coverage of 34%. The light yield before the second purification was 300 PEs/MeV with 17-in. PMTs only and 500 PEs/MeV for the complete set of 17+20-in. PMTs. The attenuation length was measured by a dye-laser, it is about 10 m at the 400 nm wavelength. The light output of the LS is 8300 photons/MeV [162].

Mineral oil (a mixture of 53% normalparaffin, $C_{12}H_{26}$, and 47% of isoparaffin, C_nH_{2n+2}, n$\sim$14), serving as a protection against external γ's and neutrons, fills the gap between the 9-m-radius SSS and the IV. The buffer liquid is 0.04% less dense than the LS. The detector has an additional transparent sphere with the radius of 8.3 m dividing the buffer into two subvolumes. It serves as a barrier against possible convective transfer of radon emanating from the SSS and the PMTs.

The Čerenkov light in the Water Tank (WT) is detected by 225 PMTs mounted on the internal WT wall and forming the outer detector (OD).

The KamLAND front-end electronics system based on the analog transient waveform digitizer (ATWD) captures PMT signals in 128 10-bit digital samples at intervals of 1.5 ns. Each ATWD captures three gain levels of a PMT signal providing a wide dynamic range from 1 to 1000 PEs covering the energy deposits of up to 30 MeV [163]. To reduce the dead time, two ATWDs are attached to each PMT. The trigger electronics receives 125 ns logical signals from front-end discriminators set at the 0.15 PE (∼0.3 mV) threshold and counts the number of triggered ID and OD PMTs with a sampling rate of 40 MHz. The trigger level is set at the number corresponding to the deposited energy of ∼0.8 MeV. Only fast 17″ PMTs are used for the trigger. The OD readout is triggered in a similar way.

The energy of events is reconstructed off-line using the total collected charge corrected for the variation of the number of PMTs in operation, dark noise, solid angle, shadowing by suspension ropes, optical transparencies, and scattering properties in the LS. The relation between the total collected charge (or visible energy E_{vis}) and the deposited energy E_{dep} is non-linear and is modelled for each type of particle, taking into account ionization quenching (Birks' mechanism) and Čerenkov light emission. The scale is adjusted using 2.2 MeV γ from the neutron capture on the proton as a reference (i.e., by setting $E_{vis} = E_{dep}$). From 5 March 2002 to 27 February 2003 the geometric coverage was only 22%, and the observed energy resolution was ∼7.4% at 1 MeV approximately scaled as $1/\sqrt{E_{vis}}$. For the rest of the data, with the 20-in. PMTs installed, the energy resolution improved to ∼6.4% at 1 MeV.

The energy scale was calibrated using a number of radioactive sources deployed in various positions within the 5.5 m distance from the detector centre and covering a range of energies between 0.28 and 6.1 MeV [164]. The sources used for calibrations included γ-sources: ^{203}Hg, ^{68}Ge, ^{65}Zn, and ^{60}Co; and n + γ sources: ^{241}Am + ^{9}Be and ^{210}Po + ^{13}C (the latter was proposed by McKee et al. [165]). The energy scale was also calibrated using internal radioactive contaminants distributed in the IV, such as ^{40}K and ^{208}Tl, the tagged delayed fast coincidence of ^{212}Bi − ^{212}Po decays from the ^{232}Th chain, and the delayed coincidence of ^{214}Bi − ^{214}Po decays from the ^{238}U chain, cosmogenic ^{12}B and ^{12}N, and γ's from neutron captures on the proton and the ^{12}C.

Vertices of low-energy (< 30 MeV) events are reconstructed using times of arrival of photons to the PMTs. In order to compensate for the possible difference in the PMTs time response, the timing calibration is performed using short light pulses from the dye laser delivered through the optical fibre to the detector centre. Calibration sources were used to verify the vertex reconstruction code by comparing the reconstructed position against the known position of the source. An average position reconstruction uncertainty of less than 3 cm was found for events with energies in the range from 0.28 to 6.1 MeV. The vertex reconstruction is essential as it is used in the selection cuts to estimate the distance between the prompt and delayed events, and it provides also the input for the active veto against the external backgrounds by removing events in the vicinity of the more radioactive walls of the IV. In the spherical detector the latter selection criterion in its simplest form will be the radial cut. The absolute precision of the vertex reconstruction is responsible for the uncertainty of the FV mass, i.e., the number of target protons. The statistical precision of the point-like event reconstruction is ∼14 cm at 1 MeV. The position resolution for the 2.506 MeV γ from the ^{60}Co source is 19 cm, scaled as $30/\sqrt{(E[\text{MeV}])}$ cm with energy [163]. More details can be found in [136,166].

The dominating contribution to the antineutrino signal detected by KamLAND before the Fukushima event originated from the ≃70 Japanese reactors with total thermal power of 130 GW, located at an average distance of 180 km from the detector, with an expected reactor antineutrino flux of ∼ 10^7 cm^{-2} s^{-1}. Antineutrinos are detected in the IBD of the proton. The thermalized neutron life-time is 207.5 ± 2.8 µs before being captured on the proton.

KamLAND presented its first results on reactor antineutrino oscillations with the 162 t yr exposure in 2003 [167]. The next analyses used exposure of 766 t yr [168] and 2.881 kt yr [166] respectively. In the latter analysis the statistical significance of spectral distortions exceeded the 5σ level, and the analysis of the reactor spectra was performed from the IBD threshold including among others the geoneutrino contribution. The first geoneutrino study appeared in 2005 on the data set from 7.09×10^{31} target proton years [13]. The total number of detected geoneutrinos of 4.5 to 54.2 for a 90% confidence interval was reported with the Th/U mass ratio fixed at 3.9. The upper limit on the antineutrino flux was set to 1.62×10^7 cm^{-2} s^{-1} at 99% C.L., corresponded to a limit of 60 TW for radiogenic heat production from the U and Th chains.

Together with the accumulation of new data, the selection cuts were tuned, including the decrease of the energy threshold and increase of the FV by one third, due to the increase of the radial cut from 5 to 5.5 m. The straightforward increase of the statistics with time would not result in significant improvement of the uncertainties because of the presence of the strong background from the (α, n) reaction on ^{13}C in the low-energy part of the spectrum, caused by the high content of ^{210}Pb. The isotope have life-time of 22.7 yr, supporting the daughter ^{210}Po with a shorter life-time, which is the main source of α's in the LS[17] [169]. In 2007 a purification campaign began with the aim of achieving purity levels suitable for the solar neutrino programme. As a result, the contribution of the ^{13}C$(\alpha, n)^{16}$O reaction decreased by a factor of ∼20, and the signal-to-background ratio was significantly improved in the energy range below 2.6 MeV. In the next round of analysis [170], the KamLAND collaboration used the data from March 9, 2002 to November 4, 2009 (2135 days). The FV was further increased by 0.5 m, up to 6 m, and the total exposure reached 4.116 kt yr.

---

[17] In contrast, in Borexino "unsupported" ^{210}Po was observed, not in equilibrium with its parent ^{210}Pb.
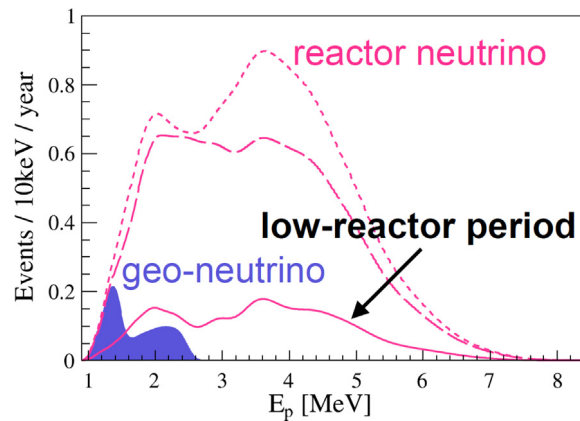
Fig. 14. Expected reactors and geoneutrino energy spectra before and after shutdown of the Japanese reactors. The reactors energy spectrum after the partial shutdown is marked as low-reactor period in the plot. E_p is visible energy of the prompt event.
Source: Fig. from [144].

In September 2011, KamLAND started to take data with the updated experimental facility, KamLAND-Zen, with the main goal of the search for neutrinoless double beta decay. The target isotope ^{136}Xe is dissolved in 13 t of the LS contained in a small balloon with radius 1.54 m placed at the detector centre. The presence of the balloon does not interfere much with the geoneutrino studies. Only a very small fraction of the total volume is affected, which can be removed by applying the corresponding spatial cut. An important point for the geoneutrino study in the KamLAND-Zen experiment was in 2012, when, following the Fukushima event, the Japanese nuclear power plants were switched off for checks and maintenance. The idea to use the information on the thermal power of nuclear plants in view of the geoneutrino signal extraction was discussed before these dramatic events [171]. After May 2012, when the last reactor was switched off, the reactor-to-geoneutrino signal ratio is practically the same as in the Borexino experiment. The decrease of the reactor signal is illustrated in Fig. 14.

The total data set can be divided into three periods. Period I with 1486 days of live-time refers to the data taken from 2002 to May 2007, before the LS purification campaign that continued until 2009. Period II with 1154 days of live-time refers to the data taken until the autumn of 2011 during and after the LS purification campaign. Period III started since September 2011 after the installation of the internal Xe balloon for KamLAND-Zen experiment. Time evolution of expected and observed antineutrino rates in KamLAND for two energy ranges (below and above the energy geoneutrino edge) is shown in Fig. 15. The contribution of geoneutrinos to the second region is negligible. The oscillation parameters used to calculate the expected reactor antineutrino rate were the best-fit values from the global oscillation analysis.

6.2.1. Radiopurity

Initially, the LS and the buffer oil were purified by a water extraction process during the detector filling in March 2002. The levels of achieved radiopurity were $(3.5 \pm 0.5) \cdot 10^{-18}$ g/g for ^{238}U, $(5.2 \pm 0.8) \cdot 10^{-17}$ g/g for ^{232}Th, and $< 2.7 \cdot 10^{-16}$ g/g for potassium. Nevertheless, contamination with ^{85}Kr at the level of 883 ± 20 μBq/kg and with daughter isotopes of ^{222}Rn was observed. The decay rate of ^{210}Pb was 58.4 ± 1.1 μBq/kg, as inferred from the decay rates of its unstable daughters ^{210}Bi and ^{210}Po [173]. Though the resulting single event counting rate of 8.1×10^7 (kt d)$^{-1}$ was acceptable for the antineutrino programme, the solar neutrino one would be impossible without further purification. The presence of a significant amount of ^{210}Po estimated at 95 Bq in the whole volume [31] was also a source of noticeable (α, n) background for geoneutrino study.

The KamLAND collaboration developed methods for efficient removal of Kr and Pb from the LS aiming to achieve the radiopurity levels for low-energy physics programme [174]. The second purification campaign was performed in 2007–2009 by distillation and nitrogen purging of each LS component. The distillation is expected to reduce high-boiling point metal elements such as ^{210}Pb and ^{40}K, while nitrogen carries away the radioactive noble gases ^{222}Rn, ^{85}Kr and ^{39}Ar. After the second purification, the radioactive impurities were further reduced to $(1.5 \pm 1.8) \cdot 10^{-19}$ g/g in ^{238}U, to $(1.9 \pm 0.2) \cdot 10^{-17}$ g/g in ^{232}Th, and in to a limit $< 2.7 \cdot 10^{-16}$ g/g in natural K. The content of the ^{222}Rn daughters was reduced to 2 mBq/m^3 for ^{210}Po, below 1 mBq/m^3 for ^{210}Bi, and to ~ 0.1 mBq/m^3 for ^{85}Kr. The overall reduction factors for counting rates of ^{85}Kr, ^{210}Bi, and ^{210}Po are about 6×10^{-6}, 8×10^{-4}, and 5×10^{-2}, respectively. After the second purification, the main source of accidental coincidences are events from the vessel walls, possibly due to dust contamination during the IB film assembly and air leakage during the LS purification.

6.2.2. Selection of antineutrino candidates

The antineutrino candidate selection criteria of the more elaborated KamLAND analysis of 2013 are presented in Table 9. KamLAND performs energy selections using reconstructed energy. Note the difference in the radial cuts:
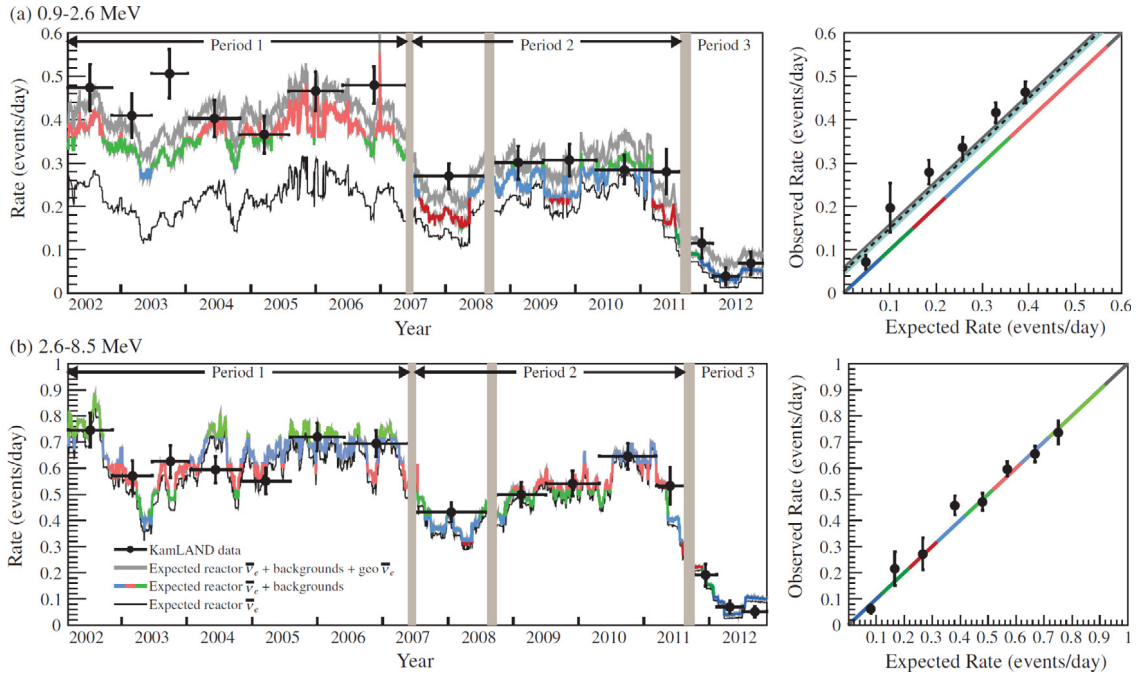
Fig. 15. Time evolution of expected and observed rates at KamLAND for antineutrinos with prompt event visible energies (a) in the geoneutrino energy window, 0.9–2.6 MeV in this analysis, and (b) above the geoneutrino energy window, 2.6–8.5 MeV. The points indicate the measured rates, while the curves show the expected rate variation for different combinations of signals and backgrounds and are almost indistinguishable in the lower plot. In the upper plot the lines indicate reactor antineutrinos (lower thin line), reactor antineutrinos plus backgrounds (coloured middle line), and reactor antineutrinos+backgrounds+geoneutrinos (grey upper line). The data periods excluded from the analysis are shaded by thick bars. In the right panel the observed event rate for each group is plotted at the exposure-weighted versus expected event rate. The efficiency-corrected best-fit value of the geoneutrino rate from the full spectral analysis (dashed line), its 1σ error (shaded region), and the model expectation (grey line) are drawn for comparison.
Source: Figure from [172].

Borexino's is based on the position of the prompt event, and in KamLAND both prompt and delayed events should be within the FV radius. This leads to a relative depletion of the outer layer with detected candidates in the KamLAND analysis. The selection of the FV decreases the amount of target protons: in KamLAND a 50 cm layer is removed, while in the first analysis a much thicker layer of 150 cm was removed. For the crossing muons KamLAND used more advanced selections compared to Borexino, which were aimed to tag showering muons only. This results in a moderate loss of 4% live-time in comparison to 11% for Borexino; the difference per crossing muon is even bigger if the higher muon flux at the Kamioka site is taken into account.

The low energy cut on the prompt event is set at the kinematic threshold of the IBD. The high energy cut corresponds to the maximum energy of the reactor antineutrino spectrum. The cut on the delayed event energy accepts the peak of the 2.2 MeV γ from the neutron capture on the proton, and the 4.95 MeV γ from the neutron capture on ^{12}C. No pulse shape cuts are applied in the KamLAND analysis. A cut on the time difference between the prompt and the delayed events requires $0.5 < \Delta T < 1000$ μs. The upper limit corresponds to 5 life-times of the neutron in the KamLAND LS (207.5 ± 2.8 μs). A cut on the relative distance between the prompt and the delayed events, $\Delta R < 2$ m, is less stringent compared to Borexino. The software-defined FV in KamLAND is a sphere with a radius of 6 m. In the last period, an additional FV cut in the antineutrino analysis is applied to exclude the contamination from the Xe balloon. In the lower hemisphere an inner spherical volume with a radius of 2.5 m is excluded, and the cylindrical volume with a radius of 2.5 m is excluded in the upper hemisphere.

An additional event selection is applied to suppress accidental coincidence backgrounds while maintaining high efficiency for antineutrinos. A figure-of-merit is constructed on the basis of the PDFs for antineutrinos rate, f_ν, and accidental coincidences rate, f_{acc}, obtained by a combination of MC, data-driven, and analytical methods. The PDF is based on six cut parameters: E_p, E_d, ΔR, ΔT, R_p, R_d. For each candidate event the ratio $L = \frac{f_\nu}{f_\nu + f_{acc}}$ is calculated and tested against the value maximizing the figure-of-merit $\frac{S}{\sqrt{S+B_{acc}}}$ for prompt energy intervals of 0.1 MeV. S is the expected antineutrino signal assuming an oscillation-free reactor spectrum and predicted geoneutrino fluxes. B_{acc} corresponds to the number of accidental background events and is measured using an out-of-time delayed coincidence window (10 ms $< \Delta T < 20$ s). The efficiency of the selection cuts defined in this way has strong energy dependence and is calculated from the ratio of the MC-generated antineutrino events that passed the selections to the total number of the generated events. The systematic uncertainty is evaluated using calibrations with the ^{68}Ge and ^{241}Am-^{9}Be sources [170].
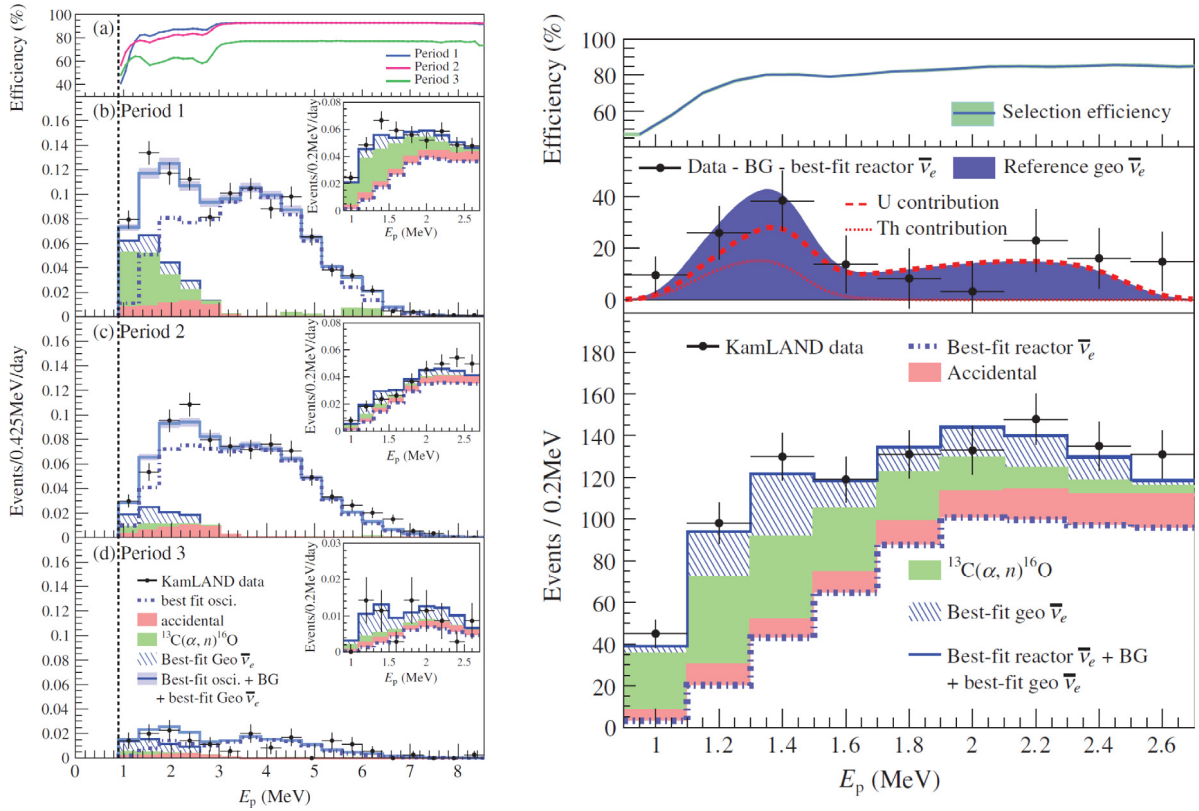
Fig. 16. Left: visible energy spectrum of $\overline{\nu}_e$ candidates prompt event shown separately for 3 data-taking periods, signed as Period I, Period II and Period III from top to bottom. The visible energy spectra of $\overline{\nu}_e$ candidate events in the geoneutrino energy range are shown in the insets with a finer binning. The very top panel shows the energy dependence of the $\overline{\nu}_e$ selection efficiency for each period. **Right:** energy spectrum of the $\overline{\nu}_e$ events in the geoneutrino region for the total data set up to 2013. Bottom panel: data together with the best-fit background and geoneutrino contributions. The shaded area corresponds to the background and geoneutrino contributions. The middle panel presents the observed geoneutrino spectrum after subtraction of other contributions. The dashed and dotted lines show the best-fit U and Th spectral contributions, respectively, and the blue shaded area corresponds to the estimation using the geological model [175]. The upper inset shows the selection efficiency curve.
Source: Figures from [172].

6.2.3. Geoneutrino analysis

The KamLAND geoneutrino analyses are presented in Table 11. In this section we mainly discuss the KamLAND analysis from [172], if otherwise explicitly stated. The more recent analysis from 2016 still has preliminary status.

Reactor fluxes are predicted from reactor operation records that include the thermal power, fuel exchange, and reshuffling data for all Japanese commercial reactors. The information is provided by a consortium of Japanese electric power companies. The thermal power generation is measured within 2% precision. The relative fission yields averaged over the live-time period for the 2013 publication were (0.567:0.078:0.298:0.057) for (^{235}U: ^{238}U: ^{239}Pu: ^{241}Pu), respectively. A calculation of the geoneutrino flux at KamLAND is based on the reference Earth model of Enomoto et al. [175]; 109 and 27 geoneutrino events from U and Th, respectively, were expected in the 2013 dataset.

The energy spectrum of $\overline{\nu}_e$ candidate events with visible energy above the 0.9 MeV energy threshold are shown in Fig. 16 separately for all 3 data taking periods analysed in [172]. The background, reactor, and geoneutrino contributions are the best-fit values from the KamLAND-only analysis. The decrease of the (α, n) background after the purifications is clearly seen in the second period. In the third period also the reactor antineutrino background decreased. In the right plot of Fig. 16 the total spectrum for all data taking periods up to 2013 is shown. The fit in the bottom panel includes all available constraints on the oscillation parameters.

The geoneutrino fluxes are extracted together with the neutrino oscillation parameters by using an unbinned maximum-likelihood method incorporating the event rate and the prompt energy spectrum shape, and accounting for their time variation. The fit is performed in the full energy range from 0.9 to 8.5 MeV. The expression for χ^2 is more complicated compared to the Borexino analysis, and includes two contributions for the time-varying event rate, the time-varying energy spectrum shape, five penalty terms for backgrounds constrained with accordance of their estimates, a penalty term for systematic uncertainties, and a penalty term for the oscillation parameters (see [172] for more details). The normalizations for the uranium and thorium signals can be treated independently and allow the analysis without

Table 11

KamLAND results on the geoneutrino flux measurements. The results are presented for the electron antineutrino flux since only antineutrinos of this flavour are detected. The total flux of all antineutrino flavours is approximately $1/\langle P_{ee} \rangle \simeq 1.8$, times higher. Exposure of 1 t yr in KamLAND corresponds to 8.48×10^{28} protons yr, and 1 TNU corresponds to the 1.1×10^5 cm^{-2} s^{-1} electron antineutrino flux. The last column presents the probability of the absence of the geoneutrino signal in the corresponding data set (null-hypothesis).

Year	Live-time (days)	Exposure (protons yr $\times 10^{32}$)	Number of IBD candidates	Number of geo $\overline{\nu_e}$s	Geo $\overline{\nu_e}$ signal (TNU)	Geo $\overline{\nu_e}$ flux $\times 10^6$ cm^{-2} s^{-1}	P(H$_0$)
2005 [13]	749.1	0.709 ± 0.035	152	25^{+19}_{-18}	43^{+35}_{-32}	$5.1^{+3.9}_{-3.6}$	4.6%
2008 [166]	1486	2.44	–	73 ± 27	39.4 ± 14.3	4.4 ± 1.6	0.45%
2011 [171]	2135	3.49 ± 0.07	841	106^{+29}_{-28}	$38.5^{+10.7}_{-9.8}$	$4.3^{+1.2}_{-1.1}$	$3 \cdot 10^{-5}$
2013 [172]	2991	4.90 ± 0.1	–	116^{+28}_{-27}	30.4 ± 7.2	3.4 ± 0.8	$2 \cdot 10^{-6}$
2016 [144]	3901	6.39	1130	164^{+28}_{-25}	$34.9^{+6.3}_{-5.4}$	$3.9^{+0.7}_{-0.6}$	7.92σ

assuming any particular Earth model. The χ^2 includes period-dependent parameters describing the uncertainties of the reactor $\overline{\nu_e}$ spectrum, the energy scale, the event rate, and the energy-dependent detection efficiency; all these parameters are constrained. The overall reactor rate uncertainties for Period 1, and Periods 2 and 3 are 3.5% and 4.0%, respectively. Systematic uncertainties are conservatively treated as being fully correlated across all data-taking periods. Finally, a penalty term provides an optional constraint on the neutrino oscillation parameters by using solar, accelerator, and short-baseline reactor antineutrino experiments.

The best-fit to the unbinned data with free N(U) and N(Th) yields N(U) = 116 and N(Th) = 8 geoneutrino events from U and Th, respectively. The corresponding fluxes are $\Phi(U) = N(U) \times 2.01 \times 10^4 = 2.33 \times 10^6$ and $\Phi(Th) = N(Th) \times 6.88 \times 10^4$ = 0.55×10^6, both measured in cm^{-2} s^{-1}. The joint confidence intervals for the sum N(U)+N(Th) and the asymmetry factor $\frac{N(U)-N(Th)}{N(U)+N(Th)}$ agrees with the expectation from the geological reference model of Enomoto et al. [175]. Assuming the chondritic Th/U mass ratio of 3.9, the total number of U and Th geoneutrino events is N(U+Th) = 116^{+28}_{-27}, corresponding to the electron antineutrino flux $\Phi(U+Th) = (3.4 \pm 0.8) \times 10^6$ cm^{-2} s^{-1} at the KamLAND location or to the all-flavours total antineutrino flux of $(6.2 \pm 1.5) \times 10^6$ cm^{-2} s^{-1}.

The latest results of KamLAND were presented in 2016 [144]. The analysed data set included a ~3.5-year-period with few reactors operated, and ~2-year live-time with all Japanese reactors switched off. The number of detected geoneutrinos, 164^{+28}_{-25} events, is measured with the 17% uncertainty in agreement with expectation. The evidence of the geoneutrino signal achieves 7.9σ. It is confirmed that an excess of events observed by some reactor experiments in the 4–6 MeV range (see Section 5.2) has no impact on the geoneutrino results. The effect of the reactor spectrum uncertainty is much smaller than the statistical uncertainty of the geoneutrino signal.

6.2.4. Future

KamLAND continues data acquisition in its KamLAND-Zen phase with the Japanese nuclear reactors switched off, detecting about 14 geoneutrino events per year. The latest results were presented at the end of 2016, and the data from at least three more years are available for the analysis. The construction of a new, cleaner inner balloon is envisaged to meet the needs of the neutrinoless double beta decay search. For the same purpose, techniques to increase the light yield are studied. The possible improvements include: increasing the geometric coverage using Winston cones for light collection, installing higher quantum efficiency 20″ PMTs instead of the older ones masked to 17″, and using new LAB-based LS with better transparency [176]. The estimated increase of the light yield is factor 1.8, 1.9 and 1.4 for each of the improvements, respectively, or factor 4.5 in total. These measures should further improve the sensitivity of KamLAND to geoneutrinos, helping to discriminate the backgrounds and to increase the IBD detection efficiency.

6.3. Extracting Th/U global mass ratio

The Th/U mass ratio plays an important role in the Earth geoscience. It is important for the understanding of the early Earth evolution. The distributions of U and Th could be also used as benchmark for estimating the distribution of other refractory lithophile elements. Refractory elements are condensed from the nebula at high temperatures, and are assumed to be accreted in chondritic proportions, with limited variability in their ratio. The decay sequences of the both elements stops at different lead isotopes, and the Th/U mass ratio in a sample can be evaluated based on measured ^{232}Th/^{238}U molar values and their time integrated Pb isotopic values. The detailed analysis of the available data was recently performed by Wipperfurth et al. [68], the authors obtained high precision planetary Th/U mass ratio of 3.876 ± 0.016. The geoneutrinos can provide the independent check of the validity of the underlying assumptions, since the proportion of the Th and U contribution to the total spectrum reflects the global Th/U mass ratio, given the local contribution is known.

The theoretical (for ideal detector with infinite resolution) IBD spectra from the U and Th chains with the assumption of secular equilibrium in the chains and at the chondritic ratio of Th/U masses M(Th)/(U) = 3.9 are shown in Fig. 8. The visible difference in the spectra makes contributions from U and Th potentially distinguishable, but the low-energy part of the U spectrum has a contribution very similar to the Th spectrum. In fact, the end-point for the Th spectrum (E$_0$ =
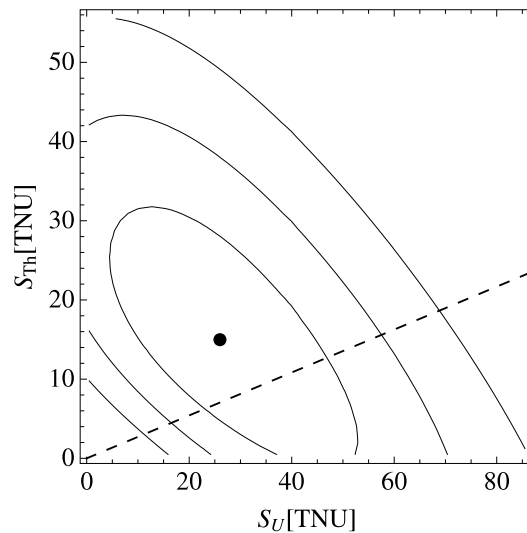
Fig. 17. Best-fit contours corresponding to 1, 2 and 3σ obtained by the unbinned likelihood fit with both the U and Th signals left free parameters. The dashed line corresponds to the chondritic Th/U mass ratio.
Source: Figure from [143].

2.252 MeV from ^{212}Bi β-decay with 64% branching ratio) is practically the same as the end-point of the ^{234}Pa^m β-decay ($E_0 = 2.267$ MeV with branching $\sim$100%). The difference above 2.267 MeV is due to β−decay of ^{214}Bi to the ground state with a branching of $\sim$19%. The fraction of events in the ^{238}U chain spectrum above the E = 2.267 MeV point is about 0.5 of the total U signal. Considering that the expected signal from the ^{238}U is a factor of $\sim$3.5 higher for chondritic M(Th)/M(U) = 3.9, a simple statistical estimate shows that in the absence of other backgrounds, the uncertainty of the S(Th)/S(U) ratio will be a factor of 5 higher compared to the statistical uncertainty of the number of the detected geoneutrino events.

Dye in [177] estimated number of events needed to distinguish between different Th/U mass ratios. The estimated number of events needed to obtain absolute uncertainty of 0.1 (this would translate to 2.5% uncertainty for the chondritic M(Th)/M(U) ratio) on the M(Th)/M(U) exceeds 10^5, the non-realistic statistics for the modern detectors. With more realistic statistics of 10^3 geoneutrino events one can expect the absolute uncertainty of the order of 1 (or 25% of the chondritic ratio) on the Th/U mass ratio.

A fit with the U and Th normalizations left as free parameters was performed by the Borexino collaboration in [143]. The U and Th best-fit contributions are shown in Fig. 17. The obtained contours indicate a non-zero U signal at a confidence level slightly above 1σ, and the Th contribution is still compatible with the zero signal. The amount of geoneutrino events observed in Borexino until now ($\sim$25) does not leave a chance to obtain a reasonable estimate for the M(Th)/M(U), as its expected uncertainty is approaching 100% even in the absence of reactor antineutrinos.

KamLAND obtained an upper limit on the Th/U mass ratio < 19 (90% C.L.) in [172], indicating the separation of the U and Th antineutrino signals. The analysis was updated using $\sim$2.5 years more data acquired after all Japanese reactors were switched off [144]. For the first time the positive indication of the U signal at 3.44σ C.L. in the fit with a free Th/U mass ratio was reported. Also, the first "global" Th/U mass ratio measurement M(Th)/M(U) = $4.1^{+5.3}_{-3.3}$ was obtained with the upper limit for the mass ratio of Th/U improved to < 17.0 at 90% C.L. All the values are consistent with the chondrite data and the BSE models. It is the first Th/U mass ratio measurement which is not compatible with zero at the 1σ level. The M(Th)/M(U) ratio obtained by KamLAND with $\sim$160 geoneutrino events is weaker compared to the simple estimate presented above because of the presence of backgrounds in the experimental data. Japanese nuclear plants

6.4. Obtaining radiogenic heat from the measured geoneutrino signal

The total radiogenic heat is proportional to the total mass of U and Th in the Earth. In contrast, as follows from formula (10), the measured geoneutrino signal depends not only on the total mass of U and Th but also on their distribution throughout the Earth. The uncertainty in HPEs distribution translates into an uncertainty in the distribution of energy sources in the Earth. Therefore, the measured geoneutrino fluxes do not provide a unique measure of the heat production and can correspond to a range of heat power depending on the distribution of HPEs.

Due to the fact that the distribution of HPEs in the crust is relatively well-studied, the variety of models is mainly defined by the distribution of HPEs in the mantle. The extreme values for the same amount of heating material can be obtained assuming either a uniform distribution of U and Th throughout the mantle or a layered one.

For fixed amount of uranium in the mantle, the minimal geoneutrino signal from the mantle would be produced by a thin uranium layer at the bottom of the mantle (sunken-layer hypothesis). The maximum geoneutrino signal corresponds
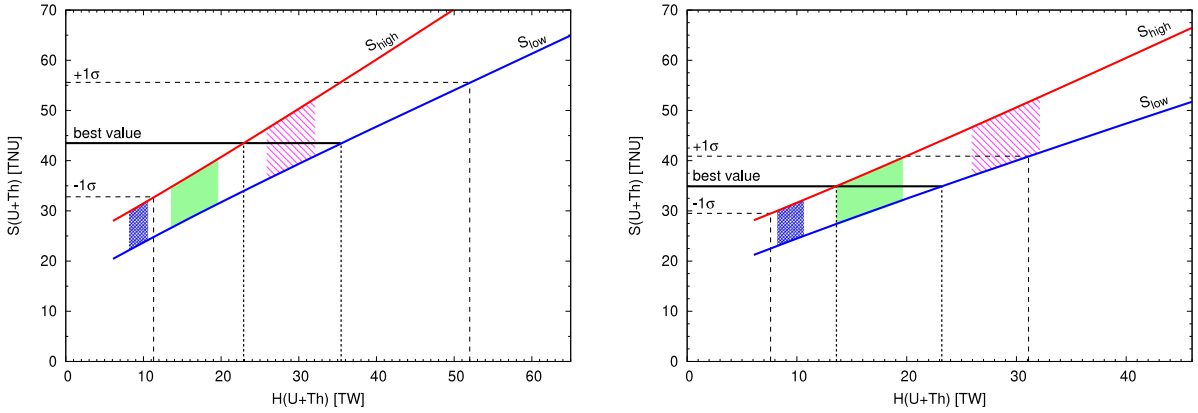
Fig. 18. The expected geoneutrino signal from U and Th in Borexino (left) and KamLAND (right) as a function of radiogenic heat released in radioactive decays of these chains [143]. Three filled regions correspond, from the left to the right, to the cosmochemical, geochemical, and geodynamical BSE models. Best experimental values from Borexino and KamLAND, together with 1σ errors, are reported in corresponding plots (Figures generously provided by Fabio Mantovani).

to the uniform distribution of the same amount of uranium in the mantle (homogeneous hypothesis). These two extreme cases give respectively the mantle signal from uranium $S_M^{min} = 11.3 \times M(U)$ and $S_M^{max} = 16.2 \times M(U)$ TNU [129].

The geoneutrino contributions from the crust and the mantle can be combined to obtain predictions of the surface geoneutrino flux for the known amount of HPEs, or, equivalently, for a fixed heat flow. The U and Th in the crust should correspond to the observational values, and the rest of the U and Th within the values given by the BSE model is assigned to the mantle. The highest geoneutrino signal is modelled by assigning the maximum acceptable value to the crust and distributing the remaining fraction uniformly through the mantle. The lowest geoneutrino signal is obtained in a similar way, assigning the minimum value compatible with observations to the crust and distributing the remaining fraction in a thin layer at the bottom of the mantle. The total amount of radioactive elements is constrained by the measured heat flow 47 ± 2 TW. Reaching this limit would correspond to a fully radiogenic Earth model. On the other hand, the minimal geoneutrinos signal is obtained with the minimal possible mass of U and Th in the crust and a negligible amount in the mantle.

In this way, the two extreme total signals, S_{high} and S_{low}, expected at the chosen site for a given heat flow H(U+Th) can be obtained. In the plot Signal vs. Heat the corresponding lines will bound the range of corresponding allowed values for geoneutrino signal and heat. The plot of is site dependent, though the slope of lines is universal.

In Fig. 18 the expected geoneutrino signal in Borexino (left) and KamLAND (right) are shown as a function of the produced radiogenic heat. The upper (red in the colour print) and lower (blue) lines correspond to the high and low models, respectively. The error in the prediction of the crustal signal is taken into account, and so are the different U and Th distributions through the mantle, as described above. Three filled areas in Fig. 18 represent three classes of BSE models, based on the heat values from the classification by Šrámek et al. [36]: 11 ± 2 TW, 20 ± 4 TW, and 33 ± 3 TW for the cosmochemical, geochemical and geodynamical estimates, respectively. The horizontal lines represent the results of Borexino of 2015 [143] and the latest result of KamLAND [144], respectively. The Borexino results are compatible with all BSE models within 1σ, while the KamLAND measurements are compatible with all models within 2σ, slightly disfavouring the more energetic cosmochemical ones.

The radiogenic heat production for the sum of U and Th corresponding to the central value of the Borexino data fit is in the range 23–36 TW, and 13–23 TW for the KamLAND. Considering the 1σ interval and the minimum and maximum models, the 68% C.L. interval for H(U+Th) radiogenic heat covers 11–52 TW range for Borexino. Assuming the chondritic ratio for M(Th)/M(U) and M(K)/M(U) = 10^4, the total measured terrestrial radiogenic power is restricted from the Borexino data to H(U+Th+K) = 33^{+28}_{-20} TW at 68% C.L., to be compared with the global terrestrial power output of 47 ± 2 TW. The KamLAND constraints for the radiogenic heat are more stringent, H(U+Th) is in the interval 8–31 TW at 68% C.L., see Fig. 18.

6.5. Mantle signal

The measurement of the geoneutrino signal from the mantle is a clue to distinguish between the existing models (see 3.3). Both the Borexino and KamLAND collaboration provided estimations of the mantle signal based on the total measured signal and the predictions for the crust signal. Because of the dominating contribution from the crust in both locations and the low available statistics, the differential measurement has a high uncertainty.
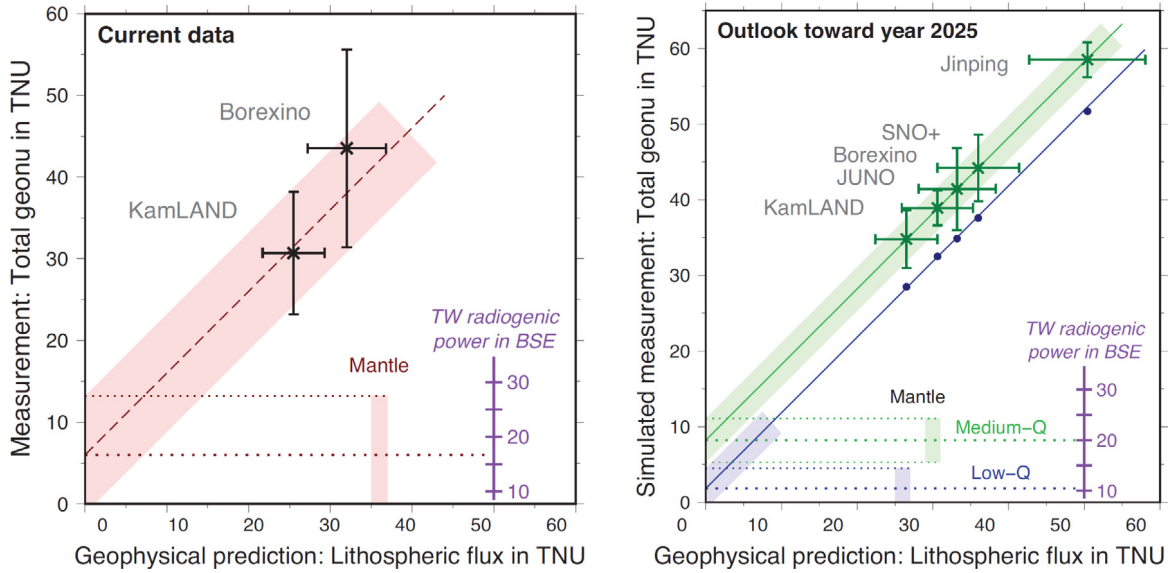
Fig. 19. *Left*: measured geoneutrino signal in Borexino and KamLAND (2013 measurement) versus geological predictions of the lithospheric flux. **Right:** expected geoneutrino signals in existing (extrapolated to 2025) and future detectors versus geological predictions of the lithospheric flux. *Source:* Figure from Šrámek et al. [33], reproduced under Creative Commons Attribution 4.0 International License [34].

In Borexino the contribution to the total geoneutrino signal from the local crust (LOC) $S_{geo}^{LOC} = (9.7 \pm 1.3)$ TNU was estimated by Fiorentini et al. [178],[18] while the contribution from the rest of the crust (ROC) is $S_{geo}^{ROC} = (13.7 \pm 2.8)$ TNU according to Huang et al. [24], and the total signal from the crust is $S_{geo}^{Crust} = (23.4 \pm 2.8)$ TNU,[19] corresponding to the average predicted number of events from the crust $N_{geo}^{Crust} = 12.75 \pm 1.53$ events. Using the experimental likelihood profile for the N_{geo} and assuming the Gaussian distribution of the N_{geo}^{Crust} uncertainty and Poissonian statistics for the number of detected events, one can obtain the 68% C.L. interval for the signal from the crust in Borexino, which corresponds to 5.8–19.6 events with the maximum at 11.4 events. Recalculated in the TNU, it is $S(Mantle) = 20.9_{-10.3}^{+15.1}$ TNU. The probability of observing at least one event from the mantle is 98% [143].

In Fig. 19 the measured geoneutrino signal in Borexino and KamLAND is plotted versus the geological predictions of the lithospheric flux. In accordance with Šrámek et al. [33], analyses of the existing data (KamLAND and Borexino combined) give a result with a large uncertainty on the mantle flux, 6.0 ± 7.2 TNU[20] (left plot in Fig. 19).

Future detectors will provide more opportunities for the mantle signal separation. SNO+ in Sudbury (Canada) will soon start taking data. Another detector sensitive to the geoneutrino, JUNO, is under construction in the Jiangmen laboratory in Southern China. The mantle signal at Jiangmen is a relatively small fraction ($\sim$14%) of the total geoneutrino signal, but a combination of the JUNO measurement with those of other experiments will allow extracting the mantle contribution. Fig. 19 (from Šrámek et al. [33]) demonstrates the underlying principle. The measured geoneutrino flux is plotted versus the geological estimate of the flux from the lithosphere that does not include the contribution from the convecting mantle. As a result, a best-fit line with a slope of 1 will intersect the physics input axis at the point corresponding to the mantle contribution. The mantle signal is reasonably assumed to be the same for all the considered locations. The range of possible interceptions provides the total uncertainty that includes both the uncertainties of the measurements and the uncertainty of the lithospheric flux predictions.

In order to extract statistically significant information on the mantle contribution from the measured total signal, a more accurate estimation of the geoneutrino flux from the local area at each site is required. For this purpose a broad collaboration of particle physicists earth scientists is necessary, joining their efforts to provide surveys and descriptions of the geology, seismology, heat flow, and geochemistry of the regional lithosphere.

---

[18] In this paper a first attempt to extract the mantle signal from the combined analysis of the first high significance Borexino and KamLAND data was performed.

[19] Fiorentini et al. [178] reported separate values for U and Th, $S(U) = 7.81 \pm 1.00$ TNU and $S(Th) = 1.86 \pm 0.27$ TNU, obtained using $\langle P_{ee} \rangle = 0.55$. The uncertainties are summed assuming fully correlated U and Th contributions, and the total signal from the LOC is $S_{LOC} = 9.7 \pm 1.3$ TNU. The best value of the ROC is reported by Huang et al. [24], in the row FFC (for Far Field Crust, another term used for the ROC) of Table 2, $S(U) = 10.3_{-2.2}^{+2.6}$ TNU and $S(Th) = 3.2_{-0.7}^{+1.1}$ TNU. The total signal is $S(U+Th) = 13.7_{-2.3}^{+2.8}$ TNU with the central value of $S(U+Th)$ not equal to $S(U) + S(Th)$ because of the sum of the two non-symmetric distributions. In the Borexino paper [143] the highest value of the uncertainty was considered, $S(U+Th) = 13.7 \pm 2.8$ TNU. Since the two components ROC and LOC are uncorrelated, the central values are summed and the uncertainties are propagated in quadrature, resulting in $S_{Crust} = 23.4 \pm 2.8$ TNU [179].

[20] The analysis in [33] does not include the 2016 results of KamLAND [144].

6.6. Search for the hypothetical geo-reactor

The nuclear reactor at the Earth's core was theoreticized by Herndon [180]. Hollenbach and Herndon [181] showed that a planetary-scale nuclear reactor could operate over the lifetime of the Earth. The theory requires some U and Th sink to the core instead of accumulating in the crust rising from the early molten Earth as a slag. The proto-Earth geo-reactor hypothesis has been recently reassessed by Degueldre and Fiorina [182]. They found its build-up and subsequent operations unlikely. Nevertheless, there is no experimental evidence against the hypothesis. The natural nuclear reactor would explain the peculiarities in the isotopic content of the Earth, in particular the observed high ^{3}He/^{4}He ratio found in volcanic hotspot lavas, like those erupted at Hawaii and Iceland, which is up to 50 times the present atmospheric ratio. The geo-reactor would explain the ratio in a natural way as ^{3}He would be a product of tritium decay in reactor. As discussed by Raghavan [183], this hypothetical source in the thermal power range of 1 to 10 TW could be the power source driving the deep Earth plumes and the Earth's geo-dynamo mechanism responsible for the Earth's magnetic field. Hypotheses for presently existing natural breeder reactors propose deep-earth locations, including the centre of the core [180], the inner core boundary [184], and the core–mantle boundary [185]. Herndon notes in [186] that if a nuclear fission reactor should occur in those places, then geo-reactors would anyway melt down to the Earth's centre.

The KamLAND data were used to test the hypothesis of a natural nuclear reactor in the Earth's core assuming its stable power output over the data-taking period and ^{235}U: ^{238}U = 0.75:0.25 composition. The modelled contribution from the reactor was allowed to vary in the fit together with contributions from U and Th geoneutrinos. The oscillation parameters were constrained from the solar, accelerator, and reactor antineutrino data. The limits on the geological reactor power were obtained from the fit, < 3.1 TW at 90% C.L. (or < 3.7 TW at 95% C.L.) [172], improving the previous results.

A geo-reactor with two dominant fission nuclides ^{235}U (76%) and ^{238}U (23%) composition (as discussed by Herndon and Edgerley [187]) was excluded by Borexino using the same likelihood fit as for the geoneutrino analysis with the fixed mass ratio M(Th)/M(U) = 3.9, adding the simulated geo-reactor spectrum in the fit. The number of reactor events N_R was constrained to the expected value of $N_R = 33 \pm 2.4$ events. The upper limit on the geo-reactor power is 4.5 TW at 95% C.L. [158], close to the one obtained by KamLAND.

Dye [188] discussed a method for the geo-reactor detection by analysing the characteristic oscillation pattern in its energy spectrum. Indeed, if the geometrical size of the natural reactor is small compared to the length of oscillations and the distance to the detector is fixed, the geo-reactor energy spectra should demonstrate oscillation patterns. Characteristics of this distorted spectrum could reveal the distance to the geo-reactor with an uncertainty of ~150 km, and using estimates from several Earth-surface sites locate a solitary geo-reactor by triangulation, discriminate the models, and provide precision power measurement. The method to locate an electron antineutrino source by measuring spectral distortions utilizes the Rayleigh test. This statistical test returns the power of spectral distortions for an assumed length of the neutrino path. The amplitude of distortions depends on the energy resolution; hence, the future high resolution JUNO detector (see 8.2) will have advantages when applying the method. The exposure necessary to locate a geo-reactor at the centre of the Earth (6371 km), close to the inner core boundary (5149 km), and at the core–mantle boundary (2981 km) with the probability of 95% using the JUNO type detector (3%/$\sqrt{E}$ energy resolution and $\sim 10^{33}$ target protons) is found to be 20, 6, and 0.4 10^{33} protons·yr for 1 TW reactor, respectively.

7. New detection methods

Antineutrino detection with IBD detectors has clear advantages: the LS is cheap allowing construction of detectors with target media large enough for detection of antineutrinos, the main antineutrino background comes from reactors and can be reduced by choosing locations far away from the operating nuclear reactors; moreover, the reactor energy spectra are well-understood and predictable. Unfortunately, the high energy threshold of the IBD on protons makes impossible the detection of geoneutrinos from the third most important contributor to the geoneutrino spectra, ^{40}K. That is why physicists are looking for detection methods with a threshold below the ^{40}K end-point energy.

Some recent proposals are concerned with the directionality. The methods are based either on the modification of the IBD detectors (sectioning or doping with ^{6}Li) with the purpose of improving the angular sensitivity or on the application of other known detection techniques, e.g., gas-filled TPC. The latter uses antineutrino-electron scattering and suffers from the strong irreducible background from the solar neutrinos that are both much more numerous and have a factor of ~6 higher interaction cross sections in the region of interest.

7.1. Directionality of the geoneutrino signal

Directional measurement of the antineutrino events would provide additional information that can be used to disentangle geoneutrinos from isotropic background and reactor antineutrinos whose points of origin are known. Moreover, it could help separating crust and mantle components in the total geoneutrino flux. Simple model calculations of the angular distribution of the antineutrinos originating in the crust, mantle, and hypothetically in the core of the Earth are shown in Fig. 20. Uniform distribution of HPEs in the 40 km crust, mantle, and core is assumed in calculations. The area under first two curves is normalized to unity, and the core distribution is reduced by a factor 3 for the sake of better visual presentation. It can be seen that while the angular distribution of crustal geoneutrinos concentrates close to the
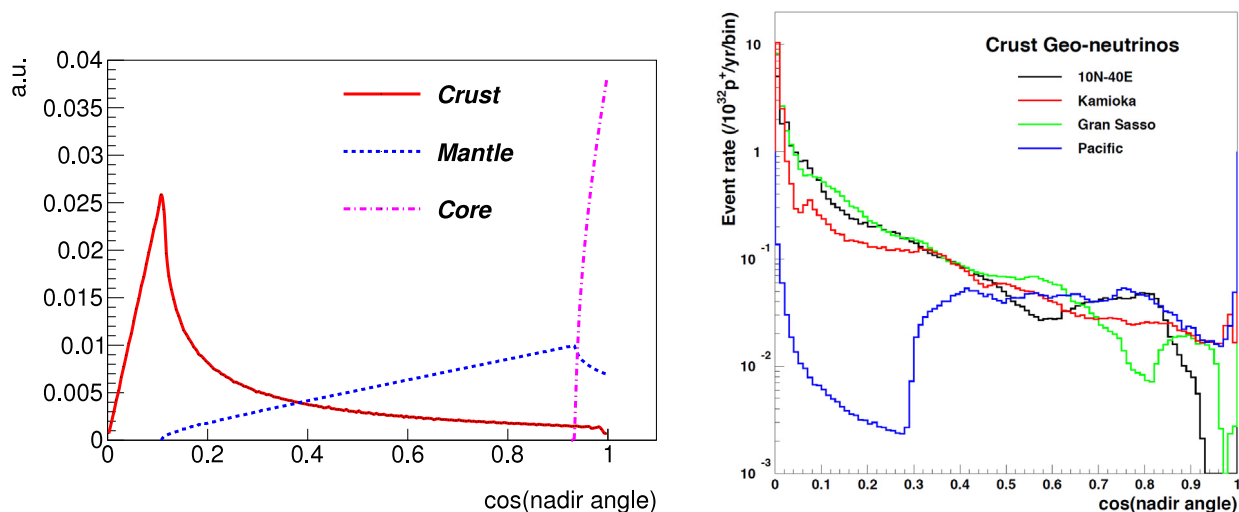
Fig. 20. Left: zenith angle distributions of geoneutrinos produced in the uniform crust (red), mantle (blue) and core (magenta) calculated in a simplified model with uniform distribution of heating elements. **Right**: predicted zenith angle distributions of crustal geoneutrinos at some geographic positions.
Source: (Figure from [49].

horizon, the angular distribution of mantle geoneutrinos spreads over a range of angles below, and the hypothetical core contribution is expectedly concentrated close to vertical. In general, because about 25% of the signal arrives from the distances comparable to the crust thickness, one should expect the same fraction of the signal to be distributed almost uniformly for the continental crust. The "ideal" crust distribution peaks at the direction of tangent to the mantle from the observation point, in this direction the line of sight is longest. For the thickness of the uniform crust of 40 km, this point corresponds to $\cos\theta \sim 0.09$. As shown in [189] the rise of the angular distribution is linear before this point. For the uniform crust the peak would thus give the position of the inner edge [189]. The peak in the crust angular distribution corresponds to the maximum possible nadir angle from the mantle, the feature is clearly visible in the mantle angular distribution. The angular distribution for the core would concentrate at the vertical direction, with minimum $\cos\theta$ about 0.94. The corresponding peak in the mantle distribution is expected at this value, indicating the corresponding boundary.

The peak at small angles expected for the uniform approximation does not appear in more detailed calculations, see left plot in Fig. 20. The crust is not uniform, the highest abundances of HPEs are expected in the upper crust and sediments, and the "horizontal" signals from the thin upper layer, especially in the near field, dominate in the distribution [190].

The absence of U and Th in the core is generally assumed, but there exists experimental evidence that potassium can form alloys with iron [191,192], and so the possibility that the Earth's core might contain significant amounts of ^{40}K is not completely excluded. Nimmo et al. [193] argued that along with other explanation the presence of the potassium in the core at the level ~400 ppm would satisfy the present-day inner core size, surface heat flux, mantle temperature and cooling rate, and positive core entropy production.

Sensitivity to the mantle geoneutrino signal at the continental sites is masked by a much stronger signal from the crust, as at least 75% of the flux come from the crust. Measurements with deep underwater detectors on the seafloor where the crustal contribution is minimal, as proposed by Dye et al. [194], would be a straightforward solution, but practical realization of the proposal is problematic. Exploiting the geoneutrino directionality would be a good alternative to measuring far away from continents. This could be achieved with a directional detector capable of resolving the angular distribution of incoming antineutrinos. Determining the direction of the incoming geoneutrino was considered just after the first report of KamLAND on geoneutrinos by Fields et al. [189] and Suzuki [195].

Calculations using the detailed topographic information show that the distribution of geoneutrino signals demonstrate detectable anisotropy not only in the nadir angle but also in the azimuthal one. Calculations of azimuthal anisotropy of incoming geoneutrinos were performed by Šrámek et al. [33]. As one can see in Fig. 21, all existing sites but SNO demonstrate significant azimuthal anisotropy due to the vicinity either to the thicker crustal structures (Jinping) or to the thinner oceanic crust (JUNO, KamLAND).

If measured, the angular distribution of geoneutrinos can be inverted to give tomography of the terrestrial radioisotope distribution [189].

7.2. Directionality in IBD reaction in liquid scintillator

Because the only experimental data on geoneutrinos acquired thus far are collected with IBD detectors, it will be natural to examine their angular sensitivity more closely. In fact, displacement of neutrons in the direction of
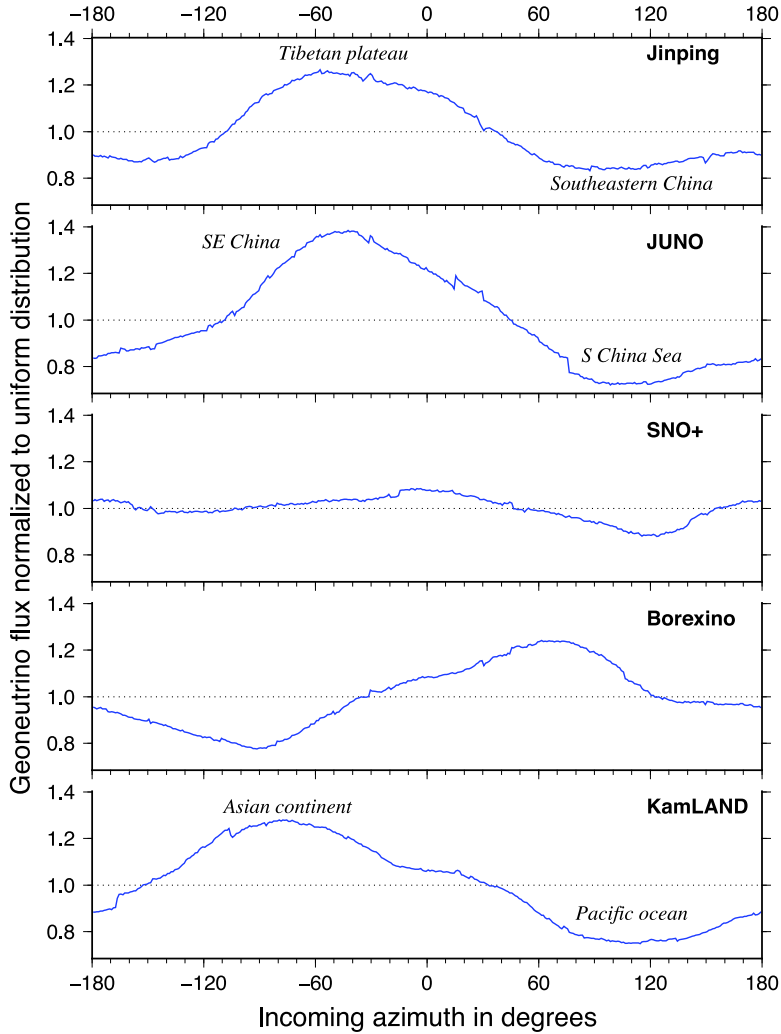
Fig. 21. Predicted signal at 5 laboratories as a function of azimuth of incoming geoneutrino. Signal in each bin is shown with respect to the one expected in a case of uniform distribution at the corresponding detector.
Source: Figure from Šrámek et al. [33], reproduced under Creative Commons Attribution 4.0 International License [34].

incoming antineutrinos was observed in reactor experiments: the Gösgen, Bugey, and Palo Verde collaborations registered neutron displacement for segmented scintillator detectors by detecting the neutron in a segment farther away from the reactor with respect to the segment where the positron was observed. The unsegmented CHOOZ experiment reported measurement of the average neutron–positron separation and determination of the incoming antineutrino direction with an uncertainty of 18° (half-aperture of a cone) at the 68% C.L. with 2700 events statistics [196].

Using the results of Vogel and Beacom [84,85], one can evaluate the total cross section as well as the positron angular distribution. As a rule, the positron angular distribution is not detectable in IBD experiments. However, the angular distribution of the recoil neutrons is accessible. Since in the laboratory system the proton is at rest, the neutron is initially emitted at a forward angle with a maximum at

$$\cos\theta_n = \frac{\sqrt{2E_\nu(m_n - m_p) - ((m_n - m_p)^2 - m_e^2)}}{E_\nu}. \tag{50}$$

At the IBD threshold the neutron emission direction is exactly forward, and at the reactor antineutrino energies (below 10 MeV) it is still mainly in the forward direction. The average angle $\overline{\cos\theta_n}$ is naturally closer to unity than its maximum value defined by (50).

The basic idea of the directional studies is to search for the statistical displacement of the neutron with respect to the prompt event ($\overrightarrow{\Delta R} = \overrightarrow{R_{prompt}} - \overrightarrow{R_{delayed}}$). The displacement of the emitted positron is negligible and cannot provide any reasonable information regarding the direction of the incoming antineutrino. In contrast, the neutron is emitted in a

relatively narrow range of angles (within ∼55 degrees [197]) around the direction of the antineutrino with energies up to 100 keV for reactor antineutrinos. The emitted neutron is slowed down in the proton-rich media. The average angle in a single collision is $\overline{\cos\theta_n} = \frac{2}{3A}$. In scattering on protons (atomic number A = 1) it is possible for the neutron to preserve directionality. The slowdown occurs very quickly, and the displacement from the production point is determined by the first few scatterings, still preserving the initial direction. The later isotropic diffusion process does not change the average displacement, which, in the case of CHOOZ, was observed to be 1.7 cm.

The position of the event can be reconstructed in liquid scintillation detectors with a typical precision of 10–15 cm. The single 2.2 MeV γ from the neutron capture has a comparable mean free path, adding uncertainty to the reconstructed point of origin, as it can travel up to 1 metre away. Also, the prompt event is not a point-like energy deposit, as it is a composition of the energy deposit of the positron kinetic energy and the 511 keV gammas from the positron annihilation. The 511 keV gammas are emitted in opposite directions, and thus the centre of gravity of the deposited energy should, in general, coincide with position of the event, though some additional uncertainties to the position reconstruction of the parent event will be added. Simulations show that the typical displacement of two reconstructed vertices of the IBD pair of events is ∼1.5 cm in the organic scintillator, much lower than the value that can be detected for a single event. Assuming large sample of the events, a statistical analysis is possible. As a naïve estimation, with 100 events one can expect 1σ sensitivity to this displacement with 15 cm vertex reconstruction precision. Due to the fact that much larger datasets are accumulated with antineutrino reactor experiments, detection of the displacement does not look impossible.

Feasibility of the directionality technique was studied by Batygov using Monte-Carlo simulations of a large volume IBD detector [197]. MC predicts a statistically measurable delayed signal displacement in the direction of the incident antineutrino, making directionality studies with unloaded liquid scintillation detectors possible. As expected, the effect is small compared to the natural spread of the reconstructed signals. Obtaining a statistically significant result would require thousands of antineutrino events even for the simplest case of a point-like antineutrino source. For KamLAND-sized detectors this implies unrealistic run times of hundreds of years. A larger detector placed near the operating reactors may provide enough statistics within a reasonable time. Similar conclusions were obtained in another study by Domogatski et al. [198]. The authors state that information obtained with one 30-kt target mass unloaded liquid scintillation detector using directional separation of the incoming geoneutrino flux is useful but limited. More definite information could be obtained only with a much larger detector.

To solve the problem of low statistics, two methods were discussed in [197]. A bigger, as large as 100-kt, unloaded liquid scintillation detector should collect enough events for simple terrestrial antineutrino directionality studies in several years, provided the vertex reconstruction accuracy is not worse than that in KamLAND and the background is low enough. Another improvement can be achieved by minimizing the spatial spread of the delayed event with specially chosen LS loading. Loading the LS with ^{6}Li will provide a ^{3}H+α delayed signal instead of a single gamma from the neutron capture on the proton. The loaded LS should offer about two to four times better statistical efficiency of incident angle determination compared to unloaded scintillators. In order to take full advantage of the method, high vertex reconstruction quality is needed, which is especially important in this case. Simulations show that directional studies are highly affected by the presence of backgrounds. Thus, special care should be taken to avoid backgrounds, including the reactor background and internal contamination.

The idea of doping the LS with ^{6}Li has been recently considered more thoroughly by Tanaka and Watanabe [199]. They studied the resolving power of a ^{6}Li loaded liquid scintillation detector for the detection of a hypothetical magma chamber under the Hida Mountains located in the northern Japanese Alps. The estimated size of the magma chamber is ∼16000 km^3. Assuming the average U and Th concentrations equal to the surface values (5 ppm and 20 ppm), it can be estimated that the expected contribution of the magma chamber to the antineutrino flux is ∼10% of the entire geoneutrino flux expected at the KamLAND detector, namely 2.0 TNU and 1.6 TNU from the U and Th decays, respectively, versus total of 38.5 ± 7.7 TNU. Simulations show that a 3-kt detector located at the KamLAND site can separate the magma chamber contribution from the total geoneutrino flux at a 3σ confidence level in 10 years. The technique is applicable to resolving crust contributions from the mantle, as well as neutrinographic imaging of the Earth's interior. Šrámek et al. [36] estimated that the flux contribution from two large low shear velocity provinces (LLSVPs) is comparable to the flux contribution from the hypothetical magma chamber. Such excess fluxes can be imaged with these directionally sensitive techniques.

A modification of existing antineutrino detection techniques based on IBD and, according to the authors, better suited for directional studies was proposed by Safdi and Suerfu [200]. They suggest using segmented detector with separate target and capture planes, calling it SANTA (segmented antineutrino tomography apparatus). The neutrons in this detector are captured in the thicker boron-loaded layers. The location of the IBD event and the momentum of the positron are determined by tracking the positron's trajectory through the detector. The method's capability was demonstrated through MC simulations. The use of the SANTA technique for the geoneutrino detection will necessarily demand a lot of physical space. A kilotonne scale SANTA for the geoneutrino detection consisting of a stack of 1000 modules with 10 × 10 m cross-section and 1 cm thick would stretch for around 1 km, making the practical application of the technique for the geoneutrino study questionable.

While practical directionality measurement is impossible with existing detectors, including KamLAND, the scientific significance of such research would justify construction of detectors better suited for this purpose.

7.3. Water based IBD detectors

Water is an inexpensive proton-rich medium that would be of a great benefit in constructing extra-large geoneutrino detectors. Pure water is used in large volume (50 kt) Čerenkov detector Super-Kamiokande [201] to study the high-energy portion of the solar neutrino spectrum. The detector registers electrons scattered by solar neutrinos. Directionality of the Čerenkov light is used to suppress backgrounds. Due to the low light yield, the energy threshold in water Čerenkov detectors is typically too high (above 3.5 MeV) to detect correlated pairs of events caused by geoneutrinos. An advanced study of neutron tagging in a water Čerenkov detector was reported by the Super-Kamiokande collaboration [202]. The tagging efficiencies of thermal neutrons was evaluated in the 0.2% $GdCl_3$-water solution and in pure water. They were determined to be 66.7% and 20%, respectively, for events above 3 MeV with the corresponding background probabilities of 2×10^{-4} and 3×10^{-2}. This is still not enough to challenge the detection of antineutrino events in the energy range of interest for the geoneutrino studies.

The amount of light produced by Čerenkov radiation is 50 times lower than in liquid scintillators, and a significant fraction of light is emitted in the UV region, where water loses transparency and PMTs are not sensitive. Adding a wavelength shifter to water helps to register photons otherwise invisible to PMTs, increasing the amount of detected light by a factor of 2–3 [203,204]. These studies were aimed at improving the sensitivity of existing water Čerenkov detectors, but not for the geoneutrino studies. Adding chemicals to water can reduce transparency, which influences the sensitivity.

A more promising approach to using water-based liquid scintillator (WbLS) has recently been discussed by Alonso et al. [205]. WbLS is a novel scintillation medium for large liquid detectors, in which scintillating organic molecules and water are co-mixed using surfactants [206]. The possible mixture extends from pure water to pure scintillator, offering a great possibility of tuning the detection media to fit the physics programme. Compounds with a low content of LS will work in a regime close to that of the water Čerenkov detectors, but offering higher light yield. In contrast, liquid scintillator detectors with the addition of water will gain directionality and metal-loading capability. A variety of solvents are available. In addition, different wavelength shifters and other additives can be used to adjust the timing properties of the final mixture.

The development of WbLS with a low attenuation length will allow the construction of large-volume multipurpose detectors, suitable for the geoneutrino studies.

7.4. IBD and resonant electron capture on other nuclear targets

IBD and resonant electron capture on other nuclear targets in view of the geoneutrino detection were discussed in early papers [8,9]. A list of possible nuclear targets can be found in Table 2 of the seminal article by Krauss et al. [9]. In general, the majority of considered targets will need huge quantities of material, orders of magnitude larger than those needed for detectors exploiting IBD of protons, to provide a comparable counting rate. The lowest energy threshold of 1.041 MeV is provided by a ^{3}He target. This would allow the detection of antineutrinos from ^{40}K. Unfortunately, the necessary amount of ^{3}He is beyond modern capabilities.

The use of a low-threshold target isotope ^{106}Cd for antineutrino detection, not listed by Krauss et al. in [8], was proposed by Zuber [207].[21] The natural abundance of ^{106}Cd is very low, 1.25%, and enrichment will be needed. The ^{106}Cd isotope is one of the most suitable nuclei to search for the double beta plus processes having a high-energy release in the decay. It is also favoured for the possible resonant $0\nu2\epsilon$ transitions to excited levels of ^{106}Pd. Serious efforts are applied in order to develop large-scale set-ups for the neutrinoless double-beta decay searches. A cadmium- tungstate ($CdWO_4$) solid state 215 g detector with an enrichment of 66% in ^{106}Cd is available for tests [209]. It was developed within the framework of the collaboration between the DAMA and INR-Kiev groups. $CdWO_4$ is a high density (7.9 g/cm^3), high atomic number scintillator. It emits light at a wavelength of 475 nm and has a total light yield of about 15 photons/keV. The decay time was found to be ~15 μs for different source energies. The possibility of using $CdWO_4$ crystals to construct both segmented and unsegmented detectors is being analysed. The decay time can be shifted to the nanosecond timescale using dopants during crystal production. A fast scintillator can be used to reconstruct the vertex of the events [210]. There are currently two other experiments in progress searching for the double beta decay of ^{106}Cd: the TGV-2 experiment in the Modane underground laboratory in France utilizing 32 planar HPGe detectors with 16 thin foils of enriched ^{106}Cd (23.2 g) installed between the detectors [211], and the COBRA experiment, using an array of CdZnTe semiconductors (~380 g of natural Cd) at the Gran Sasso underground laboratory [212]. COBRA is intended for a large-scale experiment with a total source mass of about 400 kg of CdZnTe enriched in another "double-beta" isotope ^{116}Cd to about 90%.

The detection reaction is IBD on cadmium

$$\overline{\nu_e} + {}^{106}\mathrm{Cd} \rightarrow {}^{106}\mathrm{Ag} + e^+. \tag{51}$$

The energy threshold of the reaction is 1.216 MeV, below the end-point of the ^{40}K β-spectrum (1.311 MeV). The full positron energy is in the 1.02 – 1.12 MeV energy range. Two transitions are possible: the $0^+ \rightarrow 1^+$ allowed transition to the ground state or the $0^+ \rightarrow 6^+$ transition to the first excited state (89.66 keV).

---

[21] The use of the isotope for geoneutrino detection was first discussed by Chen [208].
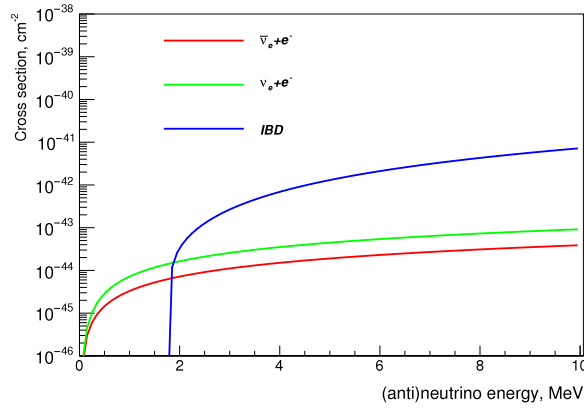
Fig. 22. Neutrino cross sections for three detection reactions: elastic scattering of neutrino and antineutrino off electrons with no energy threshold, and antineutrino interactions on protons (IBD reaction) with 1.8 MeV threshold.

The unstable silver isotope ^{106}Ag decays into the stable palladium ^{106}Pd with a half-life of 24 min through two concurrent processes. In 41% of cases it decays through electron capture (EC) "invisible" to the detector

$$^{106}\text{Ag} + e^- \rightarrow {}^{106}\text{Pd} + \nu_e, \tag{52}$$

and in 59% of cases it undergoes β^+-decay

$$^{106}\text{Ag} \rightarrow {}^{106}\text{Pd} + e^+ + \nu_e. \tag{53}$$

The β^+ end-point energy is E_0 = 1.943 MeV in 82.9% of all transitions, and it is E_0 = 1.431 MeV accompanied by a 0.5119 MeV gamma from the first excited state (16.3% of all transitions). The pair of 511 keV gammas from the annihilated positron emitted in IBD of cadmium to silver and followed by another couple of 511 keV gammas produced by ^{106}Ag β^+-decay provides a tag for the antineutrino events. The clear disadvantage of this method is a large delay between these two correlated events corresponding to a 24 min half-life of ^{106}Ag. But at the same time, the spatial separation is extremely small. Therefore, the spatial coincidence can be used to reject the background.

7.5. Other detection methods

There is no energy threshold for the elastic antineutrino scattering process

$$\overline{\nu_e} + e^- \rightarrow \overline{\nu_e} + e^-, \tag{54}$$

potentially providing sensitivity to the low energy portion of the geoneutrino spectra. The elastic scattering of neutrinos on electrons was successfully used in water Čerenkov (SuperKamiokaNDE, SNO) and liquid scintillator detectors (Borexino) to detect solar neutrinos. The cross section of the elastic antineutrino scattering is 2–3 times lower compared to the neutrino scattering (see Fig. 22) and the flux of geoneutrinos is 2–4 orders of magnitude lower compared to that of solar neutrinos. Thus, the use of this process for the geoneutrino studies is challenging. The directionality of the scattered electron offers a potential opportunity to suppress the neutrino background. The method is successfully used in water Čerenkov detectors at higher energies.

A technique with a certain potential for application to directionality studies was considered by Aberle et al. [213]. The authors propose to use directional Čerenkov light in LS to reconstruct the direction of electrons. Light with a wavelength shorter than ∼370 nm is absorbed and re-emitted isotropically, making this fraction indistinguishable from scintillation. Čerenkov photons, on average, arrive earlier with respect to the scintillation light, the latter being affected by chromatic dispersion and the finite time of the scintillation processes. A Geant4 simulation of a spherical detector with the radius of 6.5 m with scintillator properties matching a KamLAND-like scintillator showed that the early light could be effectively separated, if photodetectors with the transit time spread of 0.1 ns are used. This can be further improved if more red-sensitive photodetectors or scintillators with narrower emission spectra are used. The algorithms developed for water Čerenkov detectors were able to converge on reasonable reconstructed vertices and directions for the simulated energies of electrons of 5 MeV, 2.1 MeV, and 1.4 MeV relevant for the neutrinoless double beta decay search. At lower energies the reconstructed vertex is wider by ∼1 cm. Though the authors do not consider the geoneutrino detection as one of the potential tasks, the technique, in principle, can be used in elastic scattering experiments with energies above the Čerenkov limit. The directionality in this case is needed to separate the geoneutrino events from the much higher irreducible background induced by solar neutrinos.

A method for measuring the geoneutrino flux from ^{40}K by using antineutrino-electron elastic scattering was recently considered by Leyton et al. [214]. Gas-filled time projection chambers (TPCs) are discussed in this work as a detector
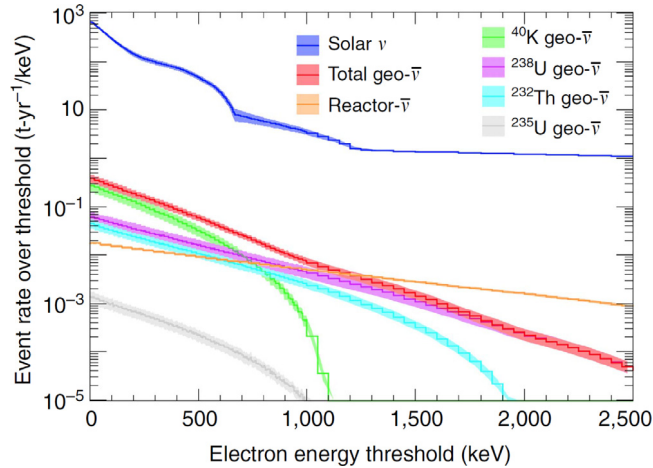
Fig. 23. Event rates over threshold shown versus electron energy threshold for solar neutrino (upper curve, blue), geoneutrino (below the solar one at lower energies, red) and reactor antineutrino (below the solar one at higher energies, orange) events, assuming a CF_4 target and 55% survival probability. Individual contributions to the total geo-neutrino flux are visible below the total geoneutrino signal: from ^{40}K (ends at $\sim$1.1 MeV, green), ^{238}U (coincides with total geoneutrino signal above 2.5 MeV, violet), ^{232}Th (ends at $\sim$1.9 MeV teal), and ^{235}U (ends at $\sim$1 MeV, grey) are also shown. *Source:* Figure from Leyton et al. [214], reproduced under Creative Commons Attribution 4.0 International License [34].

meeting the necessary requirements on the backgrounds and directional sensitivity. The challenge of the method is shown in Fig. 23, the expected geoneutrino signal is two orders of magnitude below the irreducible background from the solar neutrino elastic scattering. Detector resolution, efficiency, and energy thresholds assumed in the estimations are based on the performance of other successful detectors [215,216]. In particular, the MUNU collaboration [215] used a 1 m^3 TPC filled with CF_4 at 1 bar for searches of the antineutrino magnetic moment exactly in the energy range relevant for the geoneutrino studies. The energy resolution was determined to be 10% at 200 keV and 6.8% at 478 keV. The TPC demonstrated good angular resolution for recoil electrons, namely 15° at 200 keV, 12° at 400 keV, and 10° at 600 keV. The exposures needed to access ^{40}K, mantle, and core geoneutrinos at 95% C.L. are 140 tonne-years, 2.6 ktonne-years, and 200 ktonne-years, respectively. Enhancing the angular resolution of the detector results in a significant reduction in the required exposures.

A gas-filled TPC large enough for antineutrino searches would have an enormous size. The weight of 1 m^3 of the CF_4 gas at normal conditions is about 4 kg. Leyton et al. [214] consider high-pressure time projection chambers operating at pressures up to 10–15 bar as a better solution, noting the trade-off between the necessary mass and degradation of the angular sensitivity due to multiple scattering at higher pressures. Assuming a CF_4 (or Xe) target operating at 10 bar, a 15-tonne detector will have a FV of 403 (260) m^3 corresponding to a cube of 7.4 (6.4) m on one side.

8. Upcoming experiments and new projects

At present only two detectors, Borexino and KamLAND, are taking data. Soon, the SNO+ experiment will join the pool of the geoneutrino detectors, and JUNO is under construction. Below we discuss the potential of SNO+ and JUNO and review other existing proposals.

8.1. SNO+

SNO+ is the successor to the SNO experiment at SNOLAB in Sudbury, Ontario, Canada. The project was initiated in 2005. Significant efforts have been undertaken to transform the heavy water detector into a large volume liquid scintillator detector. The main goal of this multipurpose neutrino experiment is a search for neutrinoless double beta decay in ^{130}Te, but SNO+ also aims to study low-energy solar neutrinos, and geo and reactor antineutrinos.

SNO+ started filling with liquid scintillator on October 25, 2018 [217]. This experiment should be the third to provide geoneutrino results following the first studies by KamLAND and Borexino.

SNO+ reuses the existing infrastructure of SNO, including a 6-m-radius acrylic vessel (AV) surrounded by 9394 inward-facing PMTs mounted on a concentric stainless steel support structure with a radius of 8 m. The AV will be filled with the LS and surrounded with ultra-pure water shielding. The depth of the SNO+ detector site is 6010 m.w.e., providing effective shielding against backgrounds induced by cosmic muons. As few as 70 muons a day are expected. For comparison, in Borexino there are 4000 muons a day for a smaller detector. The centre of the detector is 2039 m below the surface, and the surface is 309 m above sea level. In contrast to the Borexino and KamLAND experiments, SNO+ does not have an external tank. Water fills the space between the cave walls and the AV.

SNO+ will use 780 tonnes of linear-alkylbenzene (LAB) based LS, well-suited for electron antineutrino detection. The LAB scintillator formula can be roughly considered as $C_{18}H_{30}$, with the 0.86 g/cm^3 density. MC simulations of the amount of light collected in SNO+ yield 1200 PEs per MeV of energy deposited, as a result of high geometric coverage (54%) and high light yield of undiluted LAB [218]. 780 t of LAB contain 7.34×10^{31} target protons. The predicted geoneutrino signal at the SNO+ location is around 40 TNU. The event rate in SNO+ would thus be around 29 events per year compared to ~32 events from the distant nuclear reactors in the same energy range.

The SNO+ detector is located in a region of a thick continental crust. The crust and the local geology in the vicinity of SNO+ were extensively studied since this is a mining location. Huang et al. [105] constructed a detailed 3D model of the regional crust by using geological, geophysical, and geochemical information. The model includes six 2×2 degrees tiles centred at the location of the SNO lab, and spreading by 3 tiles in latitude and 2 longitude. Crustal cross sections obtained from seismic surveys were used to characterize the crust and assign uncertainties to its structure. The average continental crust depth in the studied area is 42.3 ± 2.6 km. The geological structure of the upper crust was reconstructed on the basis of regional geology. The abundances of U and Th and their uncertainties in each upper crustal lithologic unit were determined directly from analyses of representative samples. The average chemical compositions of the middle and lower crust were obtained using global compilation of the chemical compositions of the corresponding rocks. The total regional crust contribution to the geoneutrino signal at SNO+ is predicted to be $15.6^{+5.3}_{-3.4}$ TNU with the Huronian Supergroup near SNO+ dominantly contributing to the uncertainty $7.3^{+5.0}_{-3.0}$ TNU. This is a glacial layer rich in uranium and thorium deposited with variable thickness throughout the region. The presence of the strongly contributing geological feature nearby would require further study to decrease its contribution to the uncertainty of the geoneutrino signal. The bulk crustal geoneutrino signal at SNO+ was estimated by Huang et al. [105] to be $30.7^{+6.0}_{-4.2}$ TNU. The total geoneutrino signal at SNO+ is predicted to be 40^{+6}_{-4} TNU without accounting for uncertainties of the signal from the continental lithospheric mantle and the convecting mantle. The geoneutrino signal from the crust predicted by the global-scale reference model [41] based on the average composition of the global upper continental crust was higher, $34.0^{+4.0}_{-5.7}$ TNU, as commented in [105]. This is due to the fact that Archean to Proterozoic Canadian Shield has lower U and Th concentrations. Local heat flow measurements revealed ~25% higher heat flow than the average for the entire Canadian Shield [219]. The higher heat flux is very likely correlated to higher local uranium and thorium abundances and thus can be related to the conclusions by Huang et al. [105]. The surface sediment layer may be a significant contributor.

More recent estimates come from Strati et al. [220]. A combination of geological observations, extensive geochemical sampling, and geophysical surveys was used to create a coherent 3D geological model of a 50×50 km upper crustal region surrounding SNOLAB. A 3D numerical model of U and Th distribution predicts a contribution of $7.7^{+7.7}_{-3.0}$ TNU out of the crustal geoneutrino signal of $31.1^{+8.0}_{-4.5}$ TNU. The uncertainties of the local contributions are even larger than those estimated by Huang et al. [105]. The large uncertainty of the local crust geoneutrino signal restricts SNO's capability of discriminating among different BSE compositional models of the mantle, and a more detailed geophysical characterization of the 3D structure of the heterogeneous Huronian Supergroup is needed.

The SNO+ programme includes solar neutrino studies, which are very demanding from the point of view of the internal backgrounds. This automatically guarantees the radiopurity levels required for the geoneutrino studies. Cosmic muon fluxes will be reduced by an order of magnitude compared to Borexino. The total interaction rate for electron antineutrinos by the world's nuclear power reactors is estimated at 129 events per 1 year of exposure. Roughly 1/4 of this rate occurs in the same energy range as the geoneutrinos, and the signal-to-background ratio for geoneutrinos in SNO+ will be approximately 1:1. In summary, the design characteristics of the SNO+ detector before the double-beta phase (with the pure scintillator) are favourable from the point of view of backgrounds for the geoneutrino detection. In the Te-loaded phase the low energy backgrounds are expected to be about 50–150 times higher than in the pure scintillator phase, which can make the extraction of the geoneutrino signal more difficult [221].

The SNO+ sensitivity to the total geoneutrino flux is expected to be dominated by statistical uncertainties with an accuracy close to that of Borexino for similar data-taking periods. The larger volume of the SNO+ detector compensates for the higher reactor background rate [221]. The antineutrino flux from the reactors will be affected by the planned upgrades when different reactor cores will be turned off, which will result in an expected total flux reduction below 10% at each moment. The known time evolution of the reactor power provides additional help in separating this background [221]. The antineutrino spectrum from reactors at SNO+ was estimated by Baldoncini et al. [222]. The results of the calculations are presented in Fig. 24.

At the first step, the analysis with the global Th/U mass ratio fixed according to standard geological models is planned. The effect of local variations of the ratio is being studied. In further analysis SNO+ aims to separate both the uranium and thorium contributions and the mantle and crust contributions in a global analysis of the geoneutrino spectrum including the KamLAND and Borexino data [221].

8.2. JUNO

JUNO is a multipurpose neutrino oscillation experiment. The first of the third generation of reactor antineutrino experiments, it is designed to determine the neutrino mass hierarchy and to measure the neutrino oscillation parameters with a greatly increased precision. One of the declared goals of the experiment is the geoneutrino flux measurement. The start of the data acquisition is planned for 2021.
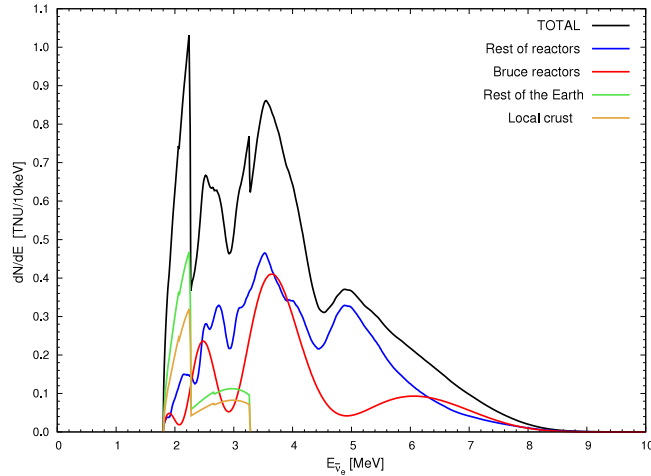
Fig. 24. Antineutrino energy spectra expected at SNO+ as estimated by Baldoncini et al. [222]. The geoneutrino spectrum components are shown separately: the contribution of the local crust (smaller contribution, orange) and the rest of the Earth (larger contribution, green). The reactor antineutrino spectrum is separated in two parts to underline the contribution from the closest (240 km) Bruce power station reactors (strongly oscillating lower spectrum, red), and the contribution from the rest of the reactors (less oscillating middle spectrum, blue). The sum of reactor and the geoneutrino components provides the total antineutrino spectrum (the resulting highest spectrum, black).

The Jiangmen Underground Neutrino Observatory is located in Kaiping, Jiangmen, Guangdong province in Southern China. The position of the detector, equally distant ($\sim$53 km) from two nuclear power plants (Yangjiang and Taishan nuclear power plants, NPPs), was optimized in view of the primary goal of the neutrino mass hierarchy determination. The large mass of the detector (20 kt) and strong requirements on the LS radiopurity and energy resolution (3% at 1 MeV) are also dictated by this goal.

The JUNO project was approved by the Chinese Academy of Sciences in February 2013. Six reactor cores of Yangjiang NPP, each with the thermal power (TP) of 2.9 GW, will run in 2020, before the start of the data acquisition in JUNO. The Taishan NPP is planned to operate four cores of 4.59 GW(TP) each. The total TP of the Yangjiang and Taishan NPPs will be 35.73 GW. It is possible that the last two cores in Taishan will not operate by 2021; in that case the total power would be 26.55 GW(TP) at JUNO's start-up. A run with reduced power would be very useful for the geoneutrino studies.

The JUNO detector will be located underground at a depth of 700 m, providing protection against cosmic rays comparable to that of the KamLAND site. The surrounding rock is granite with the average density of 2.66 g/cm^3 along a 650 m bore hole. The activities of U, Th, and ^{40}K in the rock around the experimental hall are measured to be 130, 113, and 1062 Bq/kg, respectively. The JUNO detector consists of a 20 kt central liquid scintillator detector contained in an acrylic tank immersed in a water pool. 17 000 20-in. PMTs installed on a stainless steel sphere and facing the LS will provide optical coverage larger than 75%. A muon tracker will be installed on top of the detector. The water pool is equipped with PMTs to detect the Čerenkov light from cosmogenic muons and thus also serves as an active muon veto [223].

A high energy resolution in the energy spectrum is extremely important for resolving the neutrino mass hierarchy, which will also be an advantage in the geoneutrino analysis. The designed energy resolution is the highest among the state-of-the-art detectors, such as BOREXINO or KamLAND. To prevent energy resolution degradation, the Earth's magnetic field of about 0.5 Gs at the experimental site will be compensated by a specially designed set of coils surrounding the water pool and ensuring proper operation of the PMTs, which, due to their size, are extremely sensitive to magnetic fields. The LAB is chosen as a detection medium due to its excellent transparency, high flash point, low chemical reactivity, and good light yield. The LS contains 3 g/l of PPO serving as the fluor and 15 mg/l p-bis-(o-methylstyryl)-benzene (bis-MSB) as the wavelength shifter. An attenuation length larger than 25 m at 430 nm after the proper purification is reported for the mixture [224].

The same as at the other locations, at the JUNO site 50% of the total geoneutrino signal is provided by the closest $\sim$500 km of the Earth, see Fig. 5. The three-dimensional global reference model of Huang et al. [24] was used to estimate the signal from lithospheric geoneutrinos at the JUNO site. Two main sources of uncertainties are the physical structure of the lithosphere and the abundances of HPEs in the reservoirs. The expected geoneutrino signals at JUNO from the global Bulk Crust and from the Continental Lithospheric Mantle are $28.2^{+5.2}_{-4.5}$ TNU and $2.1^{+2.9}_{-1.3}$ TNU respectively [130]. The distributions of U and Th abundances are log-normal, the quoted central values are medians, and the errors are asymmetric. The adopted mantle model divided into two spherically symmetric domains (Depleted Mantle and Enriched Mantle), refers to the McDonough and Sun's BSE model [18] based on a primitive mantle having U and Th masses M(U) = 8.1×10^{16} kg and M(Th) = 33×10^{16} kg, respectively. The mantle contribution in JUNO is estimated to be $\sim$9 TNU [130]. The total expected geoneutrino signal is $39.7^{+6.5}_{-5.2}$ TNU [130]. The present crustal models are affected by uncertainties, which are comparable to the mantle contribution [130].

Similar to that of SNO+, the JUNO physics programme includes solar neutrino studies. The demands on the LS radiopurity for the solar neutrino programme are an order of magnitude stronger than for the antineutrino one [109]. The radiopurity levels necessary for the antineutrino programme (10 ppt in U and Th in acrylic and 10^{-15} g/g in the LS) would also be well suited for the geoneutrino studies. The cosmic muon fluxes are comparable to the ones at the KamLAND site, and the general antineutrino selection will provide a clear set of antineutrino data. The most serious source of uncertainties in the geoneutrino studies will come from the strong reactor background, and, in particular, from the uncertainties of the reactor spectrum shapes at low energies.

All of the contributions from nuclear cores operating worldwide in 2013 were found to provide $95.3^{+2.6}_{-2.4}$ TNU by Baldoncini et al. [128]. The contributions of the future Taishan and Yangjiang nuclear power plants are estimated on the basis of the following parameters: 80% antineutrino detection efficiency, FV with 17.2 m radial cut (18.35 kt of LS corresponding to 1.285×10^{33} free protons), 35.8 GW(TP) and 53 km baseline for each core in the Taishan and Yangjiang power plants [225]. The uncertainties on the predicted reactor antineutrino signal are estimated to be ∼5.6%, including the effect of uncertainties on the neutrino oscillation parameters, which can be further reduced after the JUNO measurement of the neutrino oscillation parameters. The expected total reactor antineutrino rate is 16100 ± 900 events per year [76] (1569 ± 88 TNU), with the dominating contribution from Taishan and Yangjiang (>90%) to the total reactor antineutrino signal. About 1/4 of the events occurs in the geoneutrino energy window (351 ± 27 TNU in $E_{\bar{\nu}_e} < 3.27$ MeV), making it difficult to extract the geoneutrino signal, which is almost an order of magnitude lower.

Non-antineutrino backgrounds were studied by Han et al. [76]. The expected rates of the accidental and cosmogenic (^{7}Li and ^{8}He) backgrounds are comparable with the expected geoneutrino rate, but only a relatively small fraction of the corresponding background spectra falls into the geoneutrino energy window. The test of JUNO geoneutrino sensitivity in [76] is based on the fit of a large set of simulated spectra constructed by combining a random set of the initial signal and backgrounds. The spectral fit is repeated 10 000 times for the statistics corresponding to 1, 3, 5, and 10 years of full lifetime after cuts. The precision of the geoneutrino measurement with a Th/U mass ratio fixed at the chondritic value was found to be 13%, 8%, 6%, and 5%, respectively, if the uncertainty of the reactor spectrum is ∼1%. Indeed, the theoretical study by Hayes et al. [118] shows that reactor antineutrino spectra have at least a 4% theoretical uncertainty, which would be difficult to reduce within a purely theoretical framework. Thus, a near detector discussed by Forero et al. [226] as a necessary tool for the neutrino mass hierarchy study[22] would also be extremely useful to solve the issue of the reactor spectrum precision.

Reguzzoni et al. [228] used gravimetric data to improve the quality of the crustal geoneutrino signal prediction in JUNO. The gravimetric data are from the Gravity field and the steady-state Ocean Circulation Explorer (GOCE) mission [229]. The model is built by inverting gravimetric data over the $6° \times 4°$ area centred at the JUNO location. In contrast to the existing global models, the GOCE Inversion for Geoneutrinos at JUNO (GIGJ) provides a site-specific subdivision of the crustal layer masses. The local rearrangement of the crustal layer thicknesses results in a ∼21% reduction and a ∼24% increase of the middle and lower crust expected geoneutrino signal, respectively. Correspondingly, the uncertainties of the geoneutrino signal predictions at JUNO induced by uncertainties in the uranium and thorium abundances in the upper, middle, and lower crust are reduced by 77%, 55%, and 78%.

The ∼10% precision of the geoneutrino signal measurement is expected within 3 years of data taking, if the precise description of the low energy portion of the reactor spectrum will be available, where a ∼1% precision level is needed. The same set of data will allow measurement of the U contribution with a 20% precision and Th contribution with a 30% precision [109], i.e., for the first time a reasonable experimental constraint of the global Th/U ratio can be provided (see left plot in Fig. 25).

The possibility of extracting the mantle signal from the JUNO data will strongly depend on the precision of the predictions of the local crust contribution. Two probable scenarios are shown in the right plot in Fig. 25. As discussed in Section 6.5, a combination of the JUNO measurement with those of other experiments will allow the mantle contribution to be extracted from the global geoneutrino measurements (see Fig. 19).

## 8.3. Jinping underground laboratory

The Jinping Neutrino Experiment is a proposed neutrino observatory for low-energy neutrino physics in the China JinPing Laboratory (CJPL) [230], the most suited site for low background experiments due to its 2400 m depth under the Jinping Mountain in Sichuan province. The experimental site is located in a long tunnel at least 950 km away from the NPPs in operation and under construction. The Jinping Neutrino Experiment collaboration plans to build two detectors filled with LS or slow (water-based) LS as a neutrino target and detection material that will detect antineutrino events through the IBD of the protons. The design mass of each of the two detectors is 1.5 kt [77]. The slow LS candidates for MeV-scale neutrino experiments at Jinping were considered by Guo et al. [231]. A 1-t-scale prototype detector is under development [232].

Preliminary sensitivity studies for the Jinping detector based on assessments of the site and potential detector designs were conducted [28]. The muon rate at Jinping is as low as $(2.0 \pm 0.4) \times 10^{-10}$ cm^{-2} s^{-1} with 6720 m.w.e. rock overburden greatly suppressing the corresponding backgrounds.

The predicted geoneutrino signal is 59.4 ± 6.8 TNU with an expected background from nuclear reactors of only 6.7 ± 0.1 TNU in the geoneutrino energy range [77].

---

[22] In a more recent study by Danielson et al. [227] it is argued that there is no need for the near detector from the point of view of the neutrino mass hierarchy measurement; nevertheless, the near detector will still be needed for the robust geoneutrino signal measurement.
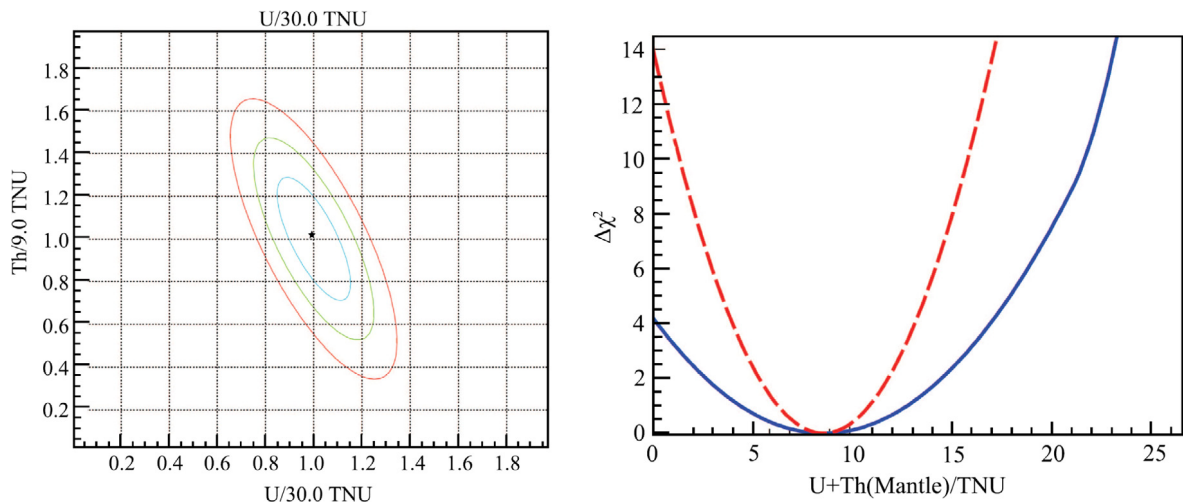
Fig. 25. left: estimate of JUNO's sensitivity to the Th/U mass ratio presented as 1, 2 and 3σ contours for the free Th/U mass ratio fit of the model data corresponding to 10 years of JUNO detector running **right:** estimate of the possibility of separating the mantle contribution from the total signal presented as a χ^2 profile. The flatter profile (blue) corresponds to the crust signal prediction with the 18% uncertainty, and the narrower profile corresponds to a better knowledge of the crust contribution with the 8% uncertainty.
Source: Figure from [76].

8.4. Other projects

LENA (Low Energy Neutrino Astronomy) was a project of 50 kt deep underground multipurpose liquid scintillator detector [233] with a vast physics programme far beyond the one of its progenitor 50 kt Borex detector (see Fig. 26, left). A cylindrical shape 30 × 100 m of the LS container was considered in the project. Due to its size, LENA would have had a moderate LY of 240 PEs/MeV. Two possible locations for the experiment have been considered: at the Pyhäsalmi site the expected geoneutrino signal is 51.3 ± 7.1 TNU, while at the Fréjus site it is 41.4 ± 5.6 TNU. In both cases, a detailed analysis of the contribution from the local crust surrounding the detector would be important in order to further constrain the expected signal and to better interpret the measured signal. LENA would detect about 1000 geoneutrino events per year. The main antineutrino background, namely that from the nuclear power plants, would be several times lower in the Finland location: this would make it a preferable location from the point of view of the geoneutrino measurement. In the geoneutrino energy window, the expected reactor antineutrino signal would be about 20 to 37 TNU depending on the construction of several new power plants in Finland, while it would be about 145 TNU at Fréjus, as estimated on the basis of the thermal power of NPPs as reported in 2009.

Another possible site for the geoneutrino exploration is the Baksan Neutrino Observatory (BNO) in Russia. The geographic position of the observatory far away from operating nuclear power plants provides for the geoneutrino studies the environment free of the reactor antineutrinos. A multipurpose 10 kt liquid scintillation detector is being discussed [234]. The predicted geoneutrino signal is 52.6 TNU with expected background from nuclear reactors of only 14.4 TNU in the geoneutrino energy range.

Hanohano is a project of a 10 kt-scale liquid scintillation detector to be placed 3–5 km underwater [235,236]. It should be a portable device deployed from the barge (see Fig. 26, right), and it is intended for measuring the mantle contribution to the total geoneutrino signal. Its location far away from the continental crust will guarantee the overwhelming contribution from the mantle. About 100 geoneutrino events per year are expected. The combination of the data from multiple sites and the data from an oceanic experiment would provide valuable information for measuring the mantle contribution.

Conclusions

The Borexino and KamLAND experiments acquired about 190 IBD events from the geologically produced antineutrinos. These experiments demonstrated the presence of the radiogenic component in the Earth's heat flux and the capacity to directly assess the amount and distribution of Th and U inside the Earth. The observations of geoneutrinos are consistent with expectations, but the accumulated data set is still too small to draw conclusions regarding the Earth's models. Additional exposure from existing and upcoming experiments will provide further improvement. The mantle signal separation could be enhanced by refinements of the predicted local crust flux. In addition to testing the models of the BSE, the geoneutrino can be used to assess the compositional nature of large structures in the deep mantle.

The detection of the ^{40}K contribution is still beyond the capabilities of modern detectors. New techniques with a lower threshold and/or directional sensitivity are needed to observe this signal.
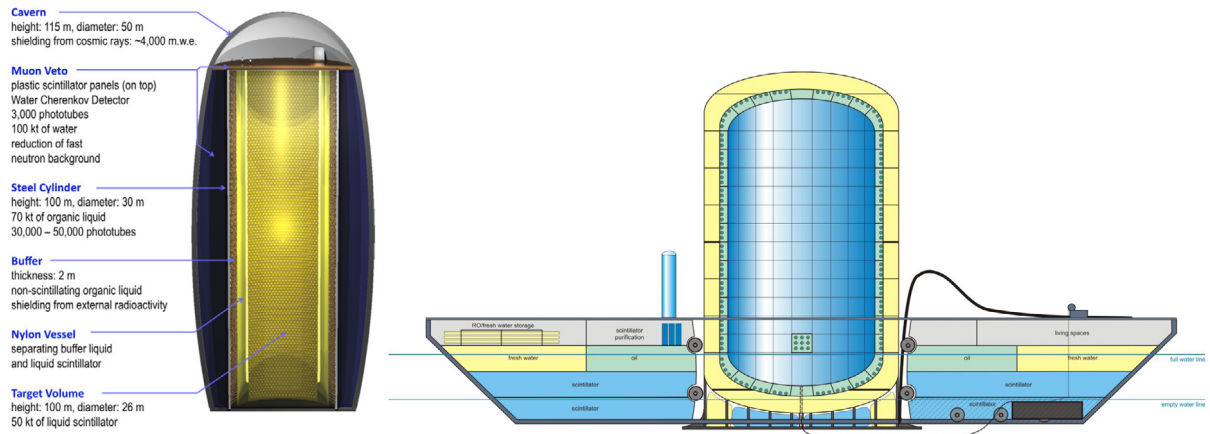
Fig. 26. LENA (Fig. from [233]) and HANOHANO concepts (Fig. from [235]).

Acknowledgements

References

[1] J. Joly, Radioactivity and Geology, an Account of the Influence of Radioactive Energy on Terrestrial History, D. van Nostrand, NY, 1909.
[2] C.L. Cowan Jr., F. Reines, F.B. Harrison, H.W. Kruse, A.D. McGuire, Science 124 (1956) 103.
[3] G. Fiorentini, M. Lissia, F. Mantovani, Phys. Rep. 453 (2007) 117.
[4] G. Marx, N. Menyhárd, Commun. Konkoly Obs. 48 (1960) 1.
[5] M. Markov, Neutrino, Nauka, Moscow, 1964.
[6] G. Eder, Nuclear Phys. 78 (1966) 657.
[7] G. Marx, Czech. J. Phys. 19 (1969) 1471.
[8] L.M. Krauss, S.L. Glashow, D.N. Shramm, Nature 310 (1984) 191.
[9] M. Kobayashi, Y. Fukao, Geophy. Res. Lett. 18 (1991) 633.
[10] R.S. Raghavan, et al., Phys. Rev. Lett. 80 (1998) 635.
[11] R.S. Raghavan, S. Pakvasa, Phys. Lett. D 37 (1988) 849.
[12] C.G. Rothschild, M. Chen, F.P. Calaprice, Geophys. Res. Lett. 25 (1998) 1083.
[13] T. Araki, et al., KamLAND collaboration, Nature 436 (2005) 499.
[14] G. Bellini, et al., Borexino collaboration, Phys. Lett. B 687 (2010) 299.
[15] http://www-nds.iaea.org/nsdl/.
[16] H. Leutz, G. Schulz, H. Wenninger, Z. Phys. 187 (1965) 151.
[17] X. Mougeot, Phys. Rev. C 91 (2015) 055504.
[18] W.F. McDonough, S. Sun, Chem. Geol. 120 (1995) 223.
[19] S. Enomoto, Earth Moon Planets 99 (2006) 131.
[20] C. Jupart, S. Labrosse, F. Lucazeau, J.-C. Mareschal, Treatise on Geophysics, Vol. 7, second ed., Elsevier, Oxford, 2015, p. 223.
[21] J.H. Davies, D.R. Davies, Solid Earth 1 (2010) 24.
[22] J. Korenaga, Rev. Geophys. 46 (2008) RG2007.
[23] U.R. Christensen, J. Geophys. Res. 90 (1985) 2995.
[24] Y. Huang, V. Chubakov, F. Mantovani, R.L. Rudnick, W.F. McDonough, Geochem. Geophys. Geosyst. 14 (2013) 2003.
[25] J.-C. Mareschal, C. Jaupart, C. Phaneuf, C. Perry, J. Geodyn. 54 (2012) 43.
[26] S.T. Petcov, M. Piai, Phys. Lett. B 533 (2002) 94.
[27] F. Capozzi, et al., Phys. Lett. D 95 (2017) 096014.
[28] L. Wan, G. Hussain, Z. Wang, S. Chen, Phys. Lett. D 95 (2017) 053001.
[29] K.A. Olive, Chin. Phys. C 40 (2016) 100001.
[30] S.T. Dye, Rev. Geophys. 50 (2012) 3007.
[31] S. Enomoto, Neutrino Geophysics and Observation of Geo-Neutrinos at KamLAND (Ph.D. Thesis), Tohoku University, Japan, 2005.
[32] C. Giunti, C. Kim, M. Monteno, Nucl. Phys. B 521 (1998) 3.
[33] O. Šrámek, et al., Sci. Rep. 6 (2016) 33034.
[34] https://creativecommons.org/licenses/by/4.0/.
[35] A.M. Dziewonski, D.L. Anderson, Phys. Earth Planet. Inter. 25 (1981) 297.
[36] O. Šrámek, W.F. McDonough, E.S. Kite, V. Lekić, S.T. Dye, S. Zhong, Earth Planet. Sci. Lett. 361 (2013) 356.
[37] G. Laske, G. Masters, Z. Ma, M. Pasyanos, Geophys. Res. Abstr. 15 (2013) Abstract EGU2013-2658.
[38] M.E. Pasyanos, T.G. Masters, G. Laske, Z. Ma, J. Geophys. Res. 119 (2014) 2153.
[39] W.D. Mooney, G. Laske, T.G. Masters, J. Geophys. Res. 103 (1998) 727.

[40] C. Bassin, G. Laske, G. Masters, EOS Trans. AGU 81 (2000) 897.
[41] F. Mantovani, L. Carmignani, G. Fiorentini, M. Lissia, Phys. Lett. D 69 (2004) 1.
[42] J.-C. Mareschal, C. Jaupart, L. Iarotsky, Neutrino Geoscience. Chapter: 4, Open Academic Press, 2016.
[43] H.-C. Nataf, Y. Richard, Phys. Earth Planet. Inter. 95 (1996) 101.
[44] O. Čadek, Z. Martinec, Stud. Geophys. Geodyn. 35 (1991) 151.
[45] S.T. Dye, Sci. Lett. 297 (2010) 1.
[46] M. Coltorti, et al., Geochim. Cosmochim. Acta 75 (2011) 2271.
[47] E. Garnero, A. McNamara, Science 320 (2008) 626.
[48] B. Roskovec, O. Šrámek, W.F. McDonough, arXiv:1810.10914, 2018.
[49] S.T. Dye, Y. Huang, V. Lekić, W.F. McDonough, O. Šrámek, Phys. Proc. 61 (2015) 310.
[50] W.F. McDonough, W. F, Deep Earth: Physics and Chemistry of the Lower Mantle and Core, Wiley, American Geophysical Union, 2016, p. 145.
[51] M. Javoy, Geophys. Res. Lett. 22 (1995) 2219.
[52] M. Javoy, et al., Earth Planet. Sci. Lett. 293 (2010) 259.
[53] E. Kaminski, M. Javoy, Earth Planet. Sci. Lett. 365 (2013) 97.
[54] M. Javoy, E. Kaminski, Earth Planet. Sci. Lett. 407 (2004) 1.
[55] H.S.C. O'Neill, H. Palme, Phil. Trans. R. Soc. Lond. A366 (2008) 4205.
[56] G. Caro, B. Bourdon, Geochim. Cosmochim. Acta 74 (2010) 3333.
[57] P.H. Warren, Earth Planet. Sci. Lett. 311 (2011) 93.
[58] M.G. Jackson, A.M. Jellinek, Earth Geochem. Geophys. Geosyst. 14 (2013) 2954.
[59] I.H. Campbell, H.S.C. O'Neill, Nature 483 (2012) 553.
[60] J. Zhang, N. Dauphas, A.M. Davis, I. Leya, A. Fedkin, Nat. Geosci. 5 (2012) 251.
[61] A.E. Ringwood, A. E, Composition and Petrology of the Earth'S Mantle, McGraw-Hill, New York, 1975.
[62] E. Jagoutz, H. Palme, H. Baddenhausen, K. Blum, M. Cendales, G. Dreibus, B. Spettel, H. Wanke, V. Lorenz, Proceedings of the Lunar and Planetary Science Conference, Pergamon, New York, 1979, p. 2031.
[63] H. Wanke, Philos. Trans. R. Soc. A303 (1981) 287.
[64] S.R. Hart, A. Zindler, Chem. Geol. 57 (1986) 247.
[65] C.J. Allegre, J.-P. Poirier, E. Humler, A.H. Hofmann, Earth Planet. Sci. Lett. 134 (1995) 515.
[66] H. Palme, H.S.C. O'Neill, Treatise on Geochemistry, second ed., Elsevier, Amsterdam, 2014, p. 1.
[67] T. Lyubetskaya, J. Korenaga, J. Geophys. Res. 112 (2007) B03211.
[68] S.A. Wipperfurth, M. Guo, O. Šrámek, W.F. McDonough, Earth Planet. Sci. Lett. 498 (2018) 196.
[69] G. Schubert, D. Stevenson, P. Cassen, J. Geophys. Res. 85 (1980) 2531.
[70] D.L. Turcotte, D. Paul, W.M. White, J. Geophys. Res. 106 (2001) 4265.
[71] D. Turcotte, G. Schubert, Geodynamics, Camridge University Press, 2002.
[72] G.F. Davies, Geochem. Geophys. Geosyst. 11 (2010) Q03.
[73] Y. Huang, V. Chubakov, F. Mantovani, W.F. McDonough, R.L. Rudnick, J. Phys. Conf. Ser. 375 (2012) 042041.
[74] D.L. Anderson, New Theory of the Earth, Cambridge University Press, 2007.
[75] B. Ricci, PoS NEUTEL 2015 (2015) 014.
[76] R. Han, Y.-F. Li, L. Zhan, W.F. McDonough. J. Cao, L. Ludhova, Chin. Phys. C 40 (2016) 033003.
[77] J.F. Beacom, et al., arXiv:1602.01733, 2016.
[78] O. Smirnov, Instrum. Exp. Tech. 46 (2003) 327.
[79] G. Bellini, et al., Phys. Lett. D 89 (2014) 112007.
[80] D.H. Wilkinson, Nucl. Phys. A377 (1982) 474.
[81] K.A. Olive, et al., (Particle Data Group), Chin. J. Phys C38 (2014) 090001.
[82] P. Vogel, Phys. Lett. D 29 (1984) 1918.
[83] S.A. Fayans, Sov. J. Nucl. Phys 42 (1985) (1985) 590.
[84] P. Vogel, J.F. Beacom, Phys. Lett. D 60 (1999) 053003.
[85] A. Kurylov, M.J. Ramsey-Musolf, P. Vogel, Phys. Rev. C 67 (2003) 035502.
[86] G. Zacek, et al., Phys. Lett. D 34 (1986) 2621.
[87] G.S. Vidyakin, et al., JETP Lett. 59 (1994) 390.
[88] Y. Declais, et al., Phys. Lett. 338 (1994) 383.
[89] A. Strumia, F. Vissani, Phys. Lett. B 564 (2003) 42.
[90] M. Morita, Suppl. Progr. Theor. Phys. 26 (1963) 1.
[91] H. Behrens, W. Bühring, Electron Radial Wave Functions and Nuclear Beta Decay, Clarendon, Oxford, 1982.
[92] H.F. Schopper, Weak Interactions and Nuclear Beta Decay, North-Holland, Amsterdam, 1966, p. 284.
[93] L. Hayen, N. Severijns, K. Bodek, D.R. Marian, X. Mougeot, Rev. Modern Phys. 90 (2018) 015008.
[94] N. Bahcall, Phys. Rev. 129 (1963) 2683.
[95] M.R. Harston, N.C. Pyper, Phys. Rev. A 45 (1992) 6282.
[96] X. Mougeot, M.-M. Bé, C. Bisch, M. Loidl, Phys. Rev. A 86 (2012) 042506-1.
[97] M. Loidl, C. Le-Bret, M. Rodrigues, X. Mougeot, J. Low Temp. Phys. 176 (2014) 1040, https://www.overleaf.com/project/5c939ebdd0dbb3140bd963ce.
[98] C. Bisch, X. Mougeot, M.-M. Bé, 16th International Congress of Metrology, 2013, p. 07004.
[99] G. Fiorentini, et al., Phys. Rev. C 81 (2010) 034602.
[100] G. Alimonti, et al., Borexino collaboration, NIMA 406 (1998) 411.
[101] G. Alimonti, et al., Borexino collaboration, Astropart. Phys. 8 (1998) 141.
[102] Y.A. Alkovali, Nucl. Data Sheets 76 (1995) 127.
[103] G.L. Fogli, E. Lisi, A. Palazzo, A.M. Rotunno, Earth Moon Planets 99 (2006) 111.
[104] N. Takeuchi, et al., Phys. Earth Planet. Inter. 288 (2019) 37.
[105] Y. Huang, V. Strati, F. Mantovani, S.B. Shirey, W.F. McDonough, Geochem. Geophys. Geosyst. 15 (2014) 3925.
[106] L.H. Ahrens, Geochim. Cosmochim. Acta 5 (1954) 49.
[107] S. Ando, Astrophys. J. 607 (2004) 20.
[108] T.K. Gaisser, M. Honda, Annu. Rev. Nucl. Part. Sci. 52 (2002) 53.
[109] Fengpeng An, et al., JUNO collaboration, J. Phys. G: Nucl. Part. Phys. 43 (2016) 030401.
[110] V. Kopeikin, L. Mikaelyan, V. Sinev, Phys. At. Nucl. 67 (2004) 1892.
[111] M. Fallot, S. Cormon, M. Estienne, A. Algora, V. Bui, et al., Phys. Rev. Lett. 109 (2012) 202504.
[112] T.A. Mueller, et al., Phys. Rev. C 83 (2011) 054615.

[113] F. Von Feilitzsch, A. Hahn, K. Schreckenbach, Phys. Lett. B 118 (1982) 162.
[114] K. Schreckenbach, G. Colvin, W. Gelletly, F. Von Feilitzsch, Phys. Lett. B 160 (1985) 325.
[115] A. Hahn, K. Schreckenbach, G. Colvin, B. Krusche, W. Gelletly, et al., Phys. Lett. B 218 (1989) 365.
[116] N. Haag, A. Gütlein, M. Hofmann, L. Oberauer, W. Potzel, K. Schreckenbach, F. Wagner, Phys. Rev. Lett. 112 (2014) 122501.
[117] P. Huber, Phys. Rev. C 84 (2011) 024617.
[118] A.C. Hayes, J.L. Friar, G.T. Garvey, G. Jungman, G. Jonkmans, Phys. Rev. Lett. 112 (2014) 202501.
[119] G. Mention, M. Fechner, Th. Lasserre, Th.A. Mueller, D. Lhuillier, M. Cribier, A. Letourneau, Phys. Rev. D 83 (2011) 073006.
[120] F.P. An, et al., (Daya Bay Collaboration), Phys. Rev. Lett. 118 (2017) 251801.
[121] F.P. An, et al., (Daya Bay Collaboration), Chin. Phys. C 41 (2017) 013002.
[122] Y. Abe, et al., (Double Chooz Collaboration), J. High Energy Phys. 10 (2014) 086.
[123] M.Y. Pac, et al., arXiv:1801.04049v1 (2018).
[124] K. Siyeon, et al., (NEOS collaboration) PoS ICRC2017 1024 2018.
[125] A.C. Hayes, P. Vogel, Annu. Rev. Nucl. Part. Sci. 66 (2016) 219.
[126] P. Huber, T. Schwetz, Phys. Rev. D 70 (2004) 053011.
[127] J. Mandula, Nuclear Power Engeneering Section, International Atomic Energy Agency, IAEA-PRIS database (Report No. IAEA-STI/PUB/1671) (2014).
[128] M. Baldoncini, et al., Phys. Rev. D 91 (2015) 065002.
[129] G. Bellini, A. Ianni, L. Ludhova, F. Mantovani, W.F. McDonough, Prog. Part. Nucl. Phys. 73 (2013) 1.
[130] Strati, et al., Prog. Earth Planet. Sci. 2 (5) (2015) 1.
[131] V.I. Kopeikin, L.A. Mikaelyan, V.V. Sinev, Phys. At. Nucl. 69 (2006) 185.
[132] X.B. Ma, et al., Nuclear Phys. A 966 (2017) 294.
[133] T. Hagner, et al., Astropart. Phys. 14 (2000) 33.
[134] M. Aglietta, et al., Nuovo Cimento Soc. Ital. Fis. C 12 (1989) 467.
[135] M. Aglietta, et al., Phys. At. Nucl. 66 (2003) 123.
[136] S. Abe, et al., KamLAND Collaboration, Phys. Rev. C 81 (2010) 025807.
[137] P. Antonioli, C. Ghetti, E.V. Korolkova, V.A. Kudryavtsev, G. Sartorelli, Astropart. Phys. 7 (1997) 357.
[138] A. Ferrari, P.R. Sala, A. Fassó, J. Ranft, FLUKA: A multi-particle transport code (program version 2005) CERN, Geneva, 2005.
[139] .
[140] S. Harissopulos, H.W. Becker, J.W. Hammer, A. Lagoyannis, C. Rolfs, F. Strieder, Phys. Rev. C 72 (2005) 062801.
[141] D. Franco, G. Consolati, D. Trezzi, Phys. Rev. C 83 (2011) 015504.
[142] G. Bellini, et al., Phys. Rev. Lett. 108 (2012) 051302.
[143] M. Agostini, et al., Phys. Rev. D 92 (2015) 031101.
[144] H. Watanabe, talk at Neutrino Research and Thermal Evolution of the Earth (2016) (https://www.tfc.tohoku.ac.jp/wp-content/uploads/2016/10/04_HirokoWatanabe_TFC2016.pdf).
[145] G. Alimonti, et al., Borexino Collaboration, Astropart. Phys. 16 (2002) 205.
[146] G. Alimonti, et al., Borexino Collaboration, Nucl. Instrum. Methods A 600 (2009) 568.
[147] C. Arpesella, et al., Borexino Collaboration, Phys. Rev. Lett. 101 (2008) 091302.
[148] J. Benziger, et al., Nucl. Instrum. Methods Phys. Res. A 582 (2007) 509.
[149] H. Back, et al., Borexino Collaboration, Nucl. Instrum. Methods Phys. Res. 584 (2008) 98.
[150] G. Bellini, et al., Borexino Collaboration, Phys. Rev. D 89 (2014) 112007.
[151] H. Back, et al., Borexino Collaboration, JINST 7 (2012) 10018.
[152] M. Agostini, et al., Borexino Collaboration, In LNGS annual report, www.lngs.infn.it/images/REIS/Annual_Report/AnnualReport_2017_low_def.pdf (2017).
[153] M. Agostini, et al., Borexino Collaboration, Nature 562 (2018) 505.
[154] J. Benziger, et al., Nucl. Instrum. Methods Phys. Res. A 587 (2008) 277.
[155] O. Yu. Smirnov, et al., Borexino Collaboration, Phys. Part. Nucl. 47 (2016) 995.
[156] G. Zuzel, H. Simgen, G. Heusser, Appl. Radiat. Isot. 61 (2004) 197.
[157] G. Bellini, et al., Borexino collaboration, J. Cosmol. Astropart. Phys. 08 (2013) 049.
[158] G. Bellini, et al., Borexino Collaboration, Phys. Lett. B 722 (2013) 295.
[159] M. Agostini, et al., Borexino Collaboration, Astropart. Phys. 97 (2018) 136.
[160] G. Bellini, et al., Borexino Collaboration, Phys. Rev. D 81 (2010) 034317.
[161] S. Kumaran, Towards the Updated geo-neutrino Measurement with Borexino (indico.in2p3.fr/event/18287/contributions/67510/attachments/52191/67338/poster_appec_v3.pdf) (2019).
[162] A. Gando, First Results of Neutrinoless Double Beta Decay Search with KamLAND-Zen (Ph.D. Thesis), 2012.
[163] A. Suzuki, Eur. Phys. J. C 74 (2014) 3094.
[164] B.E. Berger, et al., JINST 4 (2009) 04017.
[165] D.W. McKee, J.K. Busenitz, I. Ostrovskiy, Nucl. Instrum. Methods Phys. Res. A 587 (2008) 272.
[166] S. Abe, et al., KamLAND Collaboration, Phys. Rev. Lett. 100 (2008) 221803.
[167] K. Eguchi, et al., KamLAND Collaboration, Phys. Rev. Lett. 90 (2003) 021802.
[168] T. Araki, et al., KamLAND collaboration, Phys. Rev. Lett. 94 (2005) 081801.
[169] T. Araki, et al., KamLAND collaboration, Nature 436 (2005) 499.
[170] A. Gando, et al., KamLAND Collaboration, Phys. Rev. D 83 (2011) 052002.
[171] A. Gando, et al., Kamland Collaboration, Nat. Geosci. 4 (2011) 647.
[172] A. Gando, et al., KamLAND Collaboration, Phys. Rev. D 88 (2013) 033001.
[173] A. Gando, et al., Kamland Collaboration, Phys. Rev. C 92 (2015) 055808.
[174] G. Keefer, et al., Nucl. Instrum. Methods Phys. Res. A 769 (2015) 79.
[175] S. Enomoto, E. Ohtani, K. Inoue, A. Suzuki, Earth Planet. Sci. Lett. 258 (2007) 147.
[176] K. Inoue, Current status and future prospects of KamLAND-Zen www.rcnp.osaka-u.ac.jp/dbd18/Data/Prog/W0102_Inoue.pdf (2018).
[177] S.T. Dye, arXiv:1611.03559 [physics.geo-ph] (2016).
[178] G. Fiorentini, G.L. Fogli, E. Lisi, F. Mantovani, A.M. Rotunno, Phys. Rev. D 86 (2012) 033004.
[179] F. Mantovani, private communication.
[180] J.M. Herndon, Proc. Natl. Acad. Sci. USA 93 (1996) 646.
[181] D.F. Hollenbach, J.M. Herndon, Proc. Natl. Acad. Sci. USA 98 (2001) 11085.
[182] C. Degueldre, C. Fiorina, Solid Earth Sci. 1 (2016) 49.
[183] R.S. Raghavan, arXiv:hep-ex/0208038 (2002).

[184] V.D. Rusov, et al., J. Geophys. Res. 112 (2007) B09203.
[185] R.J. de Meijer, W. van Westrenen, S. Afr, J. Sci. 104 (2008) 111.
[186] J.M. Herndon, Curr. Sci. 104 (2014) 528.
[187] J.M. Herndon, D.A. Edgerley, arXiv:hep-ph/0501216 (2005).
[188] S.T. Dye, Phys. Lett. B 679 (2009) 15.
[189] B.D. Fields, K.A. Hochmuth, Earth Moon Planets 99 (2006) 155.
[190] S.T. Dye, private communication.
[191] K.K.M. Lee, R. Jeanloz, Geophys. Res. Lett. 30 (2003) 2212.
[192] V. Rama Murthy, W. van Westrenen, Y. Fei, Nature 423 (2003) 163.
[193] F. Nimmo, G.D. Price, J. Brodholt, D. Gubbins, Geophys. J. Int. 156 (2004) 363.
[194] S.T. Dye, E. Guillian, J.G. Learned, et al., Earth Moon Planets 99 (2006) 241.
[195] A. Suzuki, Earth Moon Planets 99 (2006) 359.
[196] M. Apollonio, et al., Phys. Rev. D 61 (2000) 012001.
[197] M. Batygov, Earth Moon Planets 99 (2006) 183.
[198] G.V. Domogatsky, V.I. Kopeikin, L.A. Mikaelyan, V.V. Sinev, Phys. At. Nucl. 69 (2006) 1894.
[199] H.K.M. Tanaka, H. Watanabe, Sci. Rep. 4 (2014) 4708.
[200] R. Safdi, B. Suerfu, Phys. Rev. Lett. 114 (2015) 071802.
[201] K. Abe, et al., Phys. Rev. D 83 (2011) 052010.
[202] H. Watanabe, et al., Astropart. Phys. 31 (2009) 320.
[203] X. Dai, et al., Nucl. Instrum. Methods Phys. Res. A 589 (2008) 290.
[204] M. Sweany, et al., Nucl. Instrum. Methods Phys. Res. A 664 (2012) 245.
[205] J.R. Alonso, et al., arXiv:1409.5864v3 (2014).
[206] M. Yeh, et al., Nucl. Instrum. Methods Phys. Res. A 660 (2011) 51.
[207] K. Zuber, Phys. Lett. B 571 (2003) 148.
[208] M. Chen, Potassium geo-neutrino detection (www.docstoc.com/docs/82267645/Potassium-Geo-neutrino-Detection) (2005).
[209] P. Belli, et al., Nucl. Instrum. Methods Phys. Res. A 615 (2010) 301.
[210] B. Szczerbinska, Proc. South Dakota Acad. Sci. 90 (2011) 13.
[211] Ch. Briançon, et al., Phys. At. Nucl. 78 (2015) 740.
[212] J. Ebert, et al., Nucl. Instrum. Methods Phys. Res. A 807 (2016) 114.
[213] C. Aberle, A. Elagin, H.J. Frisch, M. Wetstein, L. Winslow, JINST 9 (2014) P06012.
[214] M. Leyton, S. Dye, J. Monroe, Nature Commun. 8 (2017) 15989.
[215] Z. Daraktchieva, et al., J. Phys G 35 (2008) 125107.
[216] D. Dujmic, et al., Astropart. Phys. 30 (2008) 58.
[217] https://today.lbl.gov/new-beginnings-for-the-sno-neutrino-detector/.
[218] M.C. Chen, Earth Moon Planets 99 (2006) 221.
[219] H.K.C. Perry, J.-C. Mareschal, C. Jaupart, Earth Planet. Sci. Lett. 288 (2009) 301.
[220] V. Strati, et al., Geochem. Geophys. Geosyst. 18 (2017) 4326.
[221] S. Andringa, et al., Adv. High Energy Phys. 2016 (2016) 6194250.
[222] M. Baldoncini, et al., J. Phys. Conf. Ser. 718 (2016) 062003.
[223] H. Lu, et al., J. Phys. Conf. Ser. 888 (2017) 012088.
[224] H. Yang, et al., JINST 12 (2017) T11004.
[225] Y.-F. Li, et al., Phys. Rev. D 88 (2013) 013008.
[226] D.V. Forero, R. Hawkins, P. Huber, arXiv:1710.07378 (2017).
[227] D.L. Danielson, A.C. Hayes, G.T. Garvey, Phys. Rev. D 99 (2019) 036001.
[228] M. Reguzzoni, L. Rossi, M. Baldoncini, I. Callegari, P. Poli, D. Sampietro, V. Strati, et al., J. Geophys. Res. Solid Earth (2019) http://dx.doi.org/
      10.1029/2018jb016681.
[229] M.R. Drinkwater, R. Floberghagen, R. Haagmans, D. Muzi, A. Popescu, GOCE: ESA's First Earth Explorer Core Mission, in: Earth Gravity Field
      from Space - from Sensors to Earth Sciences, Kluwer Academic Publishers, Dordrecht, Netherlands, ISBN: 1-4020-1408-2, 2003.
[230] J. Li, X. Ji, W. Haxton, J.S.Y. Wang, Physics Procedia 61 (2015) 576.
[231] Z. Guo, M. Yeh, R. Zhang, D.W. Cao, M. Qi, Z. Wang, S. Chen, Astropart. Phys. 109 (2019) 33.
[232] Z. Wang, et al., Nucl. Instrum. Methods Phys. Res. A 35 (2012) 685.
[233] M. Wurm, et al., LENA Collaboration, Astropart. Phys. 35 (2012) 685.
[234] I.R. Barabanov, et al., Phys. At. Nucl. 80 (2017) 446.
[235] https://www.phys.hawaii.edu/sdye/CEROS-report.pdf.
[236] J.G. Learned, S.T. Dye, S. Pakvasa, arXiv:0810.4975 (2008).